

ESCUELA TÉCNICA SUPERIOR DE INGENIEROS INDUSTRIALES
UNIVERSIDAD POLITÉCNICA DE MADRID

José Gutiérrez Abascal, 2. 28006 Madrid
Tel: 91 336 3060
info.industriales@upm.es

www.industriales.upm.es



POLITÉCNICA

INDUSTRIALES

05 TRABAJO FIN DE GRADO

Josep María Barberá Civera



TRABAJO FIN DE GRADO

COMPUTATIONAL STUDY OF OSCILLATORY GROWTH INSTABILITY IN DIRECTIONAL SOLIDIFICATION OF ALLOYS



SEPTIEMBRE 2023

Josep María Barberá Civera

DIRECTORES DEL TRABAJO FIN DE GRADO:

**Damien Tourret
Milagrosa González
Juan José Moreno**



ESCUELA TÉCNICA SUPERIOR DE INGENIEROS INDUSTRIALES

GRADO EN INGENIERÍA EN TECNOLOGÍAS INDUSTRIALES

Bachelor's Thesis

**Computational study of Oscillatory Growth Instability in
Directional Solidification of Alloys**

Supervisors:

Dr. Damien Tourret

Dr. Milagrosa González

Dr. Juan José Moreno

Student:

Josep María Barberá Civera

17048

September 2023

*“If we want a world of peace and justice,
we must resolutely place intelligence at the service of Love.”*

- Antoine de Saint-Exupéry

ACKNOWLEDGEMENTS

First and foremost, I want to express my sincere gratitude to my advisor, Damien Tourret. I'm really thankful for your invaluable guidance and support, and the unbelievable opportunity to be a part of IMDEA. Your accessibility whenever I needed assistance was incredible exceptional. My deep thanks also go to my other two advisors, Milagrosa Gonzalez and Juan José Moreno. Milagrosa, I appreciate your encouragement to apply for IMDEA's Research Initiation Fellowship (RIF) and for your constant support throughout the process. To both of you, I'm grateful for accepting me for the Bachelor Thesis and for your patience and understanding when plans changed or delays occurred.

Moreover, I'd like to extend my deep appreciation to Thomas Isensee for his invaluable support and guidance throughout this research journey. Thank you for patiently addressing my questions and doubts and for the enlightening command-line sessions. Alongside Thomas, I'd like to thank the rest of Damien's group at IMDEA: Jose, Jorge, Adrian, Mohamed, and Rouhollah, for your unwavering assistance. I'd also like to acknowledge IMDEA Materials Institute for the RIF fellowship and the enriching research environment it provided.

Furthermore, I'm deeply thankful to my friends in Madrid: Javis, Luises, Miguel, Jaramillo, Huertas, Miquel, Ramón, Josep, and Ferran, among others (my apologies to those I've missed). Special thanks to the young group from Galapagar. I'm also grateful to Javier, Gonzalo, Marina, Guillermos, Manu, Estrella, and Tomás, with whom I navigated the challenges of coursework and projects at ETSII.

Lastly, I want to express my deepest appreciation to my parents, Josep and Fina, and my lovely siblings, Águeda, Rafa, Noemí, and Arnau, for the countless sacrifices you've made on my behalf over the years.

My most sincere thanks to all those who cannot be mentioned here but who have supported me unconditionally.



"Plantilla en LaTeX acorde con la Normativa para la elaboración de informes de TFT de la ETSII (UPM)" by Javier Soto Pérez-Olivares is licensed under a [Creative Commons Attribution 4.0 International License](#).

RESUMEN EJECUTIVO

La solidificación direccional (SD) es esencial en la producción de componentes de alta gama. Los álabes de turbinas monocristalinos de superaleaciones con base de Níquel utilizadas en aplicaciones aeroespaciales [86] son un claro ejemplo. Estos presentan tecnología muy avanzada y pueden soportar condiciones extremas. Sin embargo, la SD puede dar lugar a defectos como canales segregados y pecas [25, 93, 52, 85], lo que provoca el rechazo de muchas piezas. Por ello, comprender las condiciones de SD estables es crucial para los componentes de nueva generación.

Recientes experimentos desarrollados con radiografía de rayos X han descubierto inestabilidades oscilatorias durante la SD de la superaleación CMSX-4 basada en Ni [90] (véase FIG. 0.1). A lo largo de los años se han estudiado diferentes inestabilidades oscilatorias en la SD, si bien las oscilaciones del CMSX-4, causadas por la flotabilidad inducida por gravedad, plantean un reto único. El impacto de la convección por flotabilidad en el crecimiento dendrítico y las heterogeneidades microestructurales se conocen desde hace décadas, aunque su modelización cuantitativa sigue siendo computacionalmente costosa [92, 91].

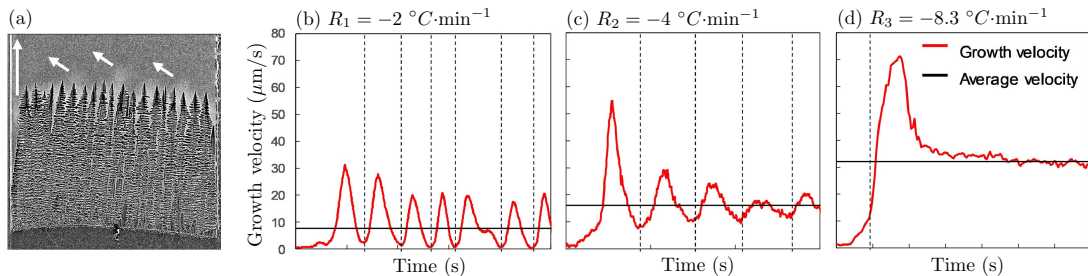


Figure 0.1: Crecimiento oscilatorio descubierto mediante radiografía de rayos X durante la solidificación direccional de la superaleación CMSX-4 [90]. (a) Evolución temporal de la velocidad de crecimiento de las dendritas. Las líneas horizontales negras en los gráficos corresponden a las velocidades medias de (b) $7,6 \mu\text{m/s}$, (c) $15 \mu\text{m/s}$ y (d) $31 \mu\text{m/s}$ para las velocidades de enfriamiento de (b) $-2 \text{ }^{\circ}\text{C/min}$, (c) $-4 \text{ }^{\circ}\text{C/min}$ y (d) $-8,3 \text{ }^{\circ}\text{C/min}$. Las flechas blancas en (a) indican la dirección del flujo convectivo de soluto durante la solidificación de la red dendrítica.

Utilizando un modelo multiescala de red de agujas dendríticas (DNN) [105, 107], extendido para incorporar el flujo de fluidos en fase líquida [104, 56] (ver Fig. 0.2), Isensee y Tourret replicaron las oscilaciones de crecimiento de CMSX-4 [56]. Sus simulaciones confirmaron la transición del comportamiento oscilatorio al amortiguado según tasas de enfriamiento crecientes (equivalentes a velocidades de arrastre equivalente V_p). Así mismo, destacaron la importancia del espaciado dendrítico primario Λ , que fomenta las oscilaciones a Λ altos y las inhibe a Λ bajos. También observaron que se producían oscilaciones continuadas cuando la velocidad media del fluido \bar{V} coincidía estrechamente con V_p .

Las simulaciones computacionales del comportamiento oscilatorio abren las puertas a una exploración exhaustiva de las condiciones y características, especialmente en lo que respecta a los parámetros de aleación y las condiciones de procesamiento. Basándonos en el trabajo previo de Isensee y Tourret [56], hemos llevado a cabo un amplio estudio de las oscilaciones inducidas por flotabilidad, variando el espaciado primario y la velocidad de tracción. Nuestro objetivo era determinar si este fenómeno se aplica a otras aleaciones mediante la combinación del gradiente de temperatura G , la velocidad de tracción V_p y el espaciado primario Λ . En nuestra investigación, hemos centrado nuestra atención en la aleación Al-4at.%Cu, que está bien documentada y sin informes previos de tales oscilaciones.

Presentamos aquí cuatro mapas (véase FIG. 0.3) que resumen nuestra exploración acerca del

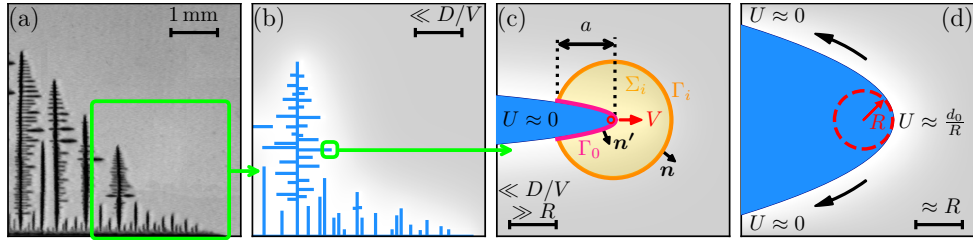


Figure 0.2: Modelo de red de agujas dendríticas (DNN) ilustrado conceptualmente. El modelo se basa en una estructura de red dendrítica que toma como ejemplo un cristal de bromuro de amonio en una solución acuosa sobresaturada, como se muestra en (a) [26]. En el modelo DNN, la estructura se representa mediante una red de finas agujas parabólicas que interactúan a través de un campo de difusión de largo alcance, como se representa en (b). La concentración de equilibrio del líquido se impone en las agujas. Las velocidades instantáneas de las puntas $V(t)$ y los radios $R(t)$ de cada aguja se obtienen mediante una combinación de condiciones en dos escalas de longitud diferentes. En la escala intermedia, una condición de conservación del soluto cerca de la punta fija el producto $RV \propto \mathcal{F}$ (3D) o $RV^2 \propto \mathcal{F}^2$ (2D), como puede verse en (c). En la escala pequeña -radio de la punta $R-$, la condición de solvencia microscópica fija el producto R^2V , como se respresenta (d). Obtenido de [57].

comportamiento oscilatorio en esta aleación binaria. Comenzando con los valores naturales de la aleación (mapa A), ajustamos el coeficiente de difusión (D) y el coeficiente de partición (k) para observar sus efectos sobre los patrones oscilatorios. Las simulaciones posteriores (etiquetadas como B y C) mantienen la difusividad original mientras varían el coeficiente de partición aumentando su valor de 0,14 a 0,2 o disminuyéndolo a 0,1. Por su parte, la simulación D modifica la difusividad (D) de $3 \times 10^{-9} \text{ m}^2/\text{s}$ a $1,5 \times 10^{-9} \text{ m}^2/\text{s}$, manteniendo constante el coeficiente de partición.

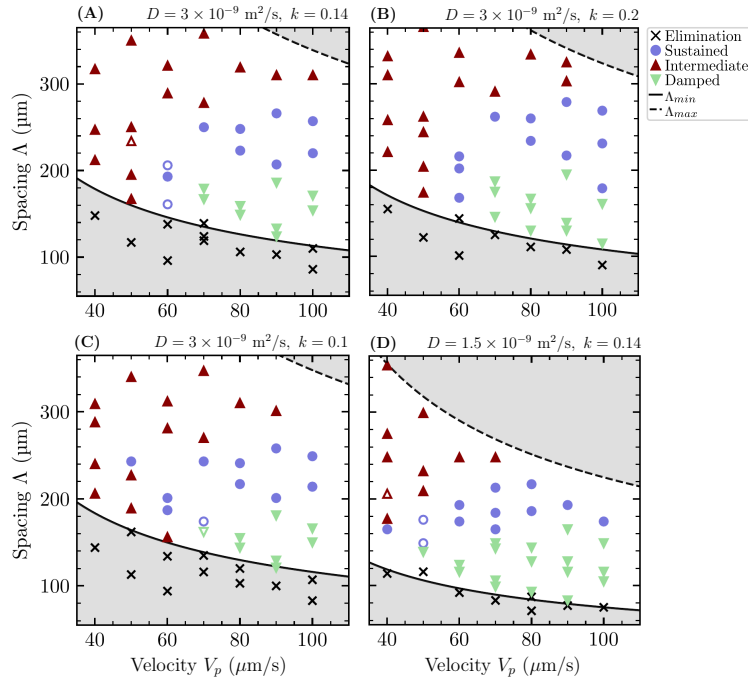


Figure 0.3: Mapas de caracterización oscilatorio para la aleación Al-4at.%Cu. Exploran variaciones del coeficiente de difusión (D) y del coeficiente de partición (k). Los símbolos abiertos representan comportamientos no clasificados.

Los resultados de este estudio han demostrado que el régimen oscilatorio observado en la aleación CMSX-4 es general a otras aleaciones binarias. A continuación, nos centraremos más específicamente en el mapa (A) llevando a cabo una caracterización exhaustiva de los compor-

tamientos oscilatorios en el mismo. Este mapa consta de 44 simulaciones en las que cada una de ellas utiliza una única GPU, principalmente la Nvidia RTX 3090, y suelen tardar un máximo de 92 horas en finalizar.

Las simulaciones son similares a las descritas en la Ref. [56] (Secciones 3.1 y 4). Implican un dominio con dimensiones H (en la dirección x) y W (en la dirección y), donde crecen N agujas primarias espaciadas uniformemente en la base según la dirección $x+$. Además, están alineadas inicialmente en x a lo largo de la localización de la temperatura del *liquidus*. Se aplican condiciones de contorno laterales periódicas en la dirección y , mientras que se utilizan condiciones de ausencia de flujo y de deslizamiento libre a lo largo de los contornos superior e inferior en la dirección x .

Para acomodar el crecimiento, se emplea un marco móvil en la dirección x , asegurando que la punta de la dendrita más avanzada en la dirección x permanece fija dentro del 30% al 65% de la altura del dominio desde el límite inferior.

El tamaño del dominio en x (altura H) se elige para minimizar el efecto de las condiciones de contorno en el patrón de flujo. Esto se determina mediante ensayo y error, manteniendo la longitud del líquido superior a $5D/V_p$ y la longitud del sólido superior a $8D/V_p$. En la dirección y , el tamaño del dominio se fija en 630 o 1470 puntos de rejilla interior para mayor comodidad y eficiencia computacional. Cada simulación comienza con un rango de entre 7 y 30 dendritas primarias para explorar diferentes valores de espaciado primario (Λ) y se ejecuta durante duraciones de 90 a 120 segundos para capturar períodos de oscilación para el análisis, según sea necesario. La figura 0.4 ilustra un ejemplo de visualización de la simulación gracias al uso del software *Paraview*.

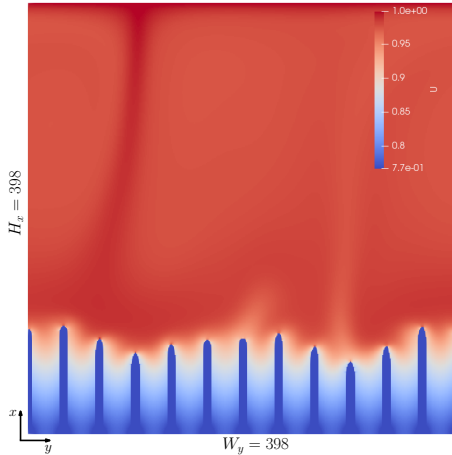


Figure 0.4: Captura de pantalla de *ParaView*, en la que se visualizan los resultados de la simulación. Observamos la representación del campo de concentración (U) para la aleación binaria seleccionada ($Al-4at.\%Cu$) en una simulación con doce agujas ($N = 12$) y los siguientes valores físicos: $k = 0,14$, $V_p = 40 \mu\text{m/s}$, $H_x = 398$ y $W_y = 398$ puntos de cuadrícula. La versatilidad de *ParaView* permite un análisis exhaustivo de procesos físicos complejos, ofreciendo valiosas perspectivas en nuestras simulaciones.

Para analizar los comportamientos de crecimiento simulados y extraer las características de oscilación, ajustamos las velocidades individuales de las dendritas, $V(t)$, a dos funciones:

$$v_1(t) = V_0 - A \cos [2\pi(t - t_0)f] \exp(-t/\tau), \quad (0.1)$$

$$v_2(t) = V_0 - A \{(1 - S) \cos [2\pi(t - t_0)f] + 2S|\cos [\pi(t - t_0)f]| - S\}, \quad (0.2)$$

Estos ajustes emplean cinco parámetros: velocidad de rango medio V_0 , origen temporal t_0 , amplitud de oscilación A , frecuencia de oscilación f , y tiempo de amortiguación τ (Ec.(0.1)) o

un factor S que mide la “puntiagudez” (Ec.(0.2)). El factor S oscila entre 0 y 1, lo que permite picos dentro de las oscilaciones de frecuencia estable (véase FIG. 0.5).

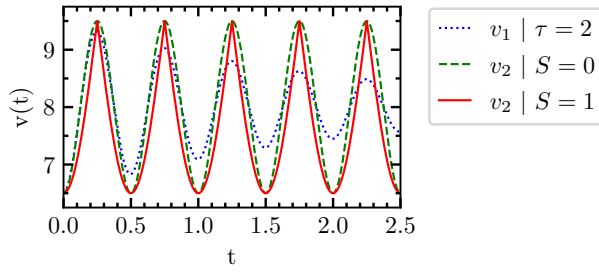


Figure 0.5: Ilustración de las funciones $v_1(t)$ y $v_2(t)$ para $V_0 = 8,0$, $A = 1,5$, $f = 2,0$, $t_0 = 0,0$ y distintos valores de τ (Ec. (0.1)) o S (Ec. (0.2)).

El proceso de ajuste dinámico selecciona el mejor de dichos ajustes entre estas funciones basándose en el coeficiente de determinación r^2 . Las velocidades de crecimiento $V(t)$ con ajustes pobres ($r^2 < 0,8$) se han etiquetado como *ruidosas*. Para $r^2 \geq 0,8$, los comportamientos se han clasificado como *amortiguados* si Ec. (0.1) se ajusta mejor que Ec. (0.2); de lo contrario, se consideran *sostenidos o continuados*. Las oscilaciones amortiguadas son fácilmente distinguibles mediante inspección visual de $V(t)$. Un ejemplo de oscilaciones amortiguadas junto con el espectro de Fourier para $V(t)$ se puede ver en la figura 0.6.

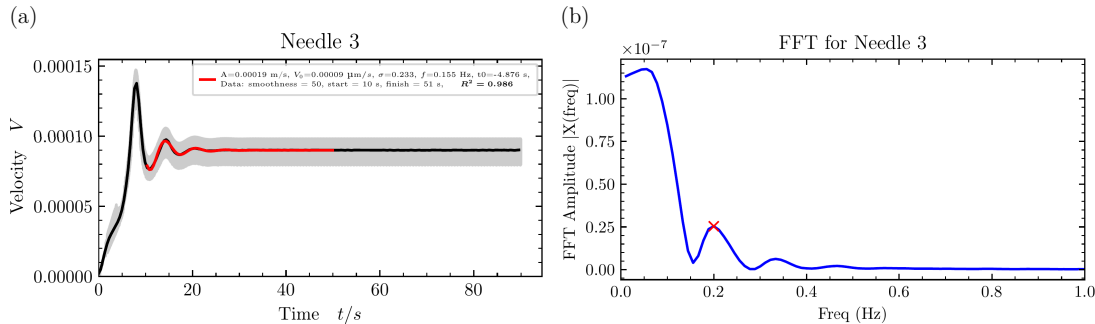


Figure 0.6: Comportamiento oscilatorio amortiguado para la dendrita número 3 en la simulación V9_N10_D3_k0.14_AlCu_630x398 (notación condensada). (a) Velocidad de crecimiento de la dendrita en función del tiempo junto con el ajuste (línea roja), y (b) espectro de Fourier para estimar la frecuencia inicial (f) antes del ajuste.

La figura 0.7 muestra el mapa de comportamiento de crecimiento (A) en relación a la velocidad de tracción V_p y el espaciado dendritico primario Λ . El crecimiento oscilatorio continuado se aprecia durante un rango de valores para (V_p, Λ) , pero las oscilaciones sólo se observan para $V_p \geq 60 \mu\text{m/s}$. La mayoría de las oscilaciones sostenidas (símbolos \bullet) se producen dentro de un intervalo de espaciado primario de $190 \leq \Lambda/\mu\text{m} \leq 270$, mientras que las oscilaciones amortiguadas (símbolos ∇) se encuentran dentro de $120 \leq \Lambda/\mu\text{m} \leq 190$.

Los colores de los símbolos representan la relación entre la velocidad media del fluido \bar{V} y la velocidad de arrastre V_p : verde claro ($\bar{V}/V_p \leq 0,05$), azul medio ($0,05 \leq \bar{V}/V_p \leq 2,5$) o rojo oscuro ($\bar{V}/V_p \geq 2,5$). Este esquema de colores se correlaciona bien con la aparición de oscilaciones amortiguadas, sostenidas o ruidosas, excepto para unos pocos puntos cerca de la transición entre oscilaciones sostenidas y ruidosas. En la figura 0.16 vemos un ejemplo de comportamiento de oscilación amortiguada correspondiente a la etiqueta gris 3.a y 3.b de la figura 0.7.

Estos hallazgos sugieren que este fenómeno podría ser una característica general de las aleaciones binarias, dadas las condiciones adecuadas de gradiente de temperatura (G), velocidad de

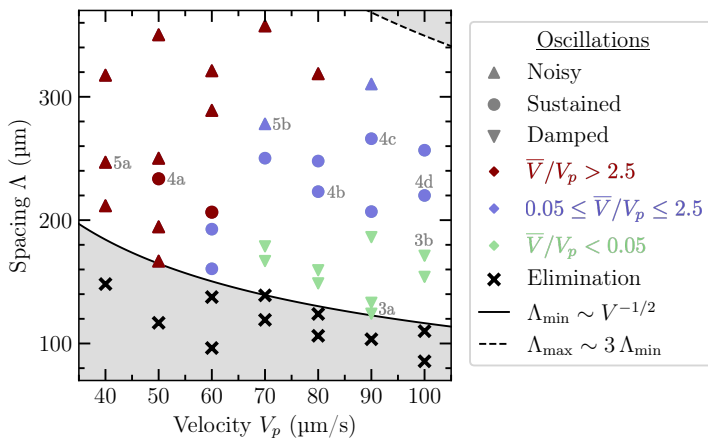


Figura 0.7: Mapa de comportamiento oscilatorio. Los tipos de símbolos denotan diferentes comportamientos de crecimiento: (\times) eliminación de alguna dendrita para $\Lambda < \Lambda_{\min}$ (línea negra) o (\blacktriangledown) oscilaciones amortiguadas, (\bullet) sostenidas o (\blacktriangle) ruidosas. Los símbolos están coloreados según la relación \bar{V}/V_p . Las etiquetas de texto gris junto a los símbolos marcan los casos más relevantes.

arrastre (V_p) y espaciado primario (Λ). Confirmamos que la relación entre la velocidad media del fluido (\bar{V}) y la velocidad de arrastre (V_p) sirve como indicador razonable del régimen oscilatorio (es decir, amortiguado, sostenido o ruidoso). Sin embargo, los valores umbral de \bar{V}/V_p difieren de los observados en el estudio anterior de Isensee y Tourret sobre CMSX-4 ($\xi_1 \approx 1,0$, $\xi_2 \approx 2,0$), lo que sugiere una posible dependencia de los parámetros de la aleación y de las condiciones de procesamiento.

En este estudio, la transición de oscilaciones amortiguadas a oscilaciones sostenidas ha coincidido con la aparición de vórtices de convección en el fluido, lo que contrasta con los resultados anteriores para CMSX-4, donde los vórtices de convección bien establecidos estaban presentes en ambos regímenes. Nuestros resultados no han captado la transición esperada de oscilaciones sostenidas a amortiguadas con el aumento de V_p (velocidad de enfriamiento), posiblemente porque se produce a valores de V_p más altos que los explorados en este estudio.

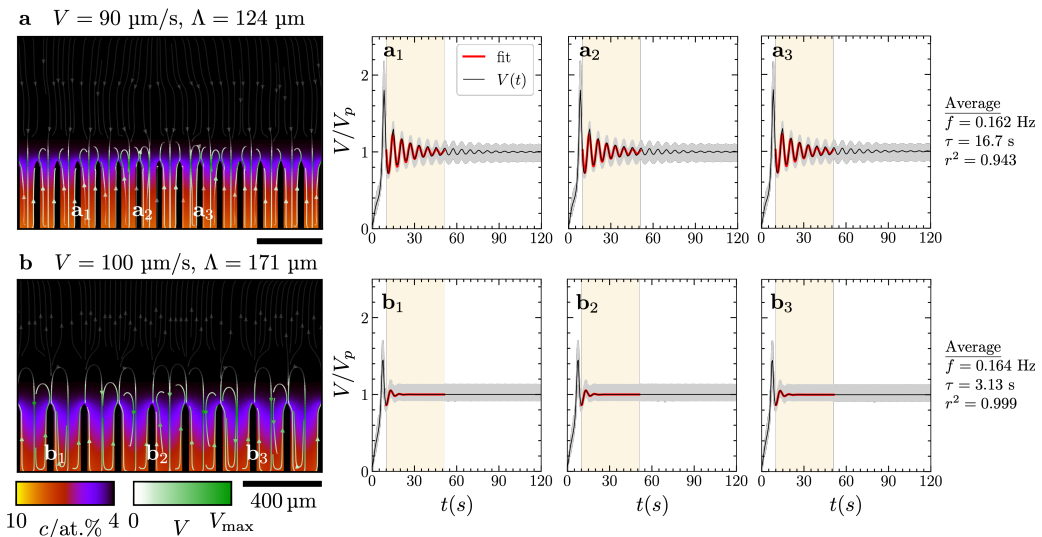


Figura 0.8: Oscilaciones amortiguadas (a) para $V = 90 \mu\text{m/s}$ y $\Lambda = 124 \mu\text{m}$ y (b) para $V = 100 \mu\text{m/s}$ y $\Lambda = 171 \mu\text{m}$. (Izquierda) Campo de concentración (mapa de colores) y flujo de fluido (líneas de corriente) a $t = 120$ s. (derecha) Velocidades de punta de las dendritas seleccionadas, mostrando $V(t)$ sin filtrar (gris) y suavizada (negro), así como la función ajustada (rojo grueso) y el rango (fondo sombreado).

Códigos UNESCO

- [120326] - Simulaciones
- [221101] - Aleaciones
- [221106] - Dendritas
- [120903] - Análisis de Datos

Palabras clave:

Ciencia de materiales computacional, red dendrítica de agujas, GPUs, solidificación direccional.

Repositorio de GitHub:

Se ha creado un repositorio en GitHub que contiene los scripts en Python utilizados para el posprocesado de datos y la automatización del lanzamiento de las simulaciones.

Enlace: <https://github.com/jbarciv/DNN-FittyPlot>

Los principales resultados de la Sec. 5.2 y 5.3 de esta tesis han sido publicados en

J. M. Barberá, T. Isensee, y D. Tourret. “On the occurrence of buoyancy-induced oscillatory growth instability in directional solidification of alloys”. En: *IOP Conference Series: Ciencia e Ingeniería de Materiales* 1281.1 (Mayo 2023), p. 012050. doi: [10.1088/1757-899X/1281/1/012050](https://doi.org/10.1088/1757-899X/1281/1/012050). url: <https://dx.doi.org/10.1088/1757-899X/1281/1/012050>.

Este estudio ha contado con el apoyo del Ministerio de Ciencia e Innovación a través del sello de excelencia María de Maeztu del Instituto IMDEA Materiales (CEX2018-000800-M).

EXECUTIVE OVERVIEW

Directional solidification (DS) is essential in the production of high-value components, exemplified by single-crystal Ni-based superalloy turbine blades used in aerospace applications [86]. These blades are highly advanced and can withstand extreme conditions. However, DS can lead to defects like segregated channels and freckles [25, 93, 52, 85], resulting in the rejection of many parts. Thus, understanding stable DS conditions is crucial for next-generation components.

Recent X-ray *in-situ* radiography experiments revealed oscillatory instabilities during DS of Ni-based superalloy CMSX-4 [90] (see FIG. 0.9). Different oscillatory instabilities in DS have been studied over the years, but CMSX-4's oscillations, caused by gravity-induced buoyancy, pose unique challenges. Buoyant convection's impact on dendritic growth and microstructure heterogeneities has been acknowledged for decades, but its quantitatively modeling remains computationally intensive [92, 91].

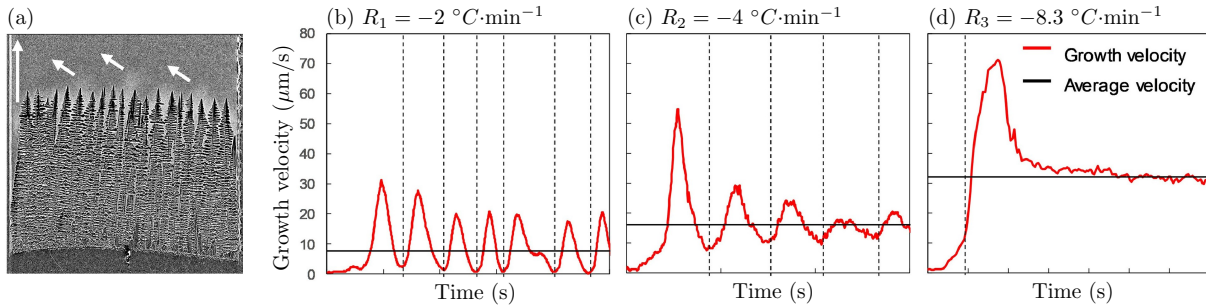


Figure 0.9: Oscillatory growth behavior discovered using *in-situ* X-ray radiography during the directional solidification of a CMSX-4 superalloy [90]. Time evolution of the growth velocity for dendrites shown in (a). The black horizontal lines in the growth velocity plots correspond to the average velocities and are (b) $7.6 \mu\text{m}/\text{s}$, (c) $15 \mu\text{m}/\text{s}$ and (d) $31 \mu\text{m}/\text{s}$ for the cooling rates of (b) $-2 \text{ }^{\circ}\text{C}/\text{min}$, (c) $-4 \text{ }^{\circ}\text{C}/\text{min}$ and (d) $-8.3 \text{ }^{\circ}\text{C}/\text{min}$. White arrows in (a) indicate the direction for solutal convective flow during solidification of the network.

Using a multiscale dendritic needle network (DNN) approach [105, 107] extended for fluid flow in the liquid phase [104, 56] (see Fig. 0.10), Isensee and Tourret replicated CMSX-4's growth oscillations [56]. Their simulations confirmed the transition from oscillatory to damped oscillations with increasing cooling rates (or equivalent pulling velocity V_p). They highlighted the importance of primary dendritic spacing Λ , promoting oscillations at high Λ and inhibiting them at low Λ . They also noted that sustained oscillations occurred when average fluid velocity \bar{V} closely matched V_p .

Computational simulations of oscillatory behavior open doors to a thorough exploration of conditions and characteristics, especially concerning alloy parameters and processing conditions. Building upon the prior work of Isensee and Tourret [56], we conduct an extensive study of buoyancy-induced oscillations, varying primary spacing and pulling velocity. Our aim is to determine if this phenomenon applies to other alloys through the combination of temperature gradient G , pulling velocity V_p , and primary spacing Λ . To investigate, we turn our attention to Al-4at.%Cu, a well-documented alloy with no prior reports of such oscillations.

Here we present four maps (see FIG. 0.11) summarizing our exploration of oscillatory behavior in this binary alloy. Beginning with the natural values of the alloy (labeled as A), we adjust the diffusion coefficient (D) and partition coefficient (k) to observe their effects on oscillatory patterns. Subsequent simulations (labeled B and C) maintain the original diffusivity while varying the partition coefficient, i.e., increasing its value from 0.14 to 0.2 or decreasing it to

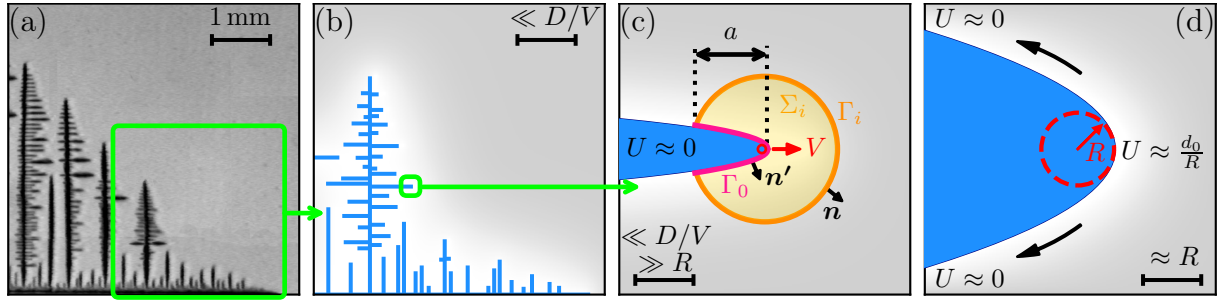


Figure 0.10: The Dendritic Needle Network (DNN) model conceptually illustrated. The model is based on a dendritic network structure of an ammonium-bromide crystal in a supersaturated aqueous solution, as shown in (a) [26]. In the DNN model, the structure is represented by a network of thin parabolic needles that interact through a long-range diffusion field, as depicted in (b). The liquid equilibrium concentration is imposed on the needles. The instantaneous tip velocities $V(t)$ and radii $R(t)$ of each needle are obtained by a combination of conditions on two different length scales. At the intermediate scale, a solute conservation condition near the tip fixes the product $RV \propto \mathcal{F}$ (3D) or $RV^2 \propto \mathcal{F}^2$ (2D), where the flux intensity factor (FIF) \mathcal{F} is computed by integrating the flux towards the dendrite tip over the contour Γ_0 as shown in (c). At the small scale of the tip radius R , the microscopic solvability condition fixes the product R^2V in (d). Sourced from [57].

0.1. And simulation D modifies the diffusivity while keeping the partition coefficient constant, specifically reducing D from $3 \times 10^{-9} \text{ m}^2/\text{s}$ to $1.5 \times 10^{-9} \text{ m}^2/\text{s}$.

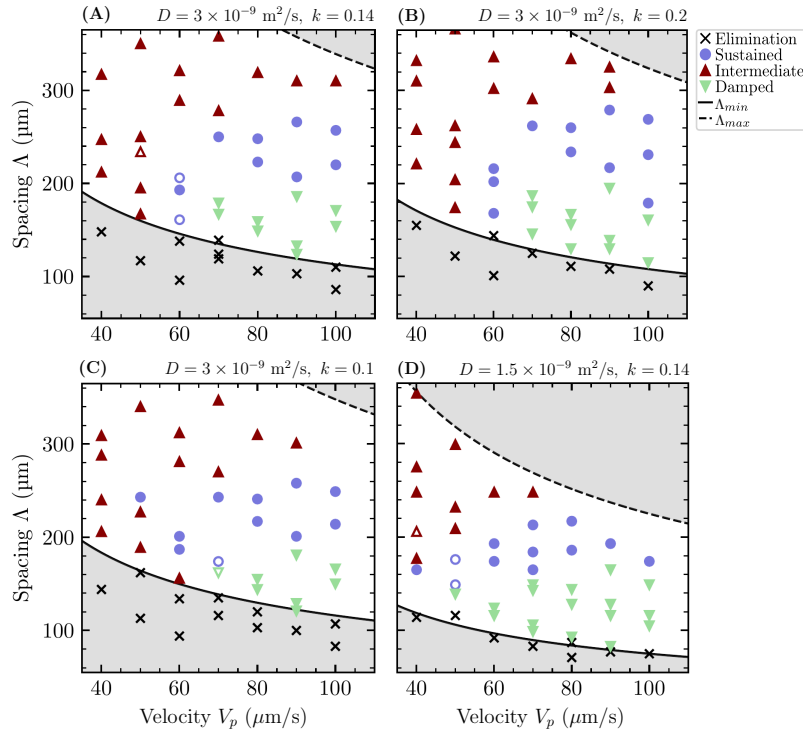


Figure 0.11: Oscillation characterization maps for the Al-4at.%Cu alloy, exploring variations in parameters, including diffusion coefficient (D) and partition coefficient (k). Open symbols represent unclassified behaviors.

Results of this study have shown that the oscillatory regime observed in CMSX-4 alloy is general to other binary alloy. We then focused more specifically on map (A) and performed a deep comprehensive characterization of the oscillatory behaviors therein. This map consist of 44 simulations where each of them utilizes a single GPU, primarily the Nvidia RTX 3090, and typically takes a maximum of 92 hours to finish in terms of wall time.

The simulations are similar to those described in Ref. [56] (Sections 3.1 and 4). They involve a domain with dimensions H (in the x -direction) and W (in the y -direction), where N primary needles grow evenly spaced at the bottom in the $x+$ direction, initially aligned in x along the liquidus temperature location. Periodic lateral boundary conditions are applied in the y direction, while no-flux and free-slip conditions are used along the top and bottom boundaries in the x direction.

To accommodate growth, a moving frame in the x -direction is employed, ensuring the most advanced needle tip in the x direction remains fixed within 30% to 65% of the domain height from the bottom boundary.

The domain size in x (height H) is chosen to minimize the effect of boundary conditions on the flow pattern. This is determined through trial-and-error, maintaining the liquid length greater than $5D/V_p$ and the solid length greater than $8D/V_p$. In the y direction, the domain size is set to either 630 or 1470 inner grid points for computational convenience and efficiency. Each simulation starts with between 7 and 30 primary dendrites to explore different primary spacing values (Λ) and runs for durations of 90 to 120 seconds to capture oscillation periods for analysis, as needed. Figure 0.12 illustrates typical results visualized with the software *Paraview*.

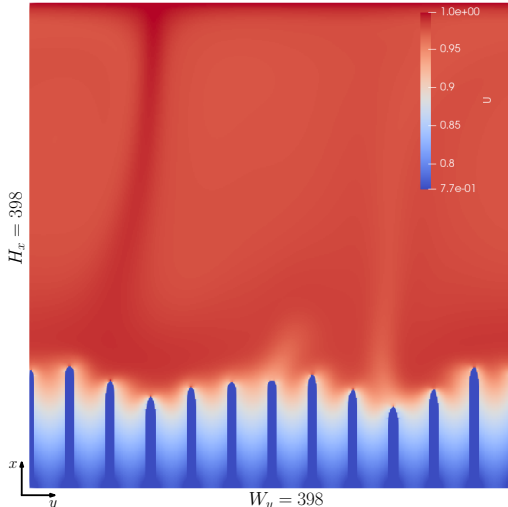


Figure 0.12: Screenshot from *ParaView*, visualizing simulation results. Here, we observe the representation of the concentration field (U) for the selected binary alloy (Al-4at.%Cu) in a simulation with twelve needles ($N = 12$) and the next physical values: $k = 0.14$, $V_p = 40 \mu\text{m/s}$, $H_x = 398$ and $W_y = 398$ grid points. *ParaView*'s versatility enables a comprehensive analysis of complex physical processes, offering valuable insights into our simulations.

To analyze simulated growth behaviors and extract oscillation characteristics, we fitted individual needle velocities, $V(t)$, to two functions:

$$v_1(t) = V_0 - A \cos [2\pi(t - t_0)f] \exp(-t/\tau), \quad (0.3)$$

$$v_2(t) = V_0 - A \{(1 - S) \cos [2\pi(t - t_0)f] + 2S| \cos [\pi(t - t_0)f] | - S\}, \quad (0.4)$$

These fittings used five parameters: mid-range velocity V_0 , time origin t_0 , oscillation amplitude A , oscillation frequency f , and either a damping time τ (Eq.(0.3)) or a “spikiness” factor S (Eq.(0.4)). S ranged from 0 to 1, allowing for spiky bursts within stable-frequency oscillations (see FIG. 0.13).

The fitting process selected the best fit between these functions based on coefficient of determination r^2 . Growth velocities $V(t)$ with poor fits ($r^2 < 0.8$) were labeled as *noisy*. For

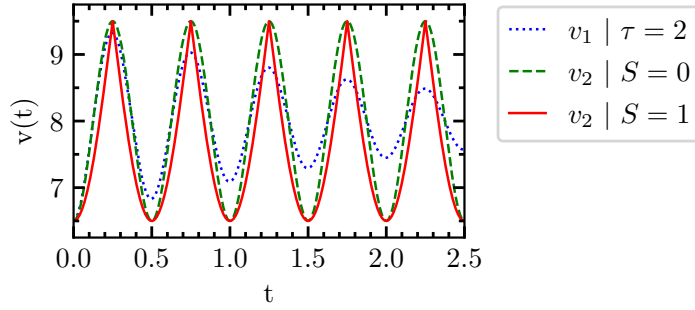


Figure 0.13: Illustration of functions $v_1(t)$ and $v_2(t)$ for $V_0 = 8.0$, $A = 1.5$, $f = 2.0$, $t_0 = 0.0$ and different values of τ (Eq. (0.3)) or S (Eq. (0.4)).

$r^2 \geq 0.8$, behaviors were categorized as *damped* if Eq. (0.3) fit better than Eq. (0.4); otherwise, they were considered *sustained*. Damped oscillations were easily distinguishable through visual inspection of $V(t)$. An example of damped oscillations along with the Fourier spectrum for $V(t)$ can be seen in figure 0.14.

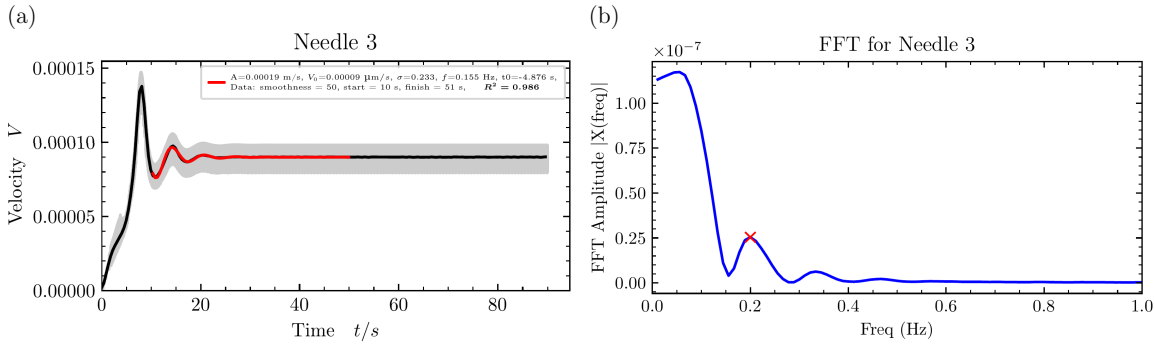


Figure 0.14: Damped oscillatory behavior for needle number 3 in the simulation V9_N10_D3.k0.14_AlCu_630x398 (condensed notation). (a) Dendrite growth velocity versus time along with the fitting (red line), and (b) Fourier spectrum for estimating the initial frequency (f) before the fitting.

Figure 0.15 displays the growth behavior map (A) concerning pulling velocity V_p and primary spacing Λ . Sustained oscillatory growth was achieved across a range of (V_p, Λ) , but oscillations were only observed for $V_p \geq 60 \text{ } \mu\text{m/s}$. Most sustained oscillations (\bullet symbols) occurred within a primary spacing range of $190 \leq \Lambda/\mu\text{m} \leq 270$, while damped oscillations (\blacktriangledown symbols) were found within $120 \leq \Lambda/\mu\text{m} \leq 190$.

Symbol colors represent the ratio of average fluid velocity \bar{V} to pulling velocity V_p : light green ($\bar{V}/V_p \leq 0.05$), medium blue ($0.05 \leq \bar{V}/V_p \leq 2.5$), or dark red ($\bar{V}/V_p \geq 2.5$). This color scheme effectively correlates well with the occurrence of damped, sustained, or noisy oscillations, except for a few data points near the transition between sustained and noisy oscillations. Refer to figure 0.16 for an example of damped oscillation behavior corresponding to the gray label 3.a and 3.b from figure 0.15.

These findings suggest that this phenomenon could be a general characteristic of binary alloys, given the appropriate conditions of temperature gradient (G), pulling velocity (V_p), and primary spacing (Λ). We confirmed that the ratio of average fluid velocity (\bar{V}) to pulling velocity (V_p) serves as a reasonable indicator of the oscillatory regime (i.e., damped, sustained, or noisy). However, the threshold values for \bar{V}/V_p differ from those observed in Isensee and Tourret previous study on CMSX-4 ($\xi_1 \approx 1.0$, $\xi_2 \approx 2.0$), suggesting a potential dependence on alloy parameters and processing conditions.

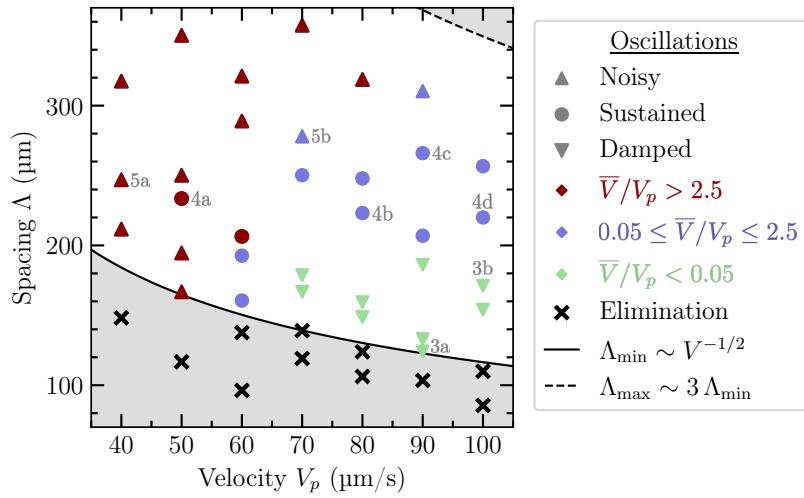


Figure 0.15: Oscillatory behavior map. Symbols types denote different growth behaviors: (\times) elimination events for $\Lambda < \Lambda_{\min}$ (black line) or (\blacktriangledown) damped, (\bullet) sustained, or (\blacktriangle) noisy oscillations. Symbols are colored according to the ratio \bar{V}/V_p . Gray text labels next to symbols mark cases for later discussions.

In this study, the transition from damped to sustained oscillations coincided with the appearance of convection vortices in the fluid, which contrasts with previous results for CMSX-4, where well-established convection rolls were present in both regimes. Our results did not capture the expected transition from sustained to damped oscillations with increasing V_p (cooling rate), possibly because it occurs at higher V_p values than those explored in this study. Additionally, the influence of the boundary condition at the solid-liquid interface, such as the imposition of null velocity, as opposed to other methods like accounting for the solid-liquid density change or tracking the solid fraction in a mushy region, remains to be investigated.

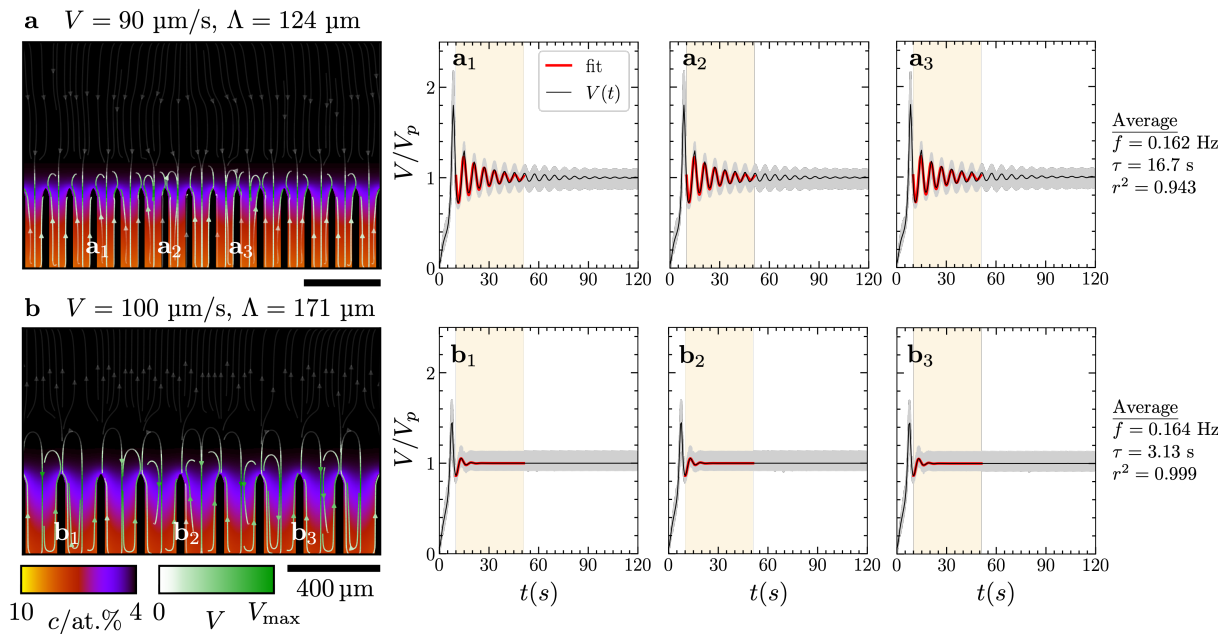


Figure 0.16: Damped oscillations (a) for $V = 90 \mu\text{m/s}$ and $\Lambda = 124 \mu\text{m}$ and (b) for $V = 100 \mu\text{m/s}$ and $\Lambda = 171 \mu\text{m}$. (left) Concentration field (color map) and fluid flow (streamlines) at $t = 120 \text{ s}$. Streamlines are progressively transparent toward lowest velocities (from opaque at $V/V_{\max} \geq 0.2$ to 90% transparent at $V = 0$). (right) Tip velocities of selected needles, showing raw (gray) and smoothed (black) $V(t)$ as well as fitted function (thick red) and range (shaded background).

UNESCO Codes

- [120326] - Simulations
- [221101] - Alloys
- [221106] - Dendrites
- [120903] - Data Analysis

Keywords:

Computational Material Science, Dendritic Needle Network, GPUs, Directional Solidification.

GitHub repository:

A GitHub repository has been established, housing the bespoke Python scripts used for the data post-processing and for the simulations launch automation.

Repository Link: <https://github.com/jbarciv/DNN-FittyPlot>

The main results of Sec. 5.2 and 5.3 of this thesis have been published in

J. M. Barberá, T. Isensee, and D. Tourret. “On the occurrence of buoyancy-induced oscillatory growth instability in directional solidification of alloys”. In: *IOP Conference Series: Materials Science and Engineering* 1281.1 (May 2023), p. 012050. doi: [10.1088/1757-899X/1281/1/012050](https://doi.org/10.1088/1757-899X/1281/1/012050). url: <https://dx.doi.org/10.1088/1757-899X/1281/1/012050>.

This study was supported by the Spanish Ministry of Science and Innovation through the María de Maeztu seal of excellence of IMDEA Materials Institute (CEX2018-000800-M).

Table of Contents

ACKNOWLEDGEMENTS	iv
EXECUTIVE OVERVIEW	xii
LIST OF TABLES	xxiii
LIST OF FIGURES	xxv
CODES INDEX	xxvi
1 INTRODUCTION	1
1.1 Motivation	1
1.2 State of the Art	2
1.3 Objectives	2
2 DENDRITIC GROWTH	4
2.1 Introduction	4
2.2 Phase diagram	4
2.3 Solidification and Dendrites	7
2.3.1 Nucleation and Undercooling	8
2.3.2 Dendrites	9
2.4 Directional Solidification	11
2.5 Role of Natural Convection	15
2.6 Scale Range and Numerical Models	17
2.6.1 Atomistic Models	17
2.6.2 Phase-Field	18
2.6.3 Grain Envelope	18
2.6.4 Cellular Automaton	19
3 DENDRITIC NEEDLE NETWORK MODEL	21
3.1 DNN history	21

Table of Contents

3.2	Directional Formulation	23
3.2.1	Scaled Equations	25
3.3	Numerical Implementation	26
3.3.1	Discretization of Space and Equations	26
3.3.2	Growth of Dendritic Branches	27
3.3.3	Parallelization	28
3.3.4	Moving Domain	28
4	SIMULATIONS	30
4.1	Motivations	30
4.2	Theoretical background	31
4.3	Launching	32
4.3.1	Cluster, GPUs and Slurm	32
4.3.2	Workflow	33
4.3.3	Planning	35
4.3.3.1	[A, B, C]: Simulations with $D = 3 \times 10^{-9}$ m ² /s, for $k = 0.1, 0.14$ and 0.2	36
4.3.3.2	[D]: Simulations with $D = 1.5 \times 10^{-9}$ m ² /s, for $k = 0.14$	37
4.4	Data Output	38
4.5	Data Post-Processing	39
4.5.1	Plotting and Averaging	39
4.5.2	Fitting	40
5	RESULTS	43
5.1	Scope of Research	43
5.2	Oscillatory Behavior Map	44
5.3	Discussion	44
5.3.1	Elimination ($\Lambda < \Lambda_{\min}$)	44
5.3.2	Damped oscillations ($\Lambda \gtrsim \Lambda_{\min}$)	44
5.3.3	Sustained oscillations (intermediate Λ)	45

5.3.4	Noisy oscillations (high Λ)	47
6	CONCLUSIONS AND FUTURE WORK	49
6.1	Conclusions	49
6.2	Future Work	50
	REFERENCES	51
	ANNEXES	62
C	Work Breakdown Structure	62
D	Time Planning	62
E	Budgeting	62

LIST OF TABLES

2.1	Nominal composition of the CMSX-4 superalloy [90].	15
3.1	Main stages in DNN history from early 2000's to the present.	22
4.1	Simulation parameters for the mapping of V_p and Λ	32
4.2	Summary of GPUs per node and available models in the IMDEA Materials GPU cluster	33
4.3	Overview of our four simulation groups, each exploring unique aspects of the binary alloy's behavior.	36
4.4	Simulation parameters for scanning each of the first three group simulations. With $W_y = 630$ for the width of the domain.	36
4.5	Simulation parameters for scanning each of the first three group simulations. With $W_y = 1470$ for the width of the domain.	37
4.6	Simulation parameters for scanning the last simulation group (D). With $W_y = 630$ for the width of the domain.	37
4.7	Simulation parameters for scanning the last simulation group (D). With $W_y = 1470$ for the width of the domain.	37
E.1	Estimated Electricity Costs for Simulations.	63
E.2	Allocation of Human Resources.	63
E.3	Overview of Computer Resources Utilized	64

LIST OF FIGURES

1.1	Dassault Mirage jet engine blades.	1
1.2	Oscillatory growth behavior discovered using <i>in-situ</i> X-ray radiography during the directional solidification of a CMSX-4 superalloy [90]	2
2.1	Phase diagram of total solubility in solid and liquid state of a binary alloy.	5
2.2	Linearized segment of a phase diagram for a binary alloy.	6
2.3	Schematic about planar and dendritic growth.	9
2.4	Anisotropic Surface Energy in 2D and 3D Crystals.	10
2.5	Dendrites review: schematic of dendrite branches, succinonitrile dendrite tip, spot-weld superalloy, dendritic growth in a snowflake, equiaxed dendrite from phase-field simulation.	12
2.6	Schematic representation of the vertical continuous casting process and the resulting dendritic microstructure in ingots.	13
2.7	Schematic diagram of a Bridgman furnace and the novel GaTSBI technique.	13
2.8	Turbine blades: from equiaxed, to directional solidified, to single crystal.	14
2.9	Bicrystalline nickel-based superalloy turbine blade formed by directional solidification.	15
2.10	Convection and growth patterns in directional solidification: experimental and simulated studies.	16
2.11	Different scales of solidification, along with their corresponding computational models.	17
2.12	Computer simulation of pure Ni: exploring the moving boundary between solid and liquid phases through φ measurements.	18
2.13	Predicting equiaxed dendrite formation in supersaturated binary alloy through phase-field approach: a study on diffuse interface and atomic structure via φ order parameter.	19
2.14	Simulating isothermal growth of randomly distributed and oriented grains in cubic enclosure with supersaturation $\Omega_0 = 0.05$	19
2.15	Exploring computational space and setup of 2D cellular automaton for dendrite envelope grain growth.	20
3.1	DNN 2D simulations using the first implemented version of Tourret and Karma's model with infinitely sharp needles.	22
3.2	Schematic illustration of the dendritic needle network approach for both: (i) the infinitely sharp and (ii) the finite thickness implementation.	23

3.3	Schematic illustration of the dendritic needle network approach for both: (i) the infinitely sharp and (ii) the finite thickness implementation.	24
3.4	Two-dimensional staggered finite difference grid for the numerical implementation of the DNN model.	27
3.5	Numerical approach for the approximation of the circular contour and the dendritic needle using discrete steps for the calculation of the flux intensity factor $\mathcal{F}(t)$	28
3.6	Schematic representation of a moving simulation domain in the DNN model for directional solidification.	29
4.1	Screenshot from ParaView, visualizing simulation results.	38
4.2	Illustration of functions $v_1(t)$ and $v_2(t)$ for $V_0 = 8.0$, $A = 1.5$, $f = 2.0$, $t_0 = 0.0$ and different values of τ (Eq. (4.1)) or S (Eq. (4.2)).	40
4.3	Sustained oscillation behavior for simulation V9_N7_D3_k0.14_AlCu_630x398. Plot of dendrite growth rate versus simulation time along with the fitting.	41
4.4	Damped oscillatory behavior for simulation V9_N10_D3_k0.14_AlCu_630x398. Plot of dendrite growth rate versus simulation time along with the fitting.	41
4.5	Fourier spectrum and the identified frequency component for $V(t)$ from Fig. 4.4.	42
5.1	Oscillation characterization maps for the Al-4at.%Cu alloy	43
5.2	Oscillatory behavior map A: $D = 3 \times 10^{-9}$ m ² /s, for $k = 0.14$	45
5.3	Damped oscillations.	46
5.4	Sustained oscillations.	47
5.5	Noisy oscillations.	48
E.1	Work Breakdown Structure (WBS). Hierarchical project breakdown, for the visualization of project components and deliverables, facilitating their orderly execution.	65
E.2	Gantt Diagram (part 1): first part of the research corresponding to the duration of the RIF (Research Initiation Fellowship) at IMDEA Materials.	66
E.3	Gantt Diagram (part 2): last part of the research corresponding to the analysis and the documentation for the Bachelor's Thesis.	66

CODES INDEX

4.1	Slurm manager launch file example.	33
4.2	Python script demonstrating the automation of simulation setup.	34
4.3	Smoothing algorithm for raw velocity.	39
4.4	Implemented Fast Fourier Transform (FFT) function used for analyzing the velocity signal.	42

1 INTRODUCTION

1.1 Motivation

Studying dendrites is intrinsically tied to technological considerations, especially within the domain of material science. This is attributed to the fact that in various industrial processes such as casting, welding, or soldering, dendritic solidification in metallic alloys leads to notable spatial variations in alloy concentration within the solidified material, referred to as microsegregation. Furthermore, this process may result in the formation of new phases in the interdendritic region, as highlighted in previous research [34, 9]. These phenomena hold immense significance as they directly influence the mechanical strength of the final solidified product. Therefore, an extensive comprehension of the complete solidification process, encompassing the growth of primary and secondary dendritic branches, as well as the subsequent coarsening of these branches during the solidification of the interdendritic liquid, stands as a crucial requirement to ensure the mechanical integrity of the end product.

Furthermore, alternative solidification techniques, such as directional solidification (DS), play a crucial role in the manufacturing of exceptionally robust components known for their extraordinary thermal and mechanical resilience. As depicted in Fig. 1.1, turbine and engine blades, typically composed of single-crystal Ni-based alloys, serve as a prominent example. However, the manufacturing process for these turbines is often plagued by common defects, including freckles and segregated channels [25, 93, 52, 85], which result in the wastage of produced parts. Consequently, achieving a profound understanding of the conditions that promote stable and homogeneous DS is an essential step toward advancing the next generation of directionally solidified components. These considerations underscore the dual significance of dendrite and directional solidification research within the realm of material science and technology.



Figure 1.1: Dassault Mirage jet engine blades captured by Josep María Barberá during a visit to CMT-Motores Térmicos at Universidad Politécnica de Valencia (UPV).

1.2 State of the Art

In a recent experimental study, solutal buoyant flow was directly observed using *in-situ* X-ray radiography during the directional solidification of a CMSX-4 superalloy [90]. The influence of melt flow became evident through the tracking of dendritic tip growth velocities. These tip velocities displayed oscillations depending on the applied cooling rate.

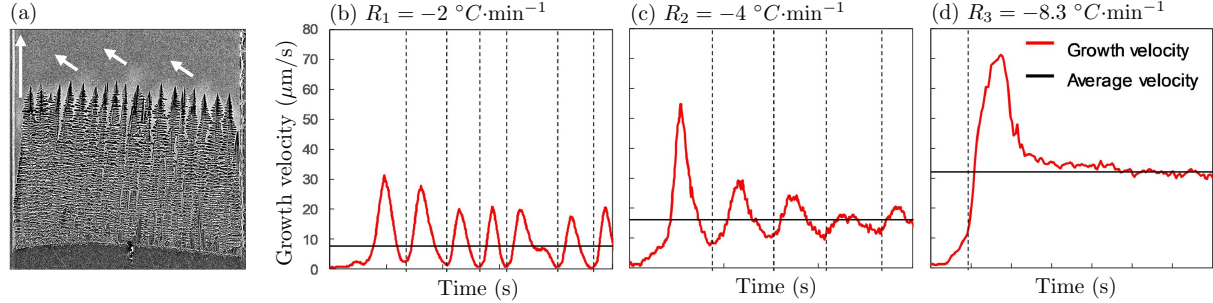


Figure 1.2: Oscillatory growth behavior discovered using *in-situ* X-ray radiography during the directional solidification of a CMSX-4 superalloy [90]. Time evolution of the growth velocity for dendrites shown in (a). The black horizontal lines in the growth velocity plots correspond to the average velocities and are (b) $7.6 \mu\text{m/s}$, (c) $15 \mu\text{m/s}$ and (d) $31 \mu\text{m/s}$ for the cooling rates of (b) $-2 \text{ }^{\circ}\text{C}/\text{min}$, (c) $-4 \text{ }^{\circ}\text{C}/\text{min}$ and (d) $-8.3 \text{ }^{\circ}\text{C}/\text{min}$. White arrows in (a) indicate the direction for solutal convective flow after solidification of the network.

From a modeling perspective, accurately simulating dendritic growth under convective conditions remains a challenging endeavor due to the presence of multiple length scales. To address this, Isensee and Tourret employed the dendritic needle network (DNN) model in conjunction with an efficient Navier-Stokes solver. Through these simulations, they successfully replicated the buoyancy-induced growth oscillations observed in CMSX4 directional solidification [56].

It's worth noting that the current DNN model, which operates within a two-dimensional framework and considers a model binary alloy, may not entirely capture the intricate interactions of multicomponent solutes in a three-dimensional sample. Nonetheless, previous results demonstrated that, by carefully employing a pseudo-binary alloy approximation, DNN simulations could replicate this oscillatory growth behavior.

These previous findings have shed light on the fact that, for a given alloy and temperature gradient, oscillations manifest within a specific range of cooling rates (or pulling velocity, V_p). Additionally, the chosen primary dendrite arm spacing (Λ) was identified as a critical factor influencing the onset of flow-induced oscillations.

However, several questions remain unanswered from this research. Is this behavior generalizable to other types of alloys, and what are the specific solidification conditions that trigger this phenomenon? These inquiries form the basis for further investigation in this field.

1.3 Objectives

Here, we show that the oscillatory behavior may be generalized to other binary alloys within an appropriate range of (V_p, Λ) by reproducing it for an Al-4at.%Cu alloy. We perform a mapping of oscillatory states as a function of V_p and Λ , and identify the regions of occurrence of different behaviors (e.g., sustained or damped oscillations) and their effect on the oscillation characteristics. Our results suggest a minimum of V_p for the occurrence of oscillations and

confirm the correlation between the oscillation type (namely: damped, sustained, or noisy) with the ratio of average fluid velocity \bar{V} over V_p . We describe the different observed growth regimes and highlight similarities and contrasts with previous results for a CMSX4 alloy.

To effectively present and explain the results, along with the computational work conducted, this thesis is structured into six chapters, excluding the current one.

- **Chapter 2** establishes the foundational concepts of solidification theory, covering directional solidification, the importance of fluid flow and natural convection in metals, and modern computational models for studying solidification processes.
- **Chapter 3** centers on the DNN model, the primary focus of this research. It reviews its history, associated research developments, and provides a brief overview of the mathematical framework, extending to fluid flow in 2D. The chapter also discusses, at the end, the numerical implementation model.
- **Chapter 4** encompasses all aspects of simulations. It begins with an introduction discussing research motivations and the current field status. The chapter then details the hardware used, simulation launch procedures, techniques for visualizing simulation data, and the implemented workflow automation and data analysis code.
- **Chapter 5** defines the research scope and presents the main results in a comprehensive discussion.
- **Chapter 6** serves as the conclusion, offering concise reflections on the academic insights gained during the thesis development, summarizing the research findings, highlighting alignment with Sustainable Development Goals, and discussing potential future research directions.

2 DENDRITIC GROWTH

Some theoretical concepts about metallic materials and the solidification theory should be detailed and are necessary before starting with the specific results of this thesis.

In the first section of this chapter shorts paragraphs introduce us to the world of casting and solidification. Then, following sections, i.e., 2.2, 2.3 and 2.4, define the relevant concepts of phase diagrams. Dendrites are presented and described as well as directional solidification as a relevant example. The last two sections, 2.5 and 2.6, discuss the role of natural convection in dendrite growth and scale ranges in relation to the numerical models that can be found in literature.

The main sources consulted regarding the sections of this chapter are summarized below:

- Section 2.2:

V. Blázquez, V. Lorenzo and B. del Río, *Ingeniería y Ciencia de los Materiales Metálicos*, Madrid, [Dextra Editorial](#) (2014).

- Sections 2.3 and 2.4:

J. A. Dantzig, M. Rappaz, *Solidification (2nd Edition)*, EPFL Press, [www.solidification.org](#) (2016).

D. R. Askeland, P. P. Phulé, W. J. Wright, and D. Bhattacharya. *The science and engineering of materials*. 6th ed. Springer (2003).

- Sections 2.5 and 2.6:

T. Isensee, *Multiscale modeling of dendritic growth kinetics with liquid convection*, PhD thesis, ETSI Caminos Canales y Puertos, (Defended January 18, 2023).

2.1 Introduction

The casting of metals dates back around 7000 years. The oldest surviving casting is a copper frog from ancient Mesopotamia around 3200 BC [89]. Since then until now, solidification has been probably the most important processing technique used in the manufacture of materials. Despite the fact that technology and science have developed rapidly, the same methodology for casting continues to be used in general terms.

A brief description of the casting process is given below. The process starts by heating the metal above the melting point. Heating is then maintained so that the metal is fully liquid just before it is poured into the mould. Finally, the metal solidifies into the desired shape, and the metal part (the casting) can be extracted. At this point, some questions may arise: Why does solidification occur? Is there a main characteristic parameter? How does solidification evolve within the liquid metal? These and other questions will be addressed in the following sections.

2.2 Phase diagram

In order to have the necessary tools for the study of solidification, some concepts should be reviewed: the definition of alloy and phase, the characteristics of a phase diagram and the parameters that can be extracted from it, i.e., the partition coefficient.

Except in very specific cases, pure metals have no industrial applications, and alloys must be used in order to obtain the combination of the required properties for a given application e.g., machining tools or structural components. The *alloys* are macroscopically homogeneous, usually obtained from casting and more recently from powder sintering i.e., the process of applying pressure and temperature without actually melting. From a microscopic view, metallic alloys are composed of atoms of two or more elements, where at least one of them is a metal.

Phases can be defined as *each of the physically separable homogeneous parts in a system consisting of one or more components*. In addition, the properties of the alloy depend on the nature, percentage, morphology, size and distribution of its phases.

The different stable zones of the components for binary alloys can be represented in a *temperature-composition* diagram. That is called, a *phase diagram* (see FIG. 2.1). These diagrams define for any temperature the phases that will compose an alloy of two metals, as well as their respective mass or molar fraction. Since, the properties of an alloy depend on their phases, these diagrams will allow us to understand the properties that a given alloy presents.

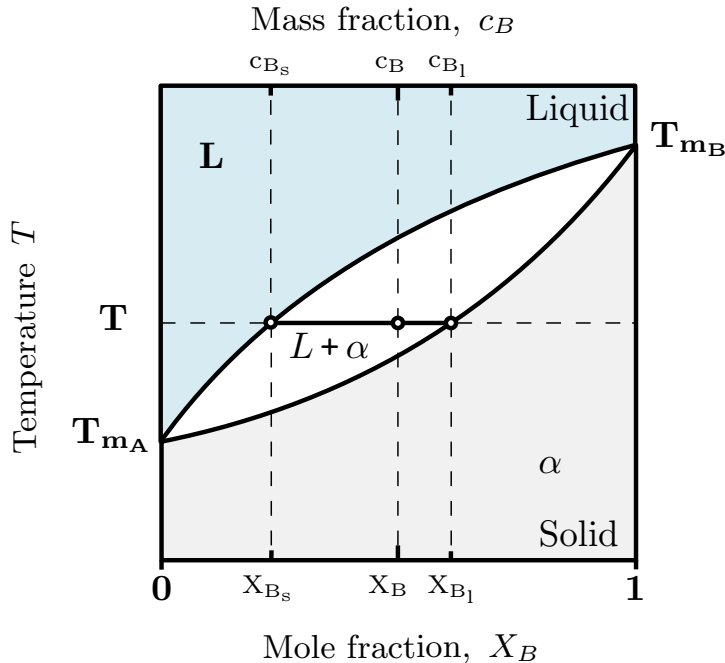


Figure 2.1: Phase diagram of total solubility in solid and liquid state of a binary alloy in terms of mole fraction X_B and mass fraction c_B , showing solidus and liquidus lines and the coexistence of solid and liquid phase (white). Where T_m is the melting temperature of pure metals and T is the current temperature.

Equilibrium diagrams correspond to the thermodynamic evolution of a system, i.e, infinitely slow in cooling and heating processes. Then, when an alloy is cooled at speeds far from those, the situation can vary significantly from the one predicted by the diagram.

Given the phase diagram in Fig 2.1, the *partition coefficient* at temperature T can be defined as:

$$k = \frac{X_{B_s}}{X_{B_l}} = \frac{c_{B_s}}{c_{B_l}} \quad (2.1)$$

it determines the extent to which solute is ejected into the liquid during solidification. Furthermore, it is frequently observed that the parameter k is less than one, indicating that the solid phase being formed possesses greater purity than the liquid phase [16].

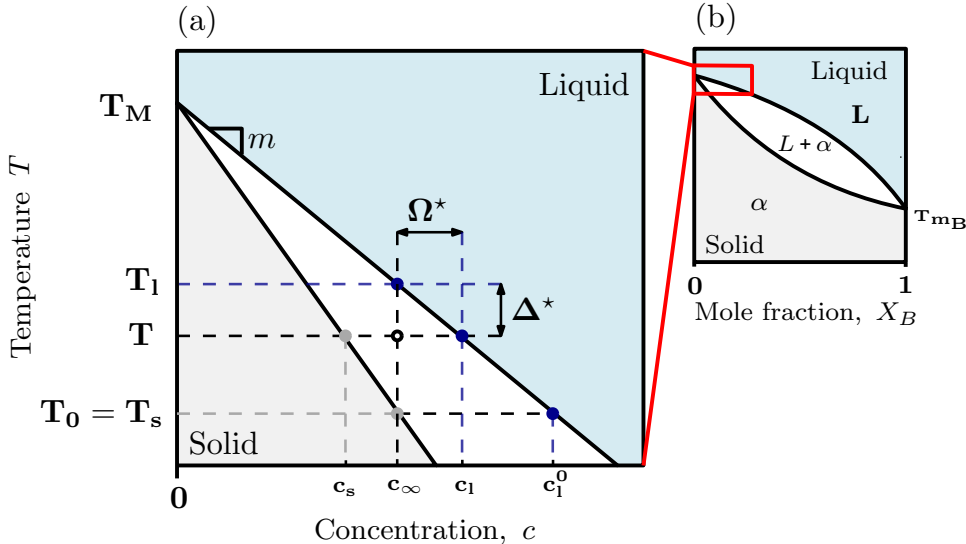


Figure 2.2: (a) Linearized segment of a phase diagram for a binary alloy with nominal concentration c_∞ and reference temperature $T_0 = T_s$. The segment shows the liquidus slope denoted by m , the liquidus and solidus temperatures at nominal concentration denoted by T_l and T_s , respectively, as well as the undercooling and supersaturation denoted by Ω^* and Δ^* , respectively. This segment is located very close to pure component A (when $X_B = 0$) in the full binary alloy phase diagram, shown in part (b).

An idealized segment of a phase diagram for a binary alloy can be seen in Fig 2.2. Since the area of the diagram on which we will focus (with respect to the complete diagram, figure 2.2b) is very small, drawing the *liquidus* and *solidus* curves as straight lines is correct and often convenient. In this particular situation, the slope of liquidus will be constant and negative, $m < 0$. At the beginning for the nominal concentration c_∞ and above the liquidus temperature T_l all the metal will be molten. Once the temperature drops below T_l solidification begins. For the current temperature T , supersaturation can be written as follows:

$$\Omega^* = c_l - c_\infty \quad (2.2)$$

and the undercooling:

$$\Delta^* = T_l - T \quad (2.3)$$

where c refers to the concentration, the value of c at equilibrium in the liquid will be called c_l and for the nominal concentration it will be used c_∞ . Also, T_l is the liquidus temperature, i.e. above which all the metal is molten. Finally, T is used as the instantaneous temperature of the alloy.

Note that the superscript “ $*$ ” is used in these equations to differentiate these parameters from their dimensionless version, which are defined below. This is because the dimensionless parameters will be of great use later in the simplification of solidification model equations. Despite these brief definitions, a deeper understanding of the meaning and implications that undercooling and supersaturation have on solidification will be discussed in the next sections.

The dimensionless version of undercooling and supersaturation can be defined as follows:

$$\Delta := \frac{T_l - T}{T_l - T_s} \quad (2.4)$$

$$\Omega := \frac{c_l - c_\infty}{(1 - k)c_l} \quad (2.5)$$

The latter can be related to the dimensionless undercooling Δ (2.4) via

$$\Omega = \frac{1}{1-k} \left[1 - \frac{1}{1 - (1 - \frac{1}{k})\Delta} \right] \quad (2.6)$$

and conversely

$$\Delta = \frac{k}{k-1} \left[1 - \frac{1}{1 - (1-k)\Omega} \right] \quad (2.7)$$

It is interesting to note how a triangular construction in the linearized phase diagram (see FIG. 2.2a) allows to obtain some of its parameters thanks to the liquidus slope. For instance, the liquid equilibrium concentration at the reference solid temperature T_0 may be expressed as:

$$c_l^0 = \frac{T_0 - T_M}{m} \quad (2.8)$$

2.3 Solidification and Dendrites

Once the basic definitions have been established, the solidification process and the formation of dendrites can be explored.

The process of solidification is induced by a departure from equilibrium, in the form of an undercooling (departure from equilibrium temperature) or supersaturation (departure from equilibrium concentration). Starting from the liquid state, crossing the liquidus line produces this departure from equilibrium. To measure this distance from equilibrium, two coordinates can be used: undercooling on the temperature axis and supersaturation on the concentration axis (see FIG. 2.2). For pure metals, solidification is induced by undercooling only, and the transformation kinetics are primarily limited by the transport of heat. For alloys, solidification kinetics depends on both temperature and solute fields. However, since the transport of solute is usually several orders of magnitude slower than that of heat, solidification kinetics for alloys are typically limited by solute transport, and can be idealized considering a locally isothermal domain at a given solute supersaturation. Despite these differences, the resulting underlying mechanisms are similar (namely interface capillarity and bulk diffusion [67]) and hence equations for thermally-driven pure metal solidification and solute-driven alloy solidification are nearly identical (i.e. replacing heat diffusivity by solute diffusivity, latent heat rejection by solute rejection at the interface, etc.). Hence, for the sake of clarity, in the current section, we only present the case of thermally-driven pure metal solidification, but the concept and equations are also relevant to alloys.

It is also remarkable to mention how the diffusion limited transport of mass and/or heat on a macroscopic scale and the anisotropic surface tension at the atomic scale are coupled. The combined effect of these two phenomena results in the production of a diverse range of branched patterns, which have been extensively studied in experimental research [1, 18, 73].

The first part of this section examines the initial formation of solid, also known as nucleation, in a pure metal and the important role that undercooling plays in the subsequent development of dendrites. The second part focuses on dendrites themselves, beginning with a brief discussion of the instability that can occur in the morphology of the growing solid and then moving on to define their key properties.

2.3.1 Nucleation and Undercooling

In general terms, the process of solidification begins thanks to nucleation, that is, when the formation of the first nanocrystallites (known as *nuclei*) from the molten material occurs. At the time a stable nucleus is formed and more number of atoms adhere to the solid-liquid interface, it is possible to talk about growth.

When discussing nucleation, it is important to note that the process can happen in two ways: through homogeneous nucleation and through heterogeneous nucleation. Homogeneous nucleation happens within a pure liquid, without the involvement of external particles. On the other hand, heterogeneous nucleation occurs when the presence of foreign substances promotes the process of nucleation [81].

The effects of nucleation in the solidification microstructure have a major influence on the grain size, morphology, extent of segregation, and compositional homogeneity. In the case of casting solidification, nucleation plays also a vital role, largely controlling the initial structure type, size scale, and spatial distribution on the product phases [95]. Other phenomena that occur in the later stages of ingot freezing, such as crystal growth, fluid flow (see Section 2.5 for natural convection influence) and structural coarsening, also modify the final microstructure [82].

The term *embryo* refers to a tiny solid particle that arises when atoms cluster together from a liquid. The embryo is not stable and can dissolve or grow into a stable nucleus. The process of embryo formation is statistical in nature. At thermodynamic temperatures of freezing or melting, the probability of creating stable and sustainable nuclei is very low. Consequently, solidification does not begin at these temperatures. If the temperature drops below the equilibrium freezing point, the liquid phase, which should have transitioned into a solid, progressively loses thermodynamic stability. This cooled liquid is known as undercooled. The disparity between the equilibrium freezing temperature and the current temperature of the liquid is denoted as *undercooling*. (Δ^* or ΔT), as mentioned in the previous section. As undercooling becomes more pronounced, the liquid's natural tendency to solidify becomes stronger, allowing for the formation of a solid-liquid interface.

The phenomenon of undercooling is significant in the creation of both equilibrium and nonequilibrium crystalline phases, as well as in the formation of amorphous phases. The degree of undercooling plays a crucial role in many practical aspects of solidification, including the evolution of morphology, the final structure of solidification, the manipulation or selection of phases, and the refinement of grain [83]. The underlying reason for this phenomenon is connected to the removal of two distinct types of heat during the solidification process: the specific heat of the liquid and the latent heat of fusion. The *specific heat* refers to the amount of heat required to either increase or decrease the temperature of a unit mass of material by one degree. It is imperative to eliminate the specific heat first, which can be accomplished through either radiation into the surrounding atmosphere or conduction into the adjacent mold. This initial phase involves cooling the liquid from its initial temperature to a point where nucleation begins. It is well-known that heat must be supplied to a solid in order to melt it. In contrast, during the formation of solid crystals from a liquid, heat is released, which is referred to as the *latent heat of fusion*. (ΔH_f). Before solidification can be completed, the latent heat of fusion must be removed from the solid-liquid interface. The technique employed to extract the latent heat of fusion affects the growth mechanism of the material and the final structure of the casting.

Regarding growth mechanisms, there are three types: cellular growth, planar growth and dendritic growth. But we will focus on the last two, emphasizing dendritic growth. In the case

of a well-inoculated liquid, containing nucleating agents, cooling under equilibrium conditions leads to heterogeneous nucleation without requiring any undercooling. As a consequence, the temperature of the liquid just ahead of the solidification front, defined as the interface between the solid and liquid phases, remains above the freezing point, while the solid itself is either at or below the freezing temperature. During the solidification process, the latent heat of fusion is conducted away from the solid-liquid interface. Any small protrusions on the interface are surrounded by liquid that is above the freezing temperature, as illustrated in Figure 2.3a. pauses until the remainder of the interface aligns with them, resulting in what is known as 'planar growth.' Planar growth occurs when a smooth solid-liquid interface advances into the liquid.

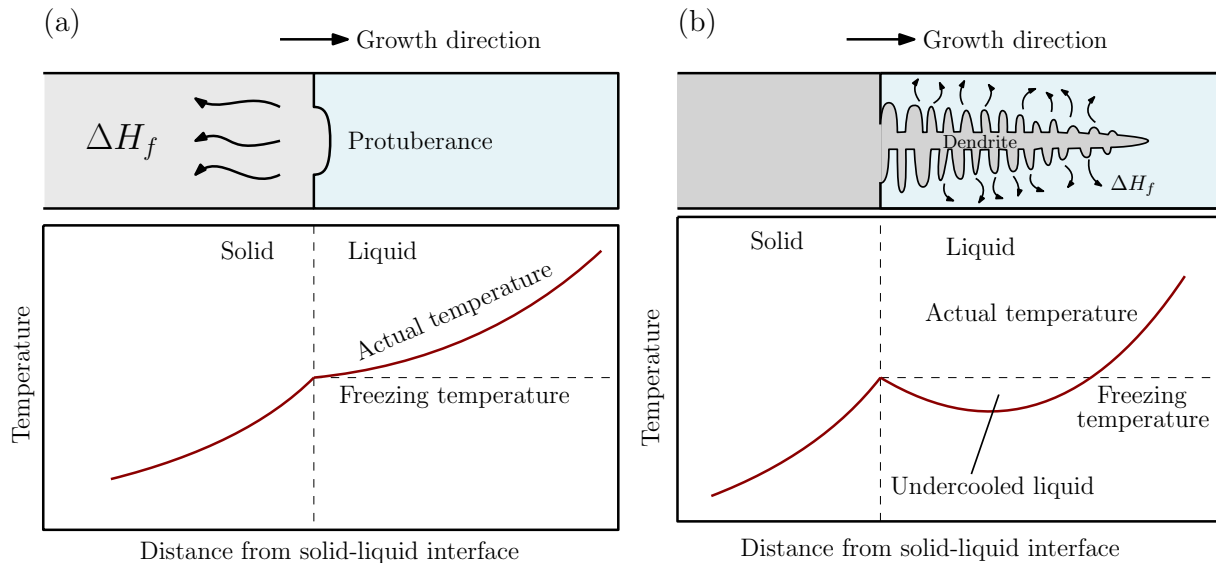


Figure 2.3: Schematics of two types of solidification growth: (a) planar and (b) dendritic, based on [2]. In planar growth, a solidification front advances with a stable interface, resulting in a smooth, flat structure. Dendritic growth produces a branching pattern due to the rapid growth of a protuberance on the solid-liquid interface, which then develops small arms extending from the main trunk. The type of growth that occurs is dependent on factors such as temperature and the rate of cooling or heating.

In the absence of inoculation and with poor nucleation, the liquid requires undercooling before solidification can occur (as shown in Fig 2.3b). At the solidification interface, a minor protrusion is prompted to expand due to the undercooling of the liquid ahead of the interface. As the solid dendrite grows, the heat of fusion is conducted into the undercooled liquid, gradually elevating its temperature toward the freezing point. To expedite the evolution of the latent heat, secondary and tertiary dendritic arms can also grow on the primary stalks. *Dendritic growth* continues until the undercooled liquid reaches the freezing point. Planar growth takes place when the remaining liquid solidifies. The distinction between planar and dendritic growth arises from the differing recipients of the latent heat of fusion. In planar growth, the container or mold absorbs this heat, whereas in dendritic growth, it is the undercooled liquid that absorbs the heat.

2.3.2 Dendrites

The previous paragraphs focused on the process of nucleation, which involves the initial formation of solid in a melt. During this process, the solid is typically treated as a sphere or a spherical cap. However, as the solid continues to grow, its spherical morphology becomes unstable, leading to the formation of dendrites.

The instability in the morphology of the growing solid is attributed to its tendency to adopt

preferred growth directions dictated by the underlying crystal structure. This preference is determined by anisotropy in either the surface energy of the solid-liquid interface or the ease of atom attachment on different crystallographic planes, or both.

Let us further consider the growth of dendrites in metals, particularly at low undercooling, where the anisotropy of the solid-liquid interfacial energy γ_{sl} is the primary determinant of the growth direction. Given the fundamental role that surface energy and its anisotropy play in dendritic growth, it is important to examine the mathematical representation of the associated equation. One common representation of surface energy in two dimensions is as follows:

$$\gamma_{sl} = \gamma_{sl}^0 [1 + \varepsilon_n \cos(n\phi)] \quad (2.9)$$

where, ϕ represents the azimuthal angle measured from a reference direction, ε_n denotes the magnitude of the anisotropy, and n signifies the degree of symmetry, e.g. $n = 4$ for a fourfold anisotropy for a cubic (fcc, bcc) system or $n = 6$ for a sixfold anisotropy of an hcp crystal in its basal plane. γ_{sl}^0 is the value of γ_{sl} , averaged over all orientations in a (100) plane. The more complex treatment of anisotropy in 3D can be found in Sec. 8.2.2 of [28]. The equilibrium shape for a crystal can be obtained via Wulff construction.

An example of the above is illustrated in Fig 2.4. There, the schematic (a) shows the anisotropic surface energy (red) with the Wulff construction (gray) for a crystal with $n = 4$ degrees of symmetry and $\varepsilon_4 = 1/7$. Also, subfigure (b) exhibits the surface energy γ_{sl} of 3D crystals with levels of cubic anisotropy comparable with those in schematic (a). After briefly discussing the morphological instability that arises from an elementary sphere during the solidification process in metals, it is easy to understand how anisotropy in surface energy can lead, under appropriate conditions, to the formation of dendrites.

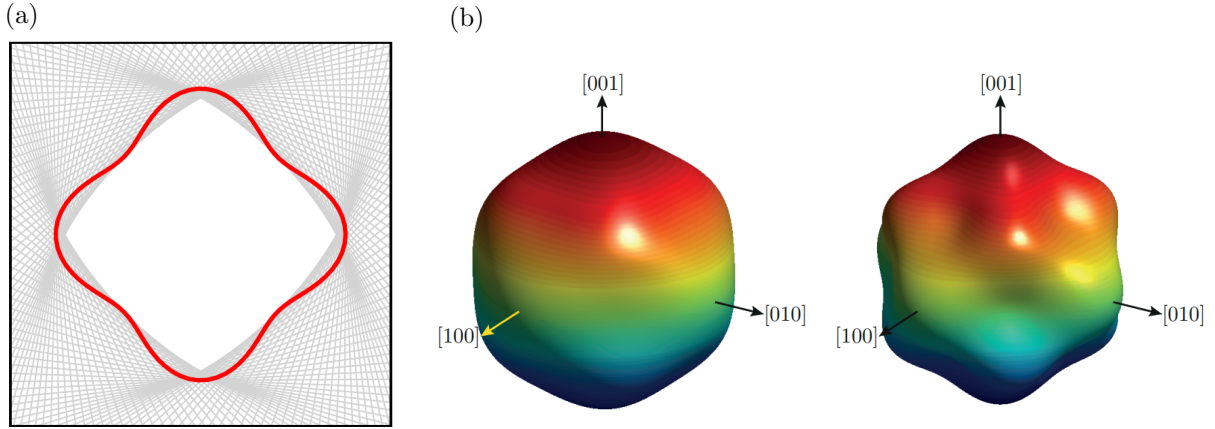


Figure 2.4: Anisotropic Surface Energy in 2D and 3D Crystals: (a) Schematic representation of anisotropic surface energy with the Wulff construction for a crystal with fourfold symmetry and a specific value of $\varepsilon_4 = 1/7$ [57], and (b) surface energy γ_{sl} of 3D crystals with cubic anisotropy levels comparable to those in schematic (a) [28].

The dendrite, which takes its name from the Greek word *dendron* meaning tree, is a structure that branches out into primary, secondary, tertiary, and higher-order branches, resembling the shape of a tree [111]. In Fig 2.5a, it can be seen an illustration of primary and secondary branches. Dendritic growth is a captivating form of crystallization process that has captured the interest of many, including artists, physicists, engineers, and applied mathematicians. One example of dendritic growth that is well-known is the formation of snowflakes (illustrated in Fig 2.5e).

This process produces intricate and complex patterns, filling the voids between the dendrite branches with eutectic or intermetallic phases [111, 45, 49]. The variation in growth conditions

controls the development of different length scales, such as dendrite tip radius, *primary spacing* (λ_1) and *secondary arm spacing* (λ_2), the latter two are indicated in Fig 2.5a.

The direct measurement of tip radius and tip growth rate as a function of undercooling was the driving force behind Glicksman et al. experiments in 1976 [46], which utilized a well-characterized transparent system, *succinonitrile*. The resulting images, such as those displayed in Fig 2.5b and 2.5d (see previous page), were a direct outcome of this research.

These length scales, i.e., dendrite tip radius, primary spacing and secondary arm spacing, characterize the solidification morphology, including the solute segregation pattern and the formation of a second phase (such as precipitates or pores) in the interdendritic region. The interarm spacings play a significant role in determining the casting mechanical properties that control the material [34, 35]. Dendritic growth is frequently observed in various contexts such as metal ingots, alloy castings, and weldments, particularly when metals and alloys solidify under modest thermal or concentration gradients, as documented in [97]. For instance, in Figure 2.5c, we can observe a prominent “dendritic forest” resulting from a spot-weld in a Ni-based superalloy.

Regarding the history of research of dendritic growth, an extensive review can be found in Ref. [67] and [68].

Figure 2.5f shows a three-dimensional equiaxed dendrite in a supersaturated binary alloy, which was predicted using the phase-field method and rendered with Blender (courtesy of Thomas Isensee). Although the phase-field model has not been discussed yet, the figure demonstrates how simulations can accurately reproduce the dendritic solidification pattern.

The microstructure in the casting of alloys is analyzed in relation to dendrites, as depicted in Fig 2.6. This figure provides a schematic representation of the vertical continuous casting process, which is known to produce the typical dendritic microstructure observed in ingots.

2.4 Directional Solidification

The previous study about nucleation and dendrites corresponds to free growth process, which involves the evolution of a single isolated solid particle in an infinite undercooled melt. A more common configuration is solidification from a chill surface, such as when a liquid is poured into a cold mold.

To better understand this process, it is convenient to discuss both *free growth* and *constrained growth* (also known as directional solidification), where many solid structures grow together under an imposed thermal gradient.

Free growth and directional solidification are the two types of dendritic structures that can develop under different growth conditions. Indeed, directional solidification is a process that involves creating a temperature difference or gradient, G_T , and then moving a sample through this gradient at a specific velocity, V_p . By doing so, it is possible to control the cooling rate of the sample, which is equal to the product of V_p and G_T :

$$\dot{T} = V_p G_T \quad (2.10)$$

This technique can be used to independently control the thermal gradient and growth velocity of dendritic structures. This allows for more precise control over the final properties of the material being produced [57] and the possibility to study specific microstructures under well known local conditions, e.g. solidification in casting.

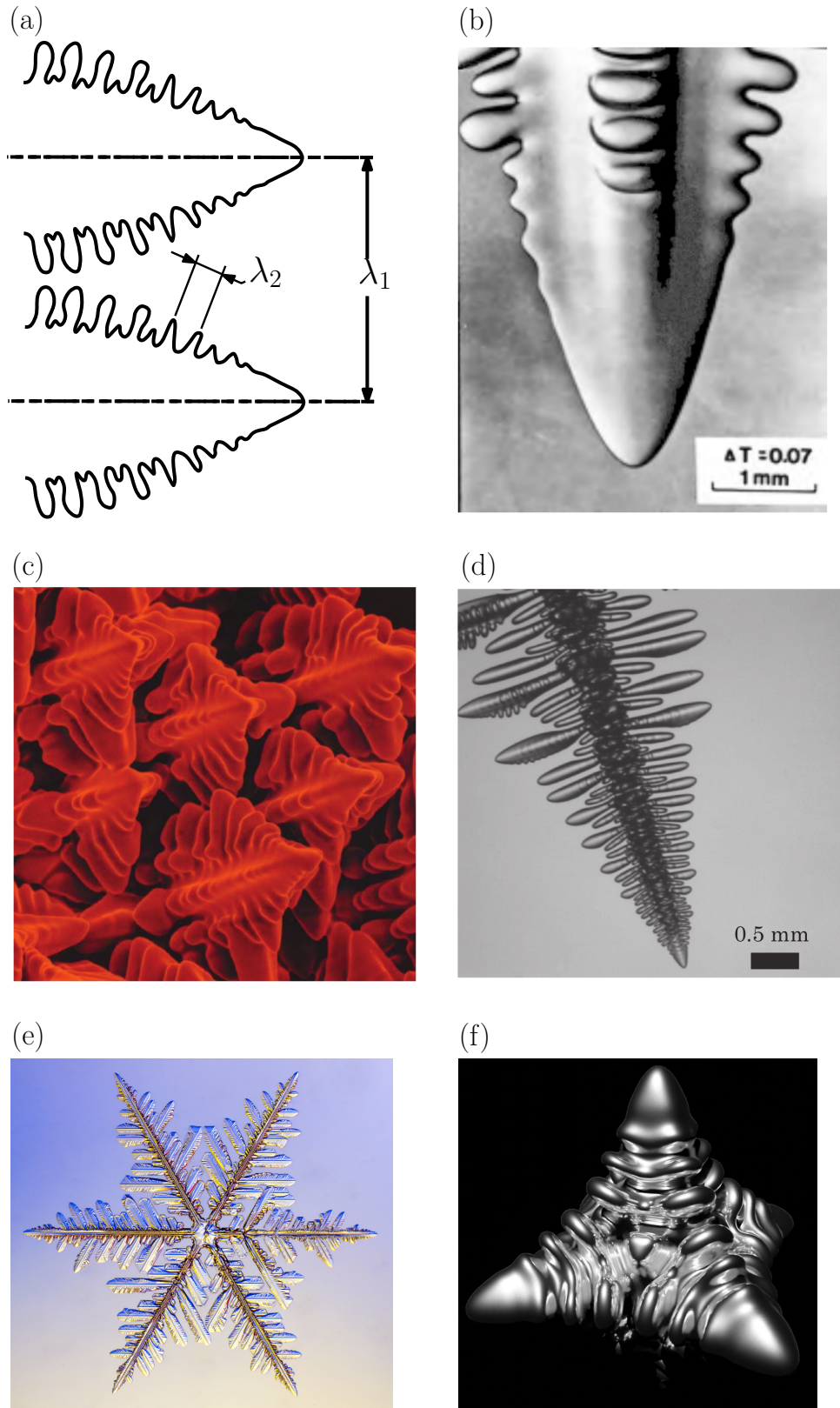


Figure 2.5: (a) Schematic illustration of primary and secondary dendrite branches with indicated primary and secondary arm spacings [95]. (b) Succinonitrile dendrite tip growth into an undercooled melt with $\Delta T = 0.07$ K [67]. (c) Spot-weld in a Ni-based superalloy [28]. (d) Micrograph of a pure succinonitrile dendrite solidifying in an undercooled melt with $\Delta T = 0.8$ K [28]. (e) Example of dendritic growth seen in the formation of snowflakes (from <http://www.snowcrystals.com/>). (f) Three-dimensional equiaxed dendrite in a supersaturated binary alloy predicted by the phase-field method and rendered with Blender (courtesy of Thomas Isensee).

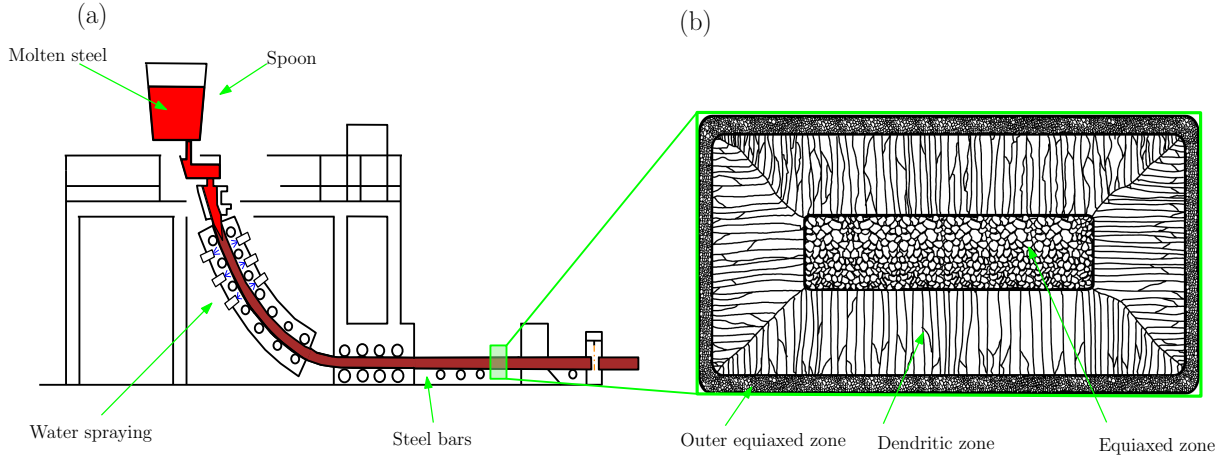


Figure 2.6: Schematic representation of the vertical continuous casting process and the resulting dendritic microstructure in ingots. (a) Illustrates the continuous casting process [32], while (b) shows a schematic of the dendritic microstructure typically observed in ingots after casting.

At this point, it is convenient to introduce the concept of *Bridgman furnace*. The idea is to have a well characterized and isolated environment in which to investigate the directional or equiaxed solidification [10]. A schematic of this type of furnace is shown in Fig 2.7a, while in Fig 2.7b a modern technique called GaTSBI (Growth at high Temperature using a Synchrotron Beam for Imaging) uses the underlying idea of the Bridgman furnace.

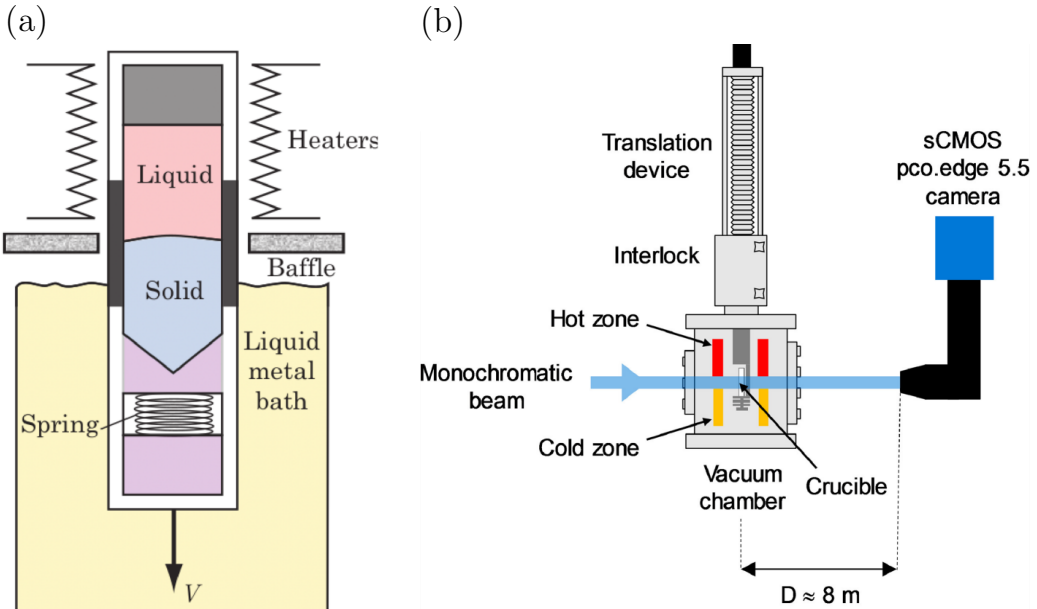


Figure 2.7: (a) Schematic diagram of a Bridgman furnace, reproduced from [57] based on [28]. (b) GaTSBI technique using the underlying concept of Bridgman furnace, reproduced from [90].

Directional solidification is a common technique used to manufacture various structures, including aligned eutectic structures, directional columnar structures, and single-crystal nickel-base superalloy turbine blades. Figure 2.8 displays three turbine blades arranged in the order of equiaxed, directional solidification, and single crystal, from left to right.

Unlike single crystals grown for electronic applications, single-crystal turbine blades intended for aerospace applications solidify with a dendritic structure. This leads to several benefits such as enhanced ductility, creep rupture, thermal resistance, and fatigue resistance [27]. Single-

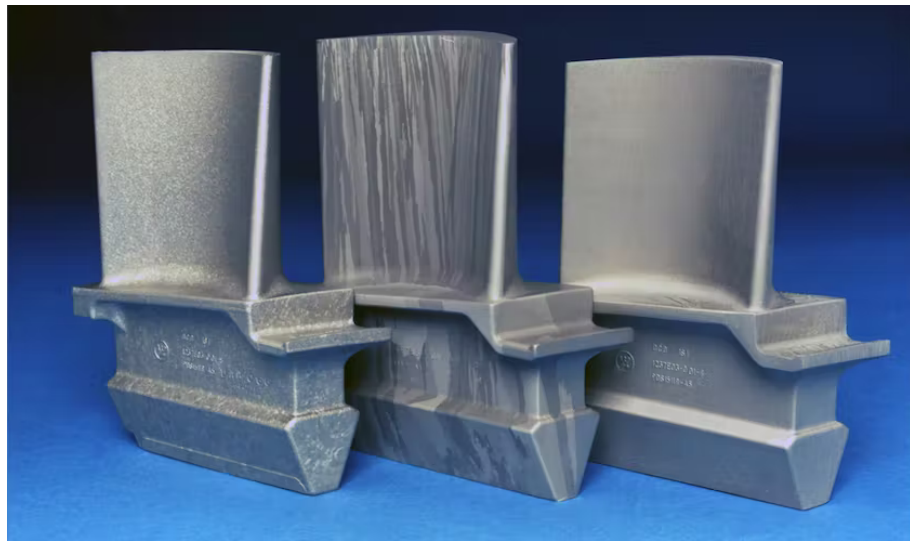


Figure 2.8: Evolution of turbine blades, depicted from left to right, transitions from equiaxed to directional solidified and finally to single crystal structures. (Photograph courtesy of Howmet Corp., sourced from [72].)

crystal turbine blades also offer advantages such as higher operating temperatures that result in increased engine fuel efficiency, improved durability, and longer lifespan at current operating temperatures. Furthermore, the absence of grain boundaries provides these blades with better corrosion resistance.

However, these turbine blades often contain microsegregation and second-phase particles formed by eutectic reactions. To achieve the desired grain structure, two conditions must be met: (1) the casting must extract heat in a unidirectional manner, and (2) the positive temperature gradient ahead of the solidifying interface must be controlled to prevent undesirable nucleation [84, 113].

The technique of *grain selection* is commonly employed in the manufacturing of directionally solidified and single crystal turbine blades. To improve the understanding of the underlying mechanism, it is relevant to present the following description, which is sourced from page 450 (section 11.4) of [28]:

Fig 2.9 “shows a simple blade cast using the lost wax process (...). In this case, the mold was covered by lateral insulating wool and attached to a water-cooled copper chill. As the melt is poured into the mold, many grains nucleate at the chill surface and start to grow. The grain selection process (...) occurs over the first few millimeters. Thus, the grains entering the helical “pig-tail” have their $\langle 100 \rangle$ directions aligned within $\approx 10^\circ$ of the vertical thermal gradient. The pig-tail eliminates most of the remaining grains, selecting those that can extend their secondary arms in the most efficient way into the first turn of the helix. After one turn in the helix, only a single grain emerges and starts to propagate by branching laterally into the entire blade. One can see that, in this particular blade, another stray grain nucleates before the arms of the main grain can reach the corner of the blade platform. If this stray grain is well-oriented with respect to the thermal gradient, it continues to grow, parallel to the initial grain, giving rise to the bicrystal blade seen here.”

Currently, *nickel-based superalloys* are the standard materials used for manufacturing blades

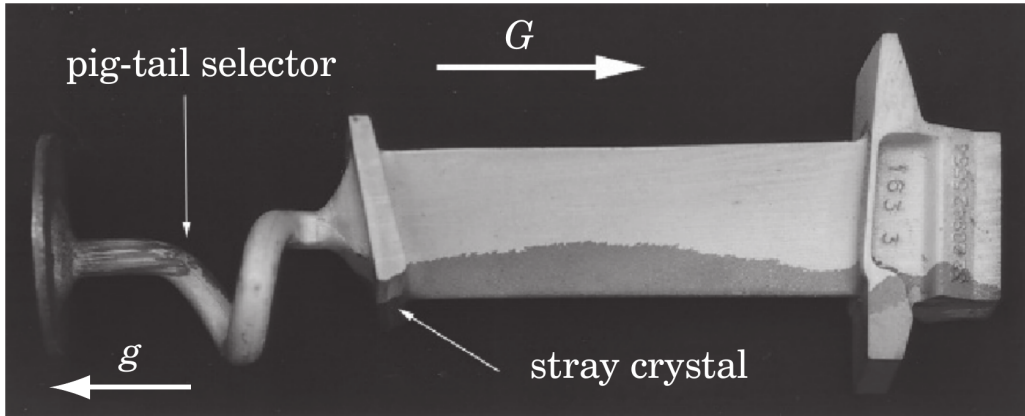


Figure 2.9: *Turbine blade made of a nickel-based superalloy with a bicrystalline structure that was formed via directional solidification. The thermal gradient in the vertical direction of the image progresses from left to right [28].*

in advanced turbine engines. The pursuit of greater turbine efficiency compels the utilization of materials that can withstand higher temperatures and stresses. However, opting for materials with enhanced mechanical properties can pose additional processing challenges [90].

CMSX-4 is a second-generation nickel-based superalloy that contains rhenium (Re) and has been extensively researched and documented in the literature [15, 103, 39, 50, 38]. The alloy's nominal chemistry is presented in Table 2.1. Since 1991, CMSX-4 has found application in a range of aero and industrial gas turbine uses, notably in high-pressure turbine blades and seals. It has consistently showcased a remarkable mix of attributes, encompassing high-temperature strength, robust phase stability, resistance to oxidation and hot corrosion, and outstanding coating performance, as corroborated by studies such as [65, 13, 14]. In fact, these properties have been proven during extensive engine service. As of 2004, nearly 5 million pounds (650 heats) of CMSX-4 had been successfully manufactured [51].

Element	Cr	Co	W	Al	Mo	Re	Ti	Hf	Ta	Ni
Composition c/wt%	6.5	9.6	6.4	5.6	0.6	3.0	1.0	0.1	6.5	Balance

Table 2.1: *Nominal composition of the CMSX-4 superalloy [90].*

Although third-generation CMSX superalloys, such as CMSX-4® Plus-Improved 3rd Generation SX Alloy [17], are currently under investigation and development, the 2nd generation CMSX-4 alloy with a 3% Re composition is still relevant. Indeed, a recent experimental study [90] identified oscillatory growth instabilities during directional solidification used this particular alloy. As a result, a comprehensive understanding of this alloy's properties is crucial for the investigation and interpretation of the phenomena observed in the study.

2.5 Role of Natural Convection

Transport phenomena play a crucial role in dendritic solidification and influence the formation and evolution of dendritic structures. While earlier sections only considered diffusion as the means of transporting solutes in the liquid melt, a deeper understanding of dendritic solidification requires studying other transport phenomena, such as fluid flow, solute and thermal gradients, and solutal buoyancy. By studying these factors, we can gain valuable insights into the formation of grain morphologies and defects in solid materials, which can ultimately help us to design and develop new materials with improved properties.

Fluid flow is one of the most important transport phenomena in dendritic solidification. During casting, the pouring of metal into a mold and natural convection induce fluid flow within the liquid as studied by [29, 74, 75]. The solute can be rejected at the growing interface due to different solubility of solid and liquid, resulting in solute gradients in the liquid. Thermal gradients are also induced by the release of latent heat of fusion. Solutal buoyancy is typically the dominant driving force of fluid flow during solidification of binary alloys, with expansion coefficients about 1-2 orders of magnitude larger. Both solute and thermal gradients lead to non-uniform density in the liquid and ultimately, under gravity, to buoyant flow. Fig. 2.10 illustrates the effect of melt flow on isothermal (equiaxed) and directional solidification.

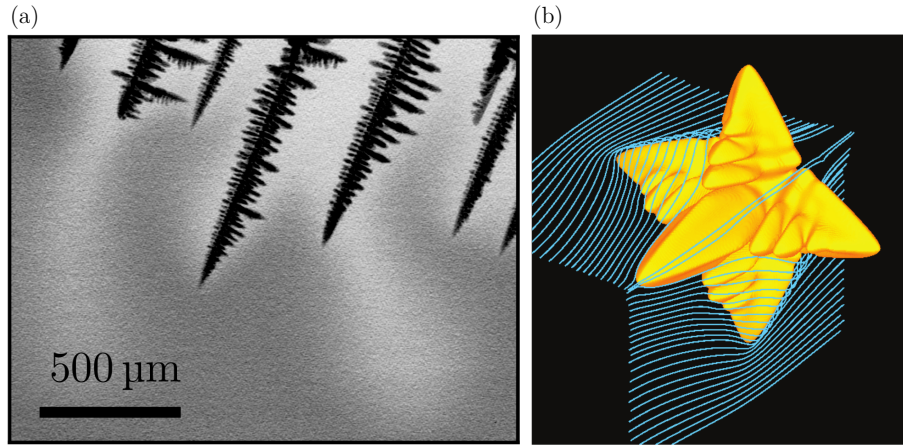


Figure 2.10: (a) Convection in directional solidification of Sn-39.5 wt%Bi (approx 27 %at.) with falling plumes of rejected tin (light shading indicates higher solute concentration) [44]. Note that the primary dendrites are inclined by an angle 23° with respect to the vertical temperature gradient and gravity and the growth is top-down (velocity and gravity aligned). (b) Phase-field method simulation of equiaxed dendrite under forced flow [28]. While the underlying crystal structure determines the direction of preferred growth, the branches facing upstream on the left side grow faster compared to those facing downstream on the right side.

To address the challenge of natural convection and achieve a purely diffusive regime (without the interference of fluid flow) for studying solidification, significant investments have been made to conduct experiments in reduced gravity conditions. These experiments are known to be expensive due to the specialized equipment and facilities required for creating and maintaining low-gravity environments [47, 77, 76]. However, fluid flow can become the dominant transport phenomenon and drastically alter solidification dynamics and resulting grain morphologies depending on the solidification conditions. Analytical studies have been done on the effect of melt flow on dendritic solidification and resulting grain morphologies [12]. Studies, such as [23], have revealed that fluid flow within the system agitates the liquid and decreases the solute boundary layer ahead of the solidification front. This effect leads to an extended range of stable velocities for the growth of the planar front. In addition, the presence of fluid flow significantly influences the selection of microstructural length scales, including parameters such as primary dendritic arm spacing, as indicated in studies such as [5, 30, 112].

As mentioned in the previous section, recent in-situ x-radiographies of directionally solidifying nickel-based superalloy CMSX-4 have shown flow-induced oscillatory growth behavior [90]. Convection effects during directional solidification in nickel-based superalloys can be associated with undesirable defects, such as freckles [43, 85, 3]. Computational methods are necessary to extend the treatment of the problem beyond a single dendritic tip and to address more complex solidification conditions.

2.6 Scale Range and Numerical Models

The process of solidification involves various scales, ranging from the atomic level, where solid-liquid adhesion kinetics are investigated, to the macroscopic level, where heat and solute transport are studied over meter-length scales. This multiscale nature makes solidification a challenging and complex problem.

As researchers historically developed theoretical models that focus on specific scales, the need to quantitatively verify them led to the use of computational simulations. Fig. 2.11 illustrates the different scales of solidification, along with their corresponding computational models. In this thesis, the focus is on the *dendritic needle network* (DNN) model, which provides an intermediate level of detail between dendritic morphology and the generalization of the grain boundary.

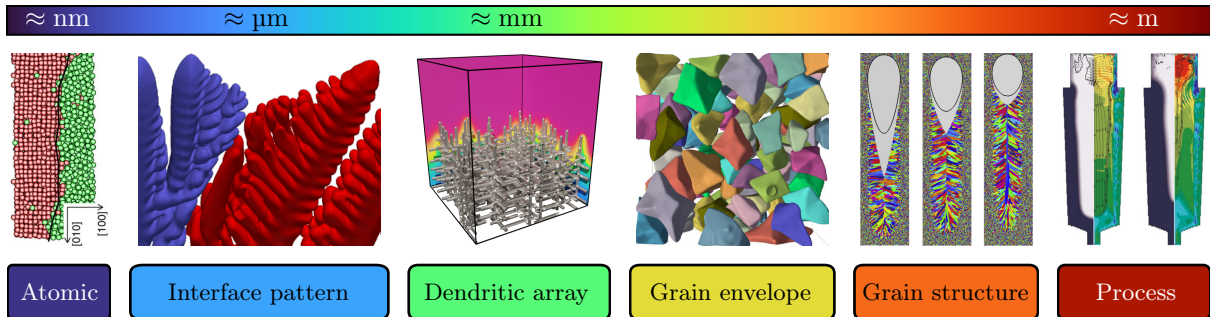


Figure 2.11: Different scales of solidification, along with their corresponding computational models. The studied effects covers from the study of the bonding process between solid and liquid at the atomic level (on the left side) to the examination of the flow of heat and solute in casting processes at the meter scale (on the right side). Reproduced with permission of T. Isensee from [57], with references from left to right: [54], [109], [57], [96], [21], [24].

In the following subsections, we briefly discuss some of the most commonly-used numerical computational models, including molecular dynamics (MD) simulations, the phase-field (PF) method, the grain envelope model (GEM), and cellular automaton (CA) models. Moreover the aim of this section is not to perform an in-depth analysis using equations and parameter analysis, but rather to provide a qualitative understanding of the primary characteristics of each model. Additionally, this section aims to provide the reader with a comprehensive list of references for further reading and research.

2.6.1 Atomistic Models

In solidification processes, the way atoms arrange themselves at the interface between solid and liquid states affects how patterns form. This is because the interface energy γ required to create an interface affects how new solid particles form, i.e., in the primary nucleation in undercooled melts. The anisotropy of γ and the anisotropy in the interface stiffness $\gamma + d^2\gamma/d\theta^2$, where θ is the angle between the [100] direction and the interface normal, also play a crucial role in pattern formation, especially in dendritic solidification.

It is worth noting that other coarse-grained models, such as phase-field and DNN, also require precise values for fundamental properties. However, obtaining these properties directly through measurement is a significant challenge as it has only been achieved for a few materials. Therefore, molecular dynamics simulations have become increasingly vital in advancing our understanding of these properties over the past few decades.

In [53, 54] researchers have developed a method using molecular dynamics simulations to calculate the anisotropy (directional dependence) of the interfacial stiffness. This property can be related to the spectrum of interfacial fluctuations and helps scientists understand how the interface behaves during solidification. An example of such simulation is shown in Fig. 2.12.

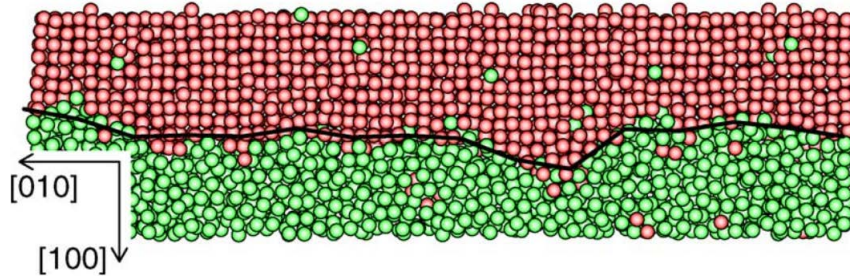


Figure 2.12: Computer simulation of pure Ni where we can see a boundary between the solid and liquid parts that is always moving due to changes in temperature. The boundary is marked by a solid line and is determined by a measure called φ which tells us how much the atoms are deviating from their ideal positions [54].

2.6.2 Phase-Field

The phase-field method, initially defined by Langer in 1978 and published in 1986-87 [70, 71], is a mathematical tool utilized to solve problems that involve moving interfaces, such as solidification and phase separation in binary alloys. Developed later in a quantitative framework by Karma in 2001 [63], the method is based on an order parameter, or phase field φ , that describes a diffuse interface that changes smoothly over a width W from one phase to another. This is in contrast to other models and allows for the implicit description of the solid-liquid interface.

It is crucial to note that the degree of order in a thermodynamic system undergoing a phase transformation is essential, as these transformations often involve symmetry breaking. The interface thickness, denoted by W , is nearly an order of magnitude smaller than the tip radius but significantly larger than the actual interface width. This feature, as shown in Figure 2.13, allows for practical three-dimensional calculations in relatively small supersaturations.

The phase-field method has been proven to accurately compute solid-liquid interfaces in dendritic growth. For a detailed overview of the current state-of-the-art of the phase-field method, readers should refer to the reviews by Karma [62], Ode et al. [80], or Chen [20].

2.6.3 Grain Envelope

The grain envelope approach is a modeling technique used to describe dendritic growth in solidification. The original idea was from Rappaz and Thévoz [88] and later expanded upon by Beckermann and others [78, 114, 115]. The approach involves treating the liquid phase as two different “phases” and using volume-averaged balances on multi-phase domains to model solidification at the macroscopic scale. The grain envelope is described by a virtual smooth surface that connects longer growing tips and the underlying dendritic structure is not resolved. Solute transport is described by volume-averaged equations and the solute flux rejected into the liquid by the dendritic tips determines the growth of the envelope. The solute concentration ahead of the tip is used to calculate the tip growth velocity, and a phase-field method is used to track the sharp interface. The model has been shown to predict envelope shapes, growth velocities, and internal solid fractions of single grains growing into an infinite melt quantitatively,

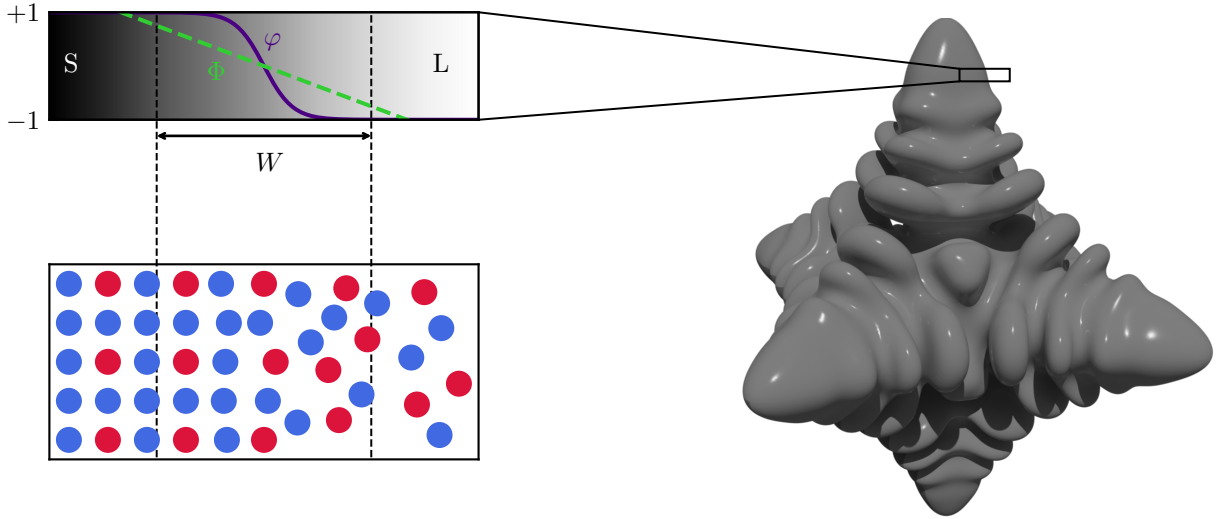


Figure 2.13: Diffuse interface and equiaxed dendrite formed in a supersaturated binary alloy using the phase-field approach. The image (left) shows an order parameter φ that smoothly changes over the interface thickness W , along with its preconditioned field ϕ , and the corresponding discrete atomic structure. The right side illustrates the predicted three-dimensional shape of an equiaxed dendrite [57].

as well as transient interactions between several grains. As an example, Fig. 2.14 displays three simulation snapshots using the grain envelope model, which involved randomly distributing and orienting grains in an isothermal cubic enclosure with an initial supersaturation fixed at $\Omega_0 = 0.05$. Note that different distributions and initial densities or supersaturation conditions can be used for simulations.



Figure 2.14: Simulation snapshots of randomly distributed and oriented grains growing isothermally in a cubic enclosure with an initial supersaturation of $\Omega_0 = 0.05$ [96].

2.6.4 Cellular Automaton

The Cellular Automaton is a model of dendritic growth introduced by Rappaz and Gandin [87, 40] that combines finite difference or finite element computations with a probabilistic physically based cellular automaton model for nucleation and growth kinetics. The model divides space uniformly into cells with a set of variables such as temperature and solid or liquid flags assigned to each cell. A transition rule is defined to describe the evolution of a cell in one time step. Grains are modeled with polygons or polyhedrons, and nucleation site distributions and densities are calibrated from experiments. Various methods, such as finite element [21, 40, 87], finite differences [116], and the Lattice-Boltzmann methods [59] have been coupled with Cellular Automaton (CA) models for modeling fluid flow and macroscopic dynamics. An instance of a

2. DENDRITIC GROWTH

cellular automaton simulation setup is illustrated in Fig. 2.15, wherein a square lattice of uniform cells divides the volume. The cell state index is zero when the cell is liquid and becomes an integer when it solidifies, which is associated with the randomly generated crystallographic orientation of the grain.

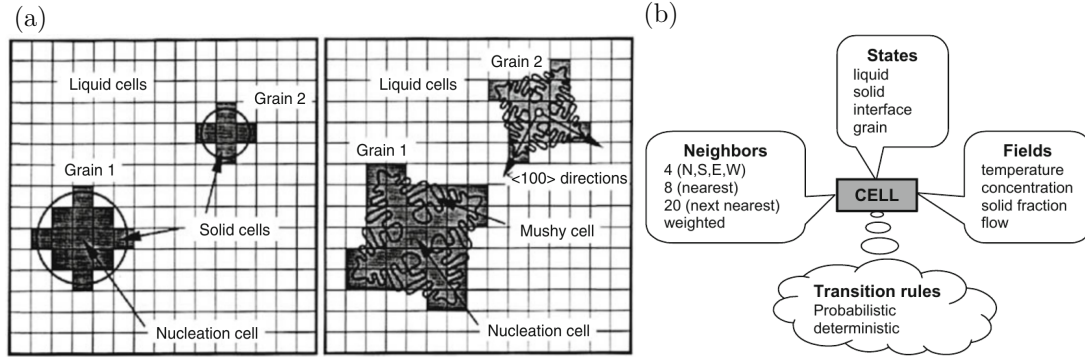


Figure 2.15: (a) Computational space of a 2D cellular automaton for dendrite envelope grain growth. (b) Example of a cellular automaton setup, where each cell is assigned information regarding its state and calculated fields, and a neighborhood configuration is selected to include cells that can directly influence each other [98].

3 DENDRITIC NEEDLE NETWORK MODEL

This chapter provides an introduction to the dendritic needle network (DNN) model. In the first section (Section 3.1), an overview of the earlier stages of DNN and subsequent developments are presented. The second section (Section 3.2) describes the current model utilized in this research. Finally, the third section (Section 3.3) briefly introduces the numerical implementation of the two-dimensional model explained in previous sections. While the explanations provided in this chapter are concise, they should be sufficient for readers to grasp the model's basic equations and concepts. In the pursuit of a more comprehensive and in-depth understanding of the model, please refer to the following sources: [61, 105, 106, 104, 55].

3.1 DNN history

The model was initially proposed by Alain Karma in 2001 [61], where he provided an intuitive explanation of the underlying physics and the governing equations of dendritic growth. In addition, the paper aimed to present his theoretical understanding of the problem, including the growth of branches which he referred to as “needle crystals” in section four. This simplification was significant but had not been rigorously justified until then. Although Karma’s model was fully introduced in two dimensions, some open questions remained when attempting to extend it to 3D.

It was not until 2013 that Damien Tourret and Karma published a validated 2D version of the model for isothermal and directional solidification [105]. They presented the model for simulating quantitatively the solidification of dendritic alloys. The novelty of the model was that it reliably bridged the gap between phase-field simulations on the scale of dendrite tip radius and cellular-automaton simulations on the several orders of magnitude larger scale of an entire dendritic grain. Indeed, comparisons of the DNN model with analytical solutions for phase-field simulations demonstrated that DNN simulations were much faster (by approximately four orders of magnitude) while still maintaining reasonable accuracy. They demonstrated in applied simulations (see FIG. 3.1 in next page) that the DNN model was capable of predicting the evolution of dendritic structures during solidification processes.

In 2016, they published an extension of the model to three dimensions [107]. They first presented an extended formulation of the 2D DNN model where needles had a finite thickness and parabolic tips (a comparison between both approaches is shown in Fig. 3.2). They subsequently developed a 3D DNN model based on this thick-needle formulation for both isothermal and directional solidification. Besides validating the model, they successfully characterized the competitive growth of well-developed secondary branches in 3D systems on the scale of diffusion length. In the field of directional solidification, they compared the 3D DNN simulation of an Al-7wt% Si alloy to observed microstructures from microgravity experiments conducted aboard the International Space Station. The simulation results agreed well with the predictions of selected microstructural features, such as dendrite arm spacings.

In 2015 and 2016, after consolidating the model in two and three dimensions, for isothermal and directional conditions and limited to diffusion transport, further results were compared to experimental measurements in Al-Cu [108], Al-Si [110], Al-Ni [100], and more recently in Al-Ge [6] alloys.

In 2019, Tourret et al. [104] introduced a method to include liquid melt flow in 2D isothermal simulations while also allowing for the simulation of dendritic branches with arbitrary orientation

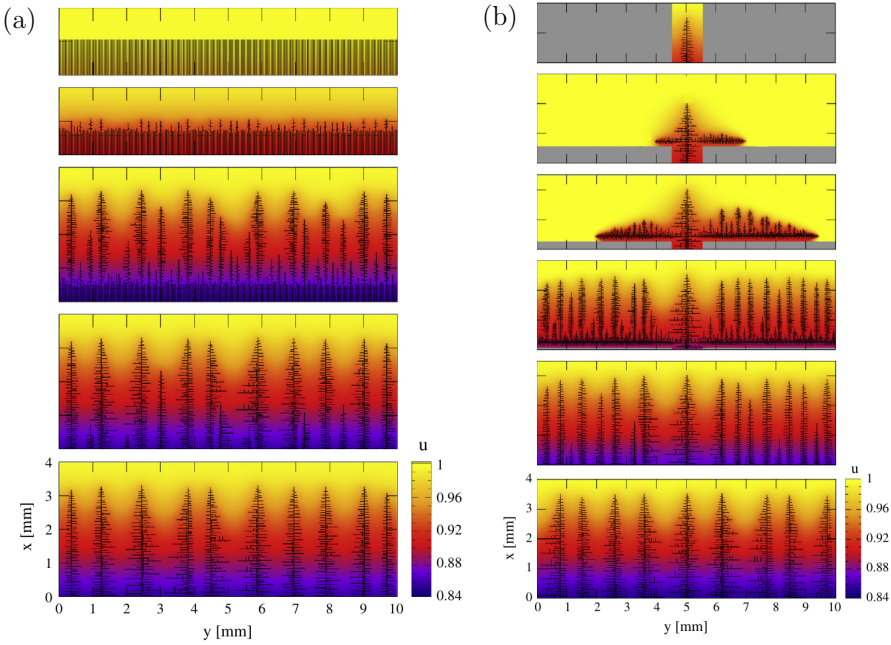


Figure 3.1: DNN 2D simulations using the first implemented version of Tourret and Karma’s model with infinitely sharp needles [105]. The simulations were conducted to model two scenarios related to the directional solidification of an Al-7 wt.% Si alloy. Scenario (a) depicts the destabilization of a planar front initially located at the liquidus temperature, while scenario (b) represents the directional solidification growth with a change in cross-section.

independent of the numerical grid. This enabled the modeling of polycrystalline microstructures that account for different grain orientations, as well as the growth of hexagonal crystal structures. Then, in the following years, Isensee and Tourret proposed two extensions to the model: the 3D version with fluid flow limited to isothermal conditions [55] and the 2D version with fluid flow for directional solidification [56]. Regarding this last implementation, which is described in-depth in section 3.2, the authors were able to use the DNN model to successfully reproduce the oscillatory growth behavior recently observed via in-situ X-ray imaging during the directional solidification of the nickel-based superalloy CMSX-4 [90]. For a better understanding of the fundamental history of the Dendritic Needle Network model, please refer to Table 3.1 for an easy-to-follow overview.

Topic	Authors	Year
First idea (lecture notes)	Karma [61]	2001
First numerical implementation in 2D with “thin” needles	Tourret and Karma [105, 106]	2013
Extension to 3D and parabolic needles	Tourret and Karma [107]	2016
Extension to fluid flow for isothermal conditions in 2D	Tourret et al. [104]	2019
Extension to fluid flow for isothermal conditions in 3D	Isensee and Tourret [55]	2020
Extension to fluid flow for directional conditions in 2D	Isensee and Tourret [56]	2022

Table 3.1: Main stages in DNN history from early 2000’s to the present.

Additional advancements have been made, such as the examination of transition from columnar to equiaxed growth (referred to as CET) [42, 19], as well as the integration of cellular automata (CA) with tip growth kinetics inspired by DNN [36], which is known as the parabolic thick needle (PTN) model. Most recently, the work undertaken within this thesis has also led to the publication of a peer-reviewed article focusing on the mechanisms of the buoyancy-induced

oscillatory growth instability in directional solidification [4].

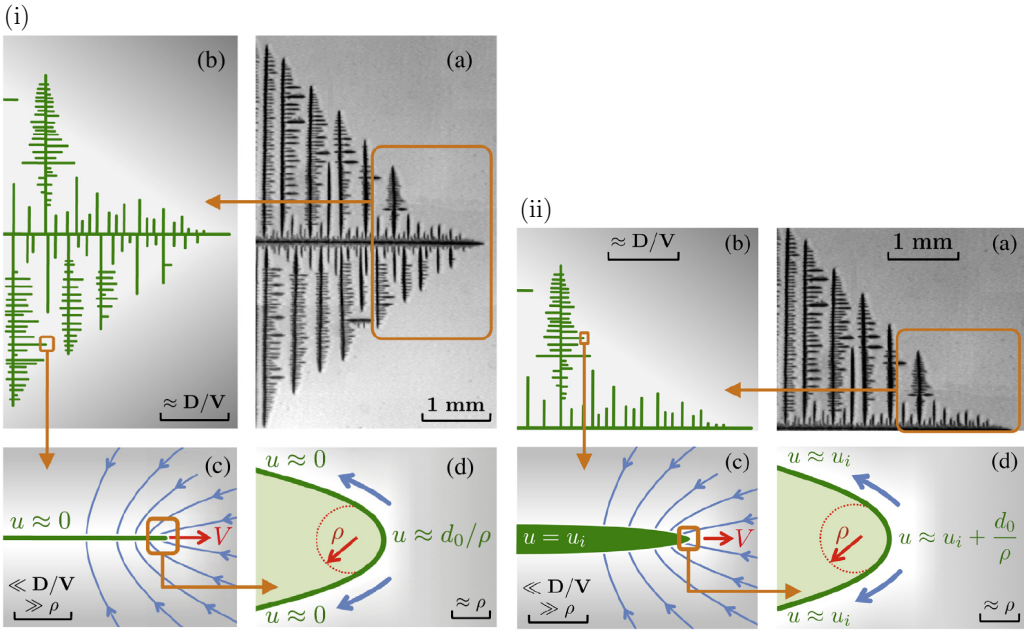


Figure 3.2: The dendritic needle network approach using both infinitely sharp (i) and finite thickness (ii) implementations. In this model, a dendritic grain, such as an ammonium-bromide crystal shown in subfigure (a) from Ref. [26], is represented as a hierarchical network of needle-like branches that interact through a long-range diffusion field, illustrated in subfigure (b). The instantaneous tip radius $\rho(t)$ and velocity $V(t)$ of each needle are determined by two conditions at different length scales. At an intermediate scale larger than the tip radius ρ but smaller than the diffusion length D/V , a solute conservation condition is applied, which is indicated by the $\gg \rho$ and $\ll D/V$ scale bar labels in subfigure (c). At the scale of the tip radius ρ , a solvability condition is established, as shown in subfigure (d).

3.2 Directional Formulation

The 2D DNN model presented in the following directional formulation corresponds to the implementation carried out by Isensee and Tourret in 2022 [56], and the description in the model follows the same as that in [4] and [57].

The dendritic needle network (DNN) model alleviates the burden of explicitly tracking the morphologically complex solid-liquid interface by representing growing crystals as hierarchical networks of thin parabolic-shaped branches [107, 104, 56]. Fig. 3.3 (see next page) illustrates the concept of the DNN and its essential variable definitions at the different length scales. With a tip radius much smaller than the diffusion length $l_D = D/V$, conservation equations are derived on different length scales: (i) solute transport via diffusion or advection-diffusion (see Fig. 3.3b), (ii) mass conservation on an intermediate scale between the tip radius R and the diffusion length, providing the product RV^2 in the two-dimensional formulation and the product RV in the three-dimensional formulation (see Fig. 3.3c), and (iii) a microscopic solvability condition at the scale of R (see Fig. 3.3d), giving the product R^2V . Thus, the combination of those conditions enables to obtain the instantaneous growth terms $R(t)$ and $V(t)$. Within the liquid phase, the advection of solute through fluid flow is considered and incorporated into the model by direct computation of the Navier-Stokes equations.

The temperature field, $T(\mathbf{x}, t)$, is usually imposed as a boundary condition throughout the domain, and the evolution of the solute concentration field, $c(\mathbf{x}, t)$, is solved considering either diffusive [107] or convective [104, 56] conditions in the liquid phase, while the concentration along

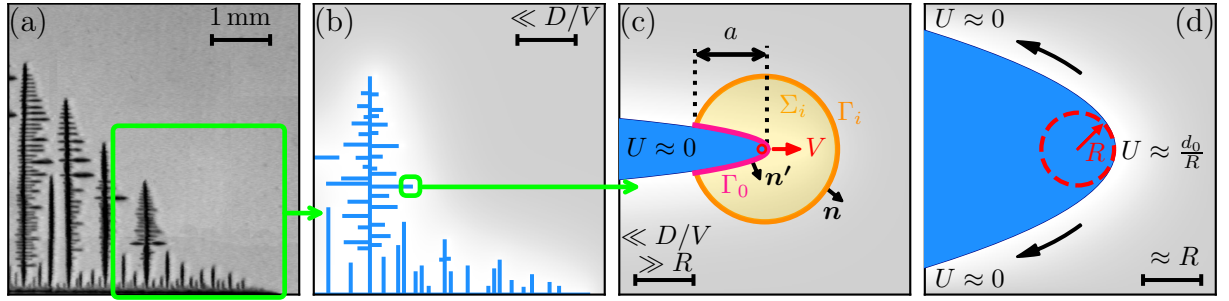


Figure 3.3: The Dendritic Needle Network (DNN) model is conceptually illustrated in this study. The model is based on a dendritic network structure of an ammonium-bromide crystal in a supersaturated aqueous solution, as shown in (a) [26]. In the DNN model, the structure is represented by a network of thin parabolic needles that interact through a long-range diffusion field, as depicted in (b). The liquid equilibrium concentration is imposed on the needles. The instantaneous tip velocities $V(t)$ and radii $R(t)$ of each needle are obtained by a combination of conditions on two different length scales. At the intermediate scale, a solute conservation condition near the tip fixes the product $RV \propto \mathcal{F}$ (3D) or $RV^2 \propto \mathcal{F}^2$ (2D), where the flux intensity factor (FIF) \mathcal{F} is computed by integrating the flux towards the dendrite tip over the contour Γ_0 as shown in (c). At the small scale of the tip radius R , the microscopic solvability condition fixes the product R^2V in (d). Sourced from [57].

the solid-liquid interface, i.e., along the needle network, is set at the equilibrium concentration at the local temperature.

As illustrated in Fig. 2.2 (from the previous chapter), we consider a dilute binary alloy with constant liquidus slope, $m < 0$, and solute partition coefficient, $0 < k < 1$, and introduce the reduced (dimensionless) concentration field,

$$U \equiv \frac{c_l^0 - c}{(1 - k)c_l^0} \quad (3.1)$$

where c_l^0 is the liquid equilibrium concentration at the reference (i.e., solidus) temperature, T_0 (see Eq. 2.8). Directional solidification conditions are represented via the frozen temperature approximation $T = T_0 + G(x - V_p t)$, where G is the strength of the temperature gradient and V_p is the pulling (or isotherm) velocity, both imposed along the x direction. Neglecting curvature and kinetic undercooling contributions, i.e., at a scale much larger than the tip radius R , the equilibrium dimensionless concentration, U_i , along the solid-liquid interface is expressed as

$$U_i \approx \frac{x - V_p t}{l_T} \in [0, 1], \quad (3.2)$$

which varies between 0 at the solidus temperature and 1 at the liquidus temperature, such that $U_i(x \rightarrow +\infty) = 1$ with

$$l_T = \frac{|m|(1 - k)c_l^0}{G} = \frac{T_l - T_s}{G} \quad (3.3)$$

the thermal length separating liquidus and solidus temperatures (the freezing range of the alloy).

The liquid velocity field, \mathbf{v} , is calculated using Navier-Stokes equations

$$\rho [\partial_t \mathbf{v} + (\mathbf{v} \cdot \nabla) \mathbf{v}] = \mathbf{F} - \nabla p + \eta \nabla^2 \mathbf{v}, \quad (3.4)$$

$$\nabla \cdot \mathbf{v} = 0, \quad (3.5)$$

where ρ is the fluid density, p its pressure, η its viscosity and \mathbf{F} corresponds to external forces. The liquid is assumed incompressible and a null velocity is imposed along the solid-liquid interface, i.e., along the needles.

Buoyant forces are included using the Boussinesq approximation, considering only solute-dependent terms

$$\mathbf{F} = \rho_\infty^l \mathbf{g} [1 - \beta_c(c - c_\infty)], \quad (3.6)$$

where $\beta_c \equiv -(\partial\rho/\partial c|_{c=c_\infty})/\rho_\infty^l$ is a solutal expansion coefficient, with ρ_∞^l the fluid density at the alloy nominal concentration c_∞ and \mathbf{g} is the gravity acceleration. The transport of solute in the liquid with fluid velocity \mathbf{v} is thus described by the advection-diffusion equation, with diffusion coefficient D ,

$$\partial_t U + \nabla \cdot (\mathbf{v} U) = D \nabla^2 U. \quad (3.7)$$

The instantaneous tip radius, $R(t)$, and velocity, $V(t)$, of each needle-like branch is computed using the microscopic solvability condition

$$R^2 V = \frac{2Dd_0}{[1 - (1 - k)U_t]\sigma}, \quad (3.8)$$

where $d_0 = \Gamma / [|m|(1 - k)c_l^0]$ is the capillary length at T_0 with Γ the interface Gibbs-Thomson coefficient, $U_t = (x_t - V_p t)/l_T$ is the equilibrium concentration at the tip position, x_t , and σ is the tip selection parameter [69, 67], combined with a solute conservation statement in the vicinity of the parabolic tip

$$RV^2 = 2D^2 \mathcal{F}^2 / \{ [1 - (1 - k)U_t]^2 d_0 \}, \quad (3.9)$$

where the flux intensity factor (FIF) is defined as follows

$$\mathcal{F} \equiv \int_{\Gamma_0} (\partial_n U) dS / (4\sqrt{a/d_0}) \quad (3.10)$$

that measures the incoming flux and can be calculated, thanks to the divergence theorem, along any contour Γ_i (instead of directly on the solid-liquid interface along Γ_0) as

$$4\mathcal{F}\sqrt{a/d_0} = \int_{\Gamma_i} (\partial_n U) dS + \frac{V}{D} \int_{\Sigma_i} (\partial_x U) dA, \quad (3.11)$$

with $\partial_n U$ the outward normal solute gradient, Σ_i the surface enclosed between Γ_0 and Γ_i , and a the distance between the tip and the intersection of the integration contour with the parabolic tip (i.e., the location where Γ_0 and Γ_i meet) [107, 104]. See Fig. 3.5 in next chapter for a deeper explanation of FIF integration.

Equation (3.8) comes from the classical microscopic solvability theory [71], while Eq. 3.9 comes from a simple statement of solute mass conservation in the vicinity of the dendrite tip [107].

3.2.1 Scaled Equations

It is necessary to reformulate here the aforementioned Navier-Stokes equations (3.4) and (3.5) along with the advection-diffusion equation (3.7) to fully understand the discretized form of these equations that will be presented in the next section.

For scaling equations we will use the steady state tip radius R_s and the steady state tip velocity V_s , which, following from Eq. (3.8), are given by

$$R_s = \sqrt{\frac{2Dd_0^*}{\sigma V_s}} = \frac{d_0^*}{\sigma Pe} = \frac{1}{[1 - (1 - k)U_s] \sigma Pe} \frac{d_0}{\sigma Pe}, \quad (3.12)$$

$$V_s = \frac{2DPe^2\sigma}{d_0^*} = [1 - (1 - k)U_s] \frac{2DPe^2\sigma}{d_0} = V_p, \quad (3.13)$$

where U_s refers to the steady-state concentrations, d_0^* to the capillary length at the tip (obtained from d_0 as $d_0^* = d_0/[1 - (1 - k)U_t]$) and Pe to the Péclet number $\text{Pe} = R_s V_s / (2D)$.

Finally the scaled equations read

$$\nabla \cdot \mathbf{v} = 0, \quad (3.14)$$

$$\partial_\tau \mathbf{v} + (\mathbf{v} \cdot \nabla) \mathbf{v} = \frac{1}{\text{Re}^*} \nabla^2 \mathbf{v} - \nabla \psi + \tilde{\mathbf{F}}, \quad (3.15)$$

$$\partial_\tau U + \nabla \cdot (\mathbf{v} U) = \tilde{D} \nabla^2 U, \quad (3.16)$$

with the scaled time $\tau = tV_s/R_s$, the scaled pressure $\psi = p/(\rho_0 V_s^2)$ and the Reynolds number $\text{Re}^* = R_s V_s / \nu$. The scaled external force $\tilde{\mathbf{F}} = \mathbf{F} R_s / (V_s^2 \rho_0)$ can be written as

$$\tilde{\mathbf{F}} = \tilde{\mathbf{g}} [1 + (\lambda_T + \lambda_c) U], \quad (3.17)$$

with the scaled gravity $\tilde{\mathbf{g}} = \mathbf{g} R_s / V_s^2$, and the scaled thermal and solutal expansion coefficients $\lambda_T = m(k-1)c_0^l \beta_T$ and $\lambda_c = (1-k)c_0^l \beta_c$, respectively.

3.3 Numerical Implementation

This section follows the structure and descriptions from [57]. It will provide a very simple and illustrative explanation of the numerical implementation based on [48] of the DNN model. For a more exhaustive description with fully developed equations please refer to [57] and [104].

3.3.1 Discretization of Space and Equations

The model is solved similarly as in Refs. [104, 56], i.e., using a mostly explicit finite difference scheme on a staggered grid (a two-dimensional schematic of this grid can be seen in Fig. 3.4), an upwind discretization scheme for convective terms, a projection method for the resolution of the Navier-Stokes equations [22], and an iterative successive over-relaxation (SOR) method [37, 117] for the incompressibility condition.

As an example, the discretized form of the scaled Navier-Stokes equations (3.14)-(3.15) and the scaled advection-diffusion equation (3.16) in two dimensions are included, where the velocity components are expressed as $\mathbf{v} = [u \ v]^T$. Note how in Fig. 3.4 these components will refer to the grid.

$$\partial_x u + \partial_y v = 0 \quad (3.18)$$

$$\partial_\tau u + \partial_x u^2 + \partial_y(uv) = \frac{1}{\text{Re}^*} (\partial_x^2 u + \partial_y^2 u) - \partial_x \psi + \tilde{F}_x \quad (3.19)$$

$$\partial_\tau v + \partial_x(vu) + \partial_y v^2 = \frac{1}{\text{Re}^*} (\partial_x^2 v + \partial_y^2 v) - \partial_y \psi + \tilde{F}_y \quad (3.20)$$

$$\partial_\tau U + \partial_x(uU) + \partial_y(vU) = \tilde{D} (\partial_x^2 U + \partial_y^2 U). \quad (3.21)$$

For the sake of clarity the remaining equations (in three and two dimensions) are omitted. These include, among others, the following:

- Solute Concentration

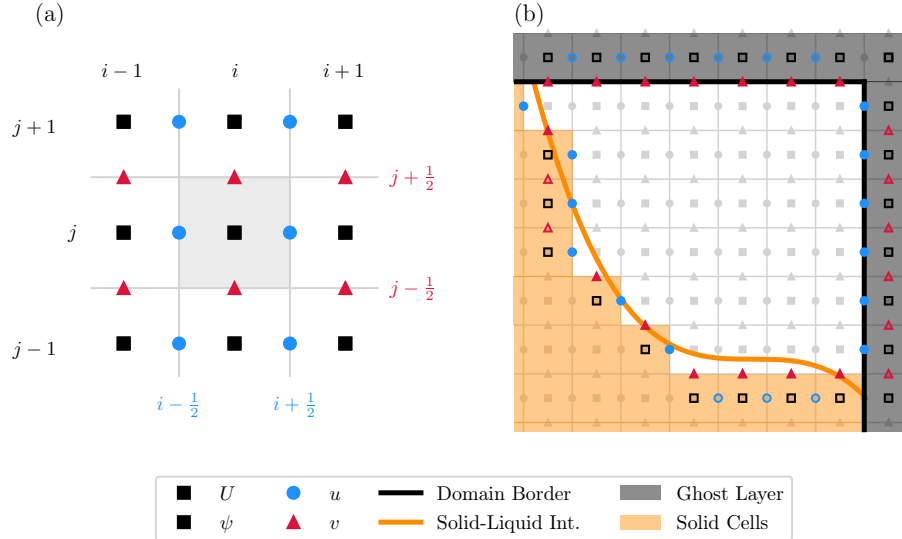


Figure 3.4: (a) The two-dimensional finite difference grid depicted in a staggered arrangement. The indices i and j represent the positions on the grid, with the velocity components u and v shifted by $h/2$ from the center in their respective directions. The diffusive field U and the pressure field ψ are positioned at the center. (b) The curved solid-liquid interface (solid orange line) is approximated by discrete steps on the staggered grid. The discretized solid region is highlighted in orange, while the dark areas represent the ghost layer at the domain boundary, which is utilized for applying boundary conditions. The colored markers represent the components determined by the boundary conditions, with full markers indicating direct determination and open markers indicating indirect determination. Sourced from: [57].

- The discrete approximation of the advection-diffusion equation (3.21) with explicit time stepping.
- The discretized form of the diffusive term of Eq. (3.16).
- Momentum Conservation
 - The discretized form of diffusive terms of Eq. (3.19)-(3.20).
- Pressure Poisson
 - The discretized form of Eq. (3.15) without the pressure contribution.
 - The Poisson equation.
- Boundary and Periodic Conditions

3.3.2 Growth of Dendritic Branches

Equations (3.8) and (3.9) govern the growth of each individual branch. Also, the flux intensity factor (FIF) defined in Eq. (3.10), is calculated using the divergence theorem, resulting in Eq. (3.11).

In the context of Fig. 3.3c, the calculation of $\mathcal{F}(t)$ involves the utilization of a circular integration contour denoted as Γ_i . This contour has a radius r_i and is centered at the tip of the dendrite. The distance a behind the tip can be determined by the expression $\sqrt{R^2 + r_i^2} - R$. To approximate the circular contour and the dendritic needle using discrete steps, a numerical approach as depicted in Fig. 3.5a (see next page) is employed. Grid cells falling within the solid region represented by a parabola (or paraboloid of revolution in 3D) (indicated by the blue

solid region) are considered as solid, while grid cells within the continuous integration contour (illustrated by the orange dashed circle) are chosen for numerical integration (highlighted in orange shading).

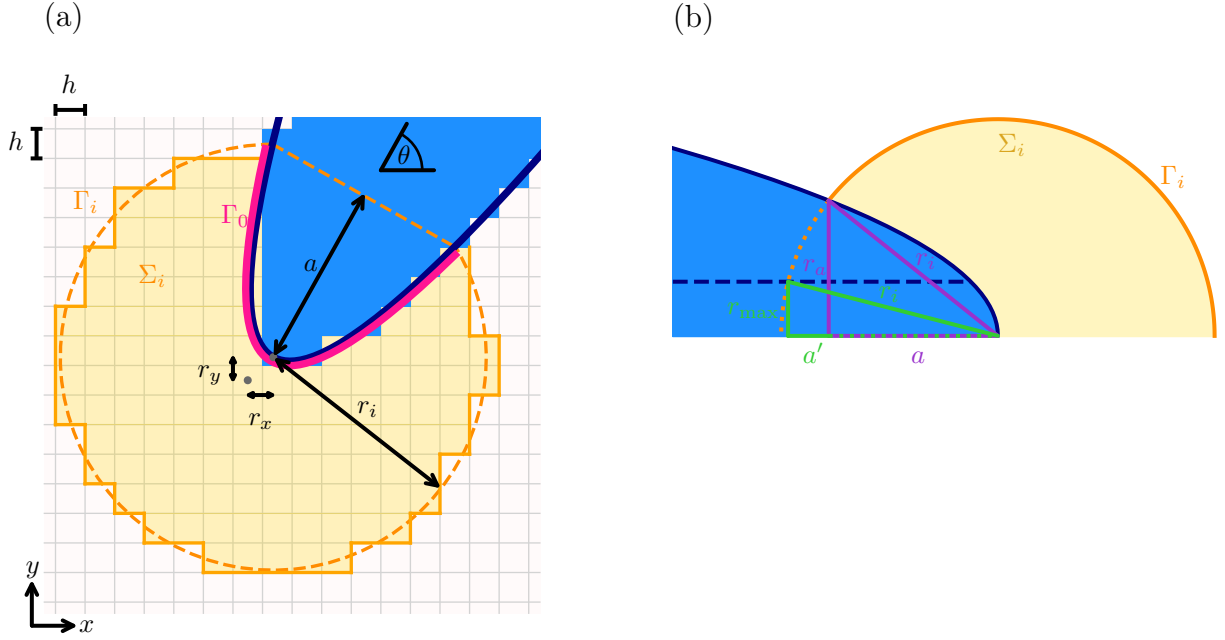


Figure 3.5: (a) The tip region of a two-dimensional parabolic dendrite, represented by the blue solid region, is inclined at an angle θ on a finite difference grid with a grid spacing of h . The parabolic dendrite, along with the integration contour Γ_0 (depicted as a solid pink line) and the circular FIF integration contour Γ_i (shown as a dotted orange line) with a radius r_i , are approximated step-wise along the grid. The FIF integration contour Γ_i encompasses the integration surface Σ_i and intersects the dendrite at a distance a behind the tip. (b) The figure also includes a representation of a parabolic needle (depicted in blue) with its full shape shown as a solid line and its truncated shape as a dashed line. The FIF integration contour (highlighted in orange) is associated with the needle. In the case of a full parabola, the value of a is calculated as $a = -R + \sqrt{R^2 + r_i^2}$, where R represents the instantaneous tip radius. However, if the parabola is truncated to a maximum half-width of r_{max} , the value of a' is calculated as $\sqrt{r_i^2 - r_{max}^2}$. To clarify, both values can be computed, and the larger one is selected for the FIF computation. Figure sourced from: [57].

3.3.3 Parallelization

To enhance computational speed through parallelization, the code is implemented in C-based Compute Unified Device Architecture (CUDA) platform from NVIDIA® [79], which utilizes (single) Graphics Processing Units (GPUs) for acceleration.

3.3.4 Moving Domain

DNN simulations are highly valuable for predicting microstructural length scales, specifically the primary dendritic arm spacing. These simulations capture the elimination of dendrites and the formation of side-branches, which play a significant role in determining the spacing and competition during grain growth. These selection mechanisms primarily occur in the vicinity of the solidification front. However, within the mushy zone deeper into the material, the DNN model loses its relevance as it doesn't track the evolution of solid fraction. To focus our simulations on the region close to the solidification front, we employ a moving frame approach, allowing us to

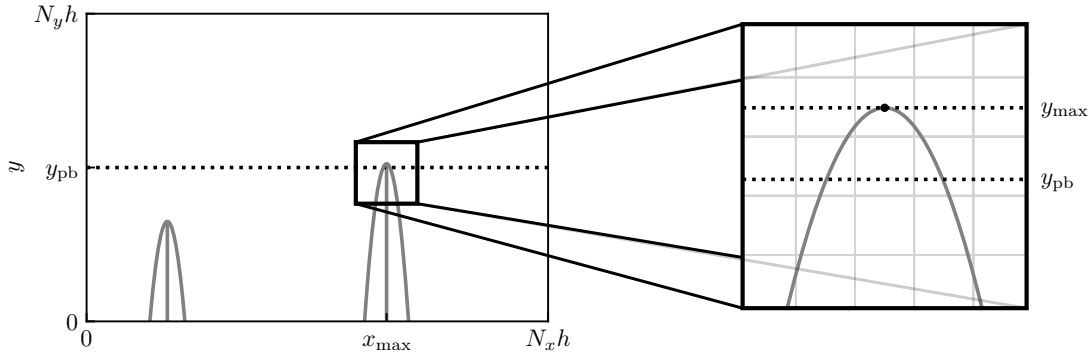


Figure 3.6: Schematic representation of a moving simulation domain in the DNN model for directional solidification. The positions x_{max} and y_{max} , which correspond to the maximum x and y positions of all needles, are continuously monitored. If the value of y_{max} exceeds a predefined position y_{pb} , an adjustment is made. This adjustment involves shifting all field values and the positions of the needles in the y direction to ensure that y_{max} remains less than or equal to y_{pb} . Sourced from [57].

simulate a larger time range. This procedure is illustrated in Fig. 3.6.

To ensure that the simulation domain moves with the most advanced needle tip, the model tracks and compares the tip positions (x and y , representing growth direction) with the desired position (y_{pb}) within the domain. If the position of the most advanced needle tip (y_{max}) exceeds y_{pb} , it shifts all field values in the y -direction by $\Delta j = \text{floor}(y_{max} - y_{pb})$. This means that in the x and y directions respectively, it updates the values of arrays (such as concentration, pressure, and velocities).

4 SIMULATIONS

This chapter deals with the computational basis of the research done. Section 4.1 states the motivations that drive this research and summarizes the current state of the field in relation to previous studies addressing oscillatory growth phenomena in directional solidification. Secondly, section 4.2 reformulates the questions underlying this research, providing a detailed exposition of the relevant physical aspects guiding our simulation methodology. Then, section 4.3 summarizes the main simulations performed and how they have been carried out on a large scale. Finally, in sections 4.4 and 4.5 the techniques used for data visualization and features extraction are explained.

It's worth noting that, sections 4.1 and 4.2 are directly derived from the ongoing research documented in our publication [4].

4.1 Motivations

Directional solidification (DS) is critical to manufacture a range of high-value components. A prominent example is that of single-crystal Ni-based superalloy turbine blades for aeronautical applications [86]. They are arguably among the most advanced manmade structural metallic components, capable to withstand extreme thermal, mechanical, and chemical conditions all at once. However, various defects may emerge, such as segregated channels and freckles [25, 93, 52, 85], which may lead to a significant amount of manufactured parts being discarded. Therefore, a better fundamental understanding of the conditions leading to stable and homogeneous DS is critical to the production of the next-generation of directionally solidified components.

Recently, experiments using X-ray *in situ* radiography revealed the existence of oscillatory instabilities during DS of Ni-based superalloy CMSX-4 [90]. Over the years, a range of oscillatory instabilities during DS had been previously investigated, e.g., related to growth in a narrow channel [64], coordinated “breathing modes” in cellular array growth [41, 8, 108], sidebranching at high primary spacing [31], or banding instabilities in rapid solidification [66, 60]. However, while all of these naturally occur within a purely diffusive thermo-solutal transport regime, the oscillations observed in CMSX-4 stem from gravity-induced buoyancy [90], making them more challenging to investigate. The effect of buoyant convection on dendritic growth and microstructure heterogeneities has been acknowledged for decades [74, 29, 58, 11, 94]. However, due to the various scales to be incorporated together in the problem, quantitative modeling of dendritic growth in presence of fluid flow remains computationally demanding [92, 91].

Using a multiscale dendritic needle network (DNN) approach [105, 107], extended to include fluid flow in the liquid phase [104, 56], Isensee and Tourret recently managed to reproduce the growth oscillations observed in CMSX-4 [56]. Beyond reproducing experimental observations — e.g., the transition from oscillatory to damped oscillations when increasing the cooling rate (or equivalent pulling velocity V_p) — our simulations highlighted the importance of the primary dendritic spacing Λ on the occurrence (at high Λ) or inhibition (at low Λ) of these oscillations, and the fact that sustained oscillations seemed to occur when the average fluid velocity \bar{V} was close to V_p .

Computational simulations of this oscillatory behavior naturally open the way for a deeper and systematic exploration of the conditions of occurrence and characteristics of oscillations as a function of alloy parameters and processing conditions. Extending Isensee and Tourret previous study [56], here we perform a mapping of this buoyancy-induced oscillatory behavior as

a function of primary spacing and pulling velocity by performing a large number of simulations. An underlying objective is also to uncover whether this phenomenon is generalizable to other alloys, provided the appropriate combination of temperature gradient G , pulling velocity V_p , and primary spacing Λ . Hence, we focus on a different alloy with relatively well-known phase diagram and thermophysical properties, namely Al-4at.%Cu.

4.2 Theoretical background

In Ref. [56], our simulations aimed at approaching specific experimental conditions of CMSX-4 directional solidification [90]. In contrast, here, an underlying objective is to investigate whether the oscillatory behavior may be general to any arbitrary alloy, provided the appropriate set of (G, V_p, Λ) conditions. Therefore, we consider a different alloy, namely a binary Al-4at.%Cu, with relatively well known parameters [56, 99], but so far no report of such oscillatory growth behavior. Specifically, we use alloy parameters as in Refs [56] (Section 3.1 therein) and [99], i.e., $c_\infty = 4.0$ at.%, $D = 3 \times 10^{-9}$ m²/s, $k = 0.14$, $m = 1.6$ K/at.%, $\nu = \eta/\rho = 5.7 \times 10^{-7}$ m²/s, $\Gamma = 2.4 \times 10^{-7}$ Km, $\beta_c = -10^{-2}$ /at.%, and $\sigma \approx 0.153$ (corresponding to an interfacial excess free energy anisotropy $\epsilon = 0.02$). In an Al-Cu alloy (unlike in CMSX-4), buoyant currents and plumes are caused by the rejection of the heavier element (Cu). Therefore, while the growth direction is kept as $x+$ and represented upwards for consistency with Ref. [56], gravity forces also have a $x+$ direction (i.e. pointing upwards in figures below). We fix the temperature gradient at $G = 10$ K/mm, and explore velocities from $V_p = 40$ to 100 μm/s within a range of primary dendrite arm spacing Λ from about 90 to 350 μm.

The radius of integration of the flux intensity factor is set to $r_i/R_s = 4$ and the truncation radius of needles far behind the tip to $r_{\max}/R_s = 5$, with R_s the theoretical steady state tip radius in the diffusive regime [107, 56]. For each velocity V_p , the grid spacing is chosen between $\Delta x/R_s = 0.7$ and 1.24, ensuring that the diffusion length included a sufficient number of grid points — namely with $D/V_p/\Delta x$ ranging from 6 ($V_p = 100$ μm/s) to 16 ($V_p = 40$ μm/s). Other numerical parameters are similar to those listed in Ref. [56] (Table 1 therein, with $K_{\Delta t} = 0.5$).

With these parameters, the simulations are similar in nature to those presented and discussed in Ref. [56] (Sections 3.1 and 4 therein). Within a domain of height H (x -direction) and width W (y -direction), we set an array of N evenly spaced primary needles at the bottom of the domain growing in the $x+$ direction and with their tips initially aligned in x along the liquidus temperature location. Boundary conditions (BCs) are periodic laterally (in the y direction) for all fields. No-flux ($\partial U/\partial x = 0$) and free-slip ($v_x = 0$) conditions are applied along the top and bottom boundaries (in the x direction). The simulations use a moving frame in the x -direction, such that the most advanced needle tip in x remains at a fixed location — namely at a distance between 30% and 65% of the domain height from the bottom boundary.

The domain size in x , i.e., its height H , is chosen long enough for BCs to have negligible effect on the flow pattern — typically adjusted by trial-and-error, ensuring that the liquid length is always greater than $5D/V_p$ and the solid length greater than $8D/V_p$. The domain size in y is set to either 630 or 1470 inner grid points, for convenience (both numbers are divisible by a broad range of integer needle number N , as required to impose periodic arrays) and performance (accounting for the two extra points used to impose periodic BCs, both 632 and 1472 are divisible by 8, thus allowing nearly optimal GPU block sizes). Each simulation is initialized with between 7 and 30 needle-like primary dendrites, in order to probe different values of primary spacing Λ . The array growth was simulated for a duration of between 90 (high V_p) and 120 (low V_p) seconds, so as to obtain enough oscillation periods to analyze, when relevant.

In the scope of this research we have conducted over 150 simulations, but only 44 of them pertain to the peer-reviewed article published from the work undertaken within this thesis. Later on this chapter the rest of simulations will be discussed. Main parameters of the 44 simulations mentioned above are summarized in Table 4.1. Each simulation is performed using a single GPU (Nvidia RTX3090, in most cases) and each required at most 92 h to complete (wall time).

Velocity V_p (μm)	Grid spacing		Height $H/\Delta x$	Number of needles, N		PDAS range Λ (μm)
	$\Delta x/R_s$	Δx (μm)		$W/\Delta x = 630$	$W/\Delta x = 1470$	
40	1.24	7.06	638	14, 18, 21, 30	-	(148, 318)
50	1.10	5.56	638	10, 14, 15, 18, 21, 30	-	(117, 350)
60	1.00	4.59	510	9, 10, 14, 15, 18, 21, 30	-	(96, 321)
70	0.94	3.98	510	7, 9, 10, 14, 15, 18, 21	-	(119, 358)
80	0.90	3.54	398, 510	7, 9, 10, 14, 15, 18, 21	-	(106, 319)
90	0.80	2.96	398, 510	7, 9, 10, 14, 15, 18	14	(103, 310)
100	0.70	2.44	398	7, 9, 10, 14, 18	14	(86, 257)

Table 4.1: Simulation parameters for the mapping of V_p and Λ .

4.3 Launching

The research conducted for this thesis utilizes the DNN model described in Chapter 3, along with the numerical implementation presented in Section 3.3, which is based on the work of Isensee and Tourret in 2022 [56]. The C-based CUDA implementation of the model is employed as a “black box” with *input files* used to manipulate simulation parameters. Due to the inherent complexities of physical simulations, careful specification of numerous variables and constants, such as alloy composition, domain size, initial conditions, and simulation behavior, is essential.

Firstly, this section provides an overview of the specific hardware and computational facilities employed in the research. Subsequently, we delve into the methodology used to initiate simulations, conducting a detailed analysis of its scalability to handle a significant volume of simulations. Lastly, an overview of the total number of conducted simulations will be presented.

4.3.1 Cluster, GPUs and Slurm

The research was made possible through utilization of the IMDEA Materials GPU cluster, a high-performance computing system equipped with over 600 Intel Xeon CPU cores and NVIDIA GPU acceleration, resulting in a formidable computational power of 90 Tflops¹.

The IMDEA Materials GPU cluster consists of five nodes, each named after the Hulk, Ironman, Thor, Asterix, and Obelix. While all nodes except Hulk have four GPUs, Hulk stands out with eight GPUs. With a combined total of 24 GPUs, this incredible computing power has been instrumental in facilitating the scale of our research. Table 4.2 presents a concise summary of the GPUs per node and their respective NVIDIA models. The cluster’s formidable computational capabilities have made significant contributions to the success of our study.

¹ *Teraflops*: a unit of measurement for a computer’s speed, denoting approximately one thousand billion (= 1,000,000,000,000), or one trillion, operations (= processes) per second [102].

Node	Number of GPUs	Model/Version
Hulk	8	GeForce RTX 2080 Ti
Ironman	4	GeForce RTX 3090
Thor	4	GeForce RTX 3090
Asterix	4	Titan Xp
Obelix	4	GeForce GTX 1080 Ti

Table 4.2: Summary of GPUs per node and available models in the IMDEA Materials GPU cluster

The IT group at IMDEA played a vital role in supporting and maintaining the cluster, effectively utilizing the open-source workload manager and job scheduler, *Slurm*. Designed for high-performance computing clusters, *Slurm* stands for “Simple Linux Utility for Resource Management”. This powerful tool efficiently allocates and schedules tasks, widely favored by research and academic institutions for managing computing resources and jobs on large-scale clusters. Slurm has been fundamental in the progress of our research. Given the nature of our experimentation, involving the scanning of a solution space through numerous simulations, Slurm has streamlined the process by seamlessly launching over 150 simulations one after the other, while carefully managing resources and ensuring smooth execution.

4.3.2 Workflow

In Slurm, launching simulations is a straightforward process for C-based CUDA code. The steps involved are:

1. Compile the model script using the CUDA compiler, known as `nvcc`.
2. Create a launch file, usually with a `.sh` extension, where you specify the job name, node, and GPU to be used. An example of such a file can be found in Listing 4.1.
3. Launch the simulation using Slurm with the `sbatch` command, as follows:
`sbatch launch_file.sh`.

```

1 #!/bin/bash
2
3 #----- Specify:: NAME for the GPU job -----
4 #SBATCH --job-name="v4_N14_D3_k0.1_AlCu"
5 #SBATCH --output="v4_N14_D3_k0.1_AlCu.out"
6
7 #----- Specify:: NODE and GPU to run the job on -----
8 #SBATCH --partition="Obelix"
9 #SBATCH --nodelist="obelix"
10 #SBATCH --gres=gpu:1
11
12 module load gcc/8.2.0
13 module load cuda10.1/toolkit/10.1.243
14 /home/josep.barbera/Codes/DNNFF2DDIR_OBELIX_ELIM v4_N14_D3_k0.1_AlCu 0

```

Listing 4.1: In this example, we present a Slurm manager launch file. Lines 1 to 10 contain directives for Slurm, where we specify the job name, output file name, the targeted node, and the GPU for our simulation. Lines 12 and 13 specify the required compiler versions for C and CUDA, respectively. Finally, line 14 executes the compiled code with the corresponding input file.

4. SIMULATIONS

Upon completion of the aforementioned steps, the compiled code DNNFF2DDIR_OBELIX_ELIM will be provided with the associated input file, v4_N14_D3_k0.1_A1Cu. Leveraging the directives outlined in lines 3 to 10 of Listing 4.1, the Slurm manager will initiate the simulation on the OBELIX node's GPU number 1, if available. In case the GPU is occupied, the simulation will be placed in a queue, awaiting its turn.

Once the workflow was established, it became evident that manually launching over 200 simulations would be a time-consuming and energy-intensive task, potentially slowing down the progress of our investigation. To address this challenge, we automated the process using a Python script within the framework of *Jupyter Notebooks*. In this section, we present the primary function of this implementation.

Initially, a *matrix* of simulations is created using a list of *tuples*. Subsequently, the script organizes and generates the necessary input and launching files as required. All these operations are performed locally on a desktop computer, and the resulting files are then uploaded to the server using the `scp` command. In the code listing shown in Listing 4.2, we emphasize the central role of the `create_input_case()` function, which is accompanied by essential supporting functions. For access to the complete source code, kindly refer to our repository at: <https://github.com/jbarciv/DNN-FittyPlot>.

```
1 # ([order, server , vel, Nneedles, gpus,      dx,   Nx,   Ny,  time, end name])
2 # For no end_name type 0, Nneedles could be an array
3 simulations =
4 ([1,   'asterix', 10,  [9],      [0],      0.7,  630, 398, 120, 0],
5  [2,   'asterix', 9,   [15],     [1],      0.8,  630, 398, 120, 0],
6  [4,   'asterix', 8,   [15],     [2],      0.9,  630, 398, 120, 0],
7  [5,   'asterix', 7,   [15, 7],  [3, 0],   0.94, 630, 510, 120, 0],
8  [6,   'asterix', 6,   [18, 14], [1, 2],   1.0,  630, 510, 120, 0],
9  [7,   'asterix', 5,   [18, 14], [3, 0],   1.1,  630, 638, 120, 0])
10
11 # Sorting list of tuples according to a key
12 def first(n):
13     return n[0]
14
15 # Function to sort the tuple
16 def sort(list_of_tuples):
17     return sorted(list_of_tuples, key = first)
18
19 # Dictionary for executables
20 executables = {
21     'thor': 'DNNFF2DDIR_IRON_THOR_ELIM',
22     'ironman': 'DNNFF2DDIR_IRON_THOR_ELIM',
23     'obelix': 'DNNFF2DDIR_OBELIX_ELIM',
24     'asterix': 'DNNFF2DDIR_ASTERIX_ELIM',
25     'hulk': 'DNNFF2DDIR_HULK_ELIM'
26 }
27
28 # Main function for creating run files and input files for all the matrix
29 # At the end it creates the global run file.
30 def create_input_case(project_name, simulations_path, project_path,
31                      executables_path, sims, k, D):
32     sorted_sims = sort(sims)
33     out_list = []
34     j = 0
35     for i in range(len(sorted_sims)):
36         server = sorted_sims[i][1]
37         V = sorted_sims[i][2]
38         v = V
39         V = V * 1.e-5
40         Needle_array = sorted_sims[i][3]
```

```

41     GPUs = sorted_sims[i][4]
42     dx = sorted_sims[i][5]
43     Nx = sorted_sims[i][6]
44     Ny = sorted_sims[i][7]
45     t_end = sorted_sims[i][8]
46     end_name = sorted_sims[i][9]
47     j = 0
48     for needle in Needle_array:
49         GPU = GPUs[j]
50         d = str(D)
51         if isinstance(end_name, str):
52             jobname = 'v' + str(v) + '_N' + str(needle) + '_Nx' + str(Nx)
53             + '_dx' + str(dx) + '_D' + d[:d.rfind("e")]
54             + '_k' + str(k) + '_AlCu_' + end_name
55         else:
56             jobname = 'v' + str(v) + '_N' + str(needle) + '_Nx' + str(Nx)
57             + '_dx' + str(dx) + '_D' + d[:d.rfind("e")]
58             + '_k' + str(k) + '_AlCu'
59
60         create_run_file(project_path, server, GPU, executables[server],
61                         executables_path, jobname)
62         create_input_file(project_path, V, needle, dx, Nx, Ny, t_end, D,
63                           k, jobname)
64         out_list.append('sbatch ' + jobname + '.sh')
65         j = j + 1
66
67     create_global_run_file(simulations_path, project_path, out_list,
68                           project_name)
69
70 # Calling the main function: all the process starts
71 create_input_case(project_name, simulations_path, project_path,
72                   executables_path, simulations, k, D)

```

Listing 4.2: Python script demonstrating the automation of simulation setup, with a specific emphasis on the central function `create_input_case()`. This script is designed to efficiently manage numerous simulations. In our research, we initiated four groups, each comprising about 50 simulations.

4.3.3 Planning

For a good performance in the execution of over 150 simulations, meticulous planning was essential. Since our research focuses on the study of oscillatory growth in solidification of alloys, we have chosen a well-known binary alloy, Al-4at.%Cu, but which has not been reported to exhibit such oscillatory patterns so far. After comprehensively studying it, we altered two key physical parameters, i.e., the diffusion coefficient (D) and the partition coefficient (k), to observe their impact on oscillation.

For this purpose, we organized the simulations into four groups, Table 4.3 helps to visualize them. The first simulation (A) focuses on the binary alloy under study. The second and third simulations (B and C) maintain the initial diffusivity but vary the partition coefficient, ranging from 0.14 to 0.2 and then down to 0.1. Finally, the fourth (D) involves modifying the diffusivity while keeping the partition coefficient constant, i.e., dividing D from 3 to 1.5.

Furthermore, within each group, we explore two fundamental parameters: the pulling velocity (V_p) and the needle density (N_i), representing the desired number of needles within the study domain, and inversely proportional to the primary spacing between dendritic trunks. The selection of these parameters has been conducted meticulously to ensure the realism and scientific rigor of our simulations. For instance, the number of needles has a significant impact on

		k		
		0.1	0.14	0.2
D (m ² /s)	3 × 10 ⁻⁹	C	A	B
	1.5 × 10 ⁻⁹	-	D	-

Table 4.3: Overview of our four simulation groups, each exploring unique aspects of the binary alloy's behavior. These letters will be used later in following chapters.

symmetry. Therefore, while maintaining the domain size, we have established specific density ranges, including 14, 18, 21, and 30, but these choices may vary depending on the domain size. The following paragraphs provide a summary of the four simulation groups (A, B, C, and D), detailing the specific number and values of their parameters.

4.3.3.1 [A, B, C]: Simulations with $D = 3 \times 10^{-9}$ m²/s, for $k = 0.1, 0.14$ and 0.2

For consistency with Refs. [56, 4] and previously stated by section 4.2, the growth direction is kept as $x+$ and represented upwards (contrary to Fig. 3.6) as shown in Fig. 4.1.

Within a domain defined by a height (H) in the x -direction and a width (W) in the y -direction, we arrange an array of evenly spaced primary needles at the bottom of the domain, denoted by N_i . Specifically, for H_x values of 398, 510, or 638, with $W_y = 630$ grid points, this configuration gives rise to 7 distinct velocities (V_i) and 4 potential needle densities (N_i). Consequently, this results in a total of 28 simulations, as outlined in Table 4.4.

It's worth noting that all 28 simulations will be conducted three times, each iteration corresponding to one of the three possible values of k , while maintaining constant the density $D = 1.5 \times 10^{-9}$ m²/s.

$V(\mu\text{m}/\text{s})$	V_4	V_5	V_6	V_7	V_8	V_9	V_{10}
	40	50	60	70	80	90	100
N_1	14	10	9	9	7	7	7
N_2	18	15	15	14	14	10	10
N_3	21	21	21	18	18	14	14
N_4	30	30	30	21	21	18	18
Duration (s)	120	120	100	100	90	90	90
H_x	638	638	510	510	398	398	398

Table 4.4: Simulation parameters for scanning each of the first three group simulations, i.e., A, B, and C. These 28 simulations will be done three times each one for the three possible values of k while keeping the real density to $D = 1.5 \times 10^{-9}$ m²/s. All these should be done with $W_y = 630$ for the width of the domain. Beyond these initially planned simulations, it eventually became requisite to conduct further experiments. The complete count of simulations for map A is elaborated in Table 4.1.

It is also necessary to launch four more simulations with $H_x = 398$ and $W_y = 1470$ as shown in Table 4.5. All with the same parameters as above for V_9 or V_{10} , except for values of N .

After defining the scanning parameters, the next step involves scheduling simulations across the four GPUs of a node.

- GPU#0: $V_4N_1, V_6N_3, V_8N_1, V_{10}N_3, V_5N_4, V_7N_2, V_9N_4$, Large 1

	Large 1	Large 2	Large 3	Large 4
$V(\mu\text{m}/\text{s})$	90	90	100	100
N	14	18	14	10

Table 4.5: Simulation parameters for scanning each of the first three group simulations, i.e., A, B, and C. But now with $W_y = 1470$ for the dimensions of the domain.

- GPU#1: $V_4N_2, V_6N_4, V_8N_2, V_{10}N_4, V_5N_1, V_7N_3, V_9N_1$, Large 2
- GPU#2: $V_4N_3, V_6N_1, V_8N_3, V_{10}N_1, V_5N_2, V_7N_4, V_9N_2$, Large 3
- GPU#3: $V_4N_4, V_6N_2, V_8N_4, V_{10}N_2, V_5N_3, V_7N_1, V_9N_3$, Large 4

4.3.3.2 [D]: Simulations with $D = 1.5 \times 10^{-9} \text{ m}^2/\text{s}$, for $k = 0.14$

Due to the reduced diffusivity (D) in the fourth map (D), some adjustments are needed compared to the previous ones. With dimensions $H_x = 510$ and $W_y = 630$, and a duration of 120 s, a total of 12 simulations are conducted, as detailed in Table 4.6.

	V_4	V_5	V_6	V_7	V_8	V_9
$V(\mu\text{m}/\text{s})$	40	50	60	70	80	90
N_1	10	10	9	7	7	14
N_2	14	18	10	14	-	-
N_3	15	-	-	18	-	-

Table 4.6: Simulation parameters for scanning the last simulation group (D). With $W_y = 630$ for the dimensions of the domain.

For $N_x = 630, N_y = 510$, one additional simulation with $V = 50 \mu\text{m}/\text{s}, N = 10$, and a reduced $\Delta x/R_s = 0.8^2$ is needed. The simulation is labeled $V_5N_1^{\Delta x}$.

Finally for $H_x = 510$ and $W_y = 1470$ there are 6 more simulations with the parameters shown in Table 4.7.

	Large 7	Large 8	Large 9	Large 10
$V(\mu\text{m}/\text{s})$	70	80	90	100
N_1	14	14	10	10
N_2	-	-	14	14

Table 4.7: Simulation parameters for scanning the last simulation group (D). With $W_y = 1470$ for the size of the domain.

Again, after defining the scanning parameters, the scheduling across the four GPUs of a node proceeds as follows:

- GPU#0: $V_4N_1, V_7N_3, V_5N_1, V_6N_2$, Large₉ N_2
- GPU#1: $V_4N_2, V_7N_1, V_5N_2, V_6N_1$, Large₁₀ N_2
- GPU#2: V_4N_3, V_7N_2, V_8N_1 , Large₈ N_1 , Large₁₀ N_1
- GPU#3: $V_9N_1, V_5N_1^{\Delta x}$, Large₇ N_1 , Large₉ N_1

² Δx refers to the spacing of the finite difference grid while R_s to the dendrite tip radius at steady state. The quotient of both allows us to set the maximum difference between them.

4.4 Data Output

Visualizing the results of our simulations is a crucial step in the process. The current implementation provides three types of output files, each serving specific purposes based on its extension:

- **.txt**: This format is employed for summarizing all the simulation parameters. Typically, there is just one file of this type.
- **.dat**: Here, we save the physical values of each needle at every time step throughout the simulation. Each needle's data is stored in a separate file.
- **.vtk**: These files are designed for visualizing the simulation output. Generally, there are two types: one for displaying velocity data and another for showing concentration fields. Users have the flexibility to choose the number of files they wish to generate.

For instance, in Fig. 4.1, we illustrate how to load and visualize .vtk files directly using the software tool *ParaView*. This visualization provides a clear representation of the evolving directional and dendritic solidification of our binary alloys. For other types of visualization, such as plotting data from .dat files, post-processing is required, as we will discuss in the next section.

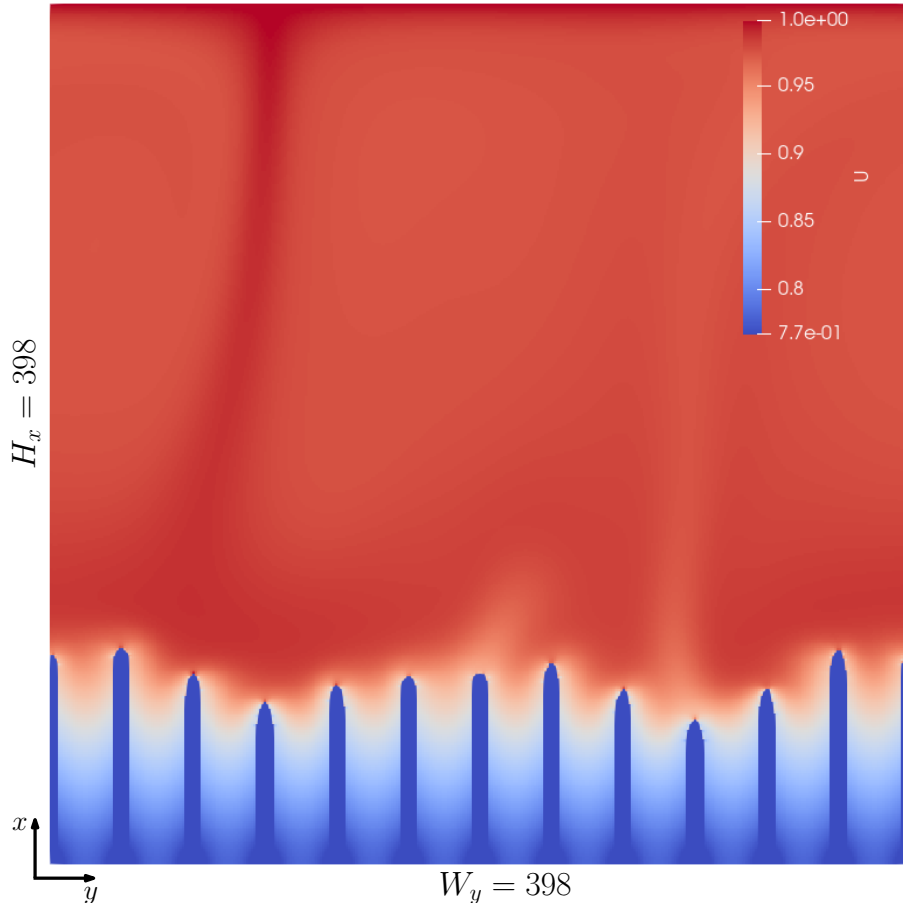


Figure 4.1: Screenshot from *ParaView*, visualizing simulation results. Here, we observe the representation of the concentration field (U) for the selected binary alloy (Al-4at.%Cu) in a simulation with twelve needles ($N = 12$) and the next physical values: $k = 0.14$, $V_p = 40 \mu\text{m/s}$, $H_x = 398$ and $W_y = 398$ grid points. *ParaView*'s versatility enables a comprehensive analysis of complex physical processes, offering valuable insights into our simulations.

4.5 Data Post-Processing

To visualize the simulation output, we utilized `.vtk` files in conjunction with *ParaView*, as demonstrated in the previous section. Now, we will employ the `.dat` files to directly plot and analyze the simulation behavior from a different perspective. Direct data analysis involves a post-processing phase that encompasses data plotting, averaging, filtering, and eventually employing data fitting algorithms.

In this section, we will begin by explaining the significant variables to plot and elucidate how to achieve this through data filtering or averaging in specific scenarios. Subsequently, we will delve into the fitting process, which aids in extracting valuable features from data.

4.5.1 Plotting and Averaging

In our research, the most crucial data stems from the dendrite growth rate, represented as the velocity evolution, denoted as $V(t)$, at the tip of each needle in every simulation. Consequently, our initial task is to access this data. Through a custom Python script, we can locate the respective `.dat` file for each needle within the simulation, resulting in one plot per needle. These files consist of 40 columns and approximately ten thousand lines, corresponding to each iteration in the calculations. The number of lines depends on the simulation's duration. For instance, approximately 10,000 iterations translate to roughly 13 hours of wall time.

Once we have obtained the data, which comprises two substantial vectors (one representing simulation time in seconds, and the other depicting the growth rate in $\mu\text{m}/\text{s}$), we proceed to create plots. For this purpose, we employ libraries like *Matplotlib* in Python. The initial post-processing step involves smoothing the raw $V(t)$ data due to its susceptibility to numerical oscillations as the needle progresses through the grid [104]. This smoothing can be achieved by applying a moving average to the time derivative of the needle length, prior to, for instance, fitting. Please see Fig. 4.3 where it is displayed both the raw and smoothed $V(t)$ data.

As the plotting code tends to be lengthy and repetitive, it is not included here. We encourage you to visit our GitHub repository at <https://github.com/jbarciv/DNN-FittyPlot> for comprehensive details, especially concerning the creation of the plot grids for each simulation and the dynamic selection of optimal y -bounds in the plots. Nonetheless, in Listing 4.3, you can observe the process of averaging raw $V(t)$ data to achieve smoothing.

```

1 test_data = np.loadtxt(needle_file_path, skiprows = 1)
2 ##### calculate velocity as derivative of the length (smoother) #####
3 n = 20 #smoothness
4 data_time_collapsed = test_data[:, TIME]
5 data_length_collapsed = test_data[:, LENGTH]
6 data_dLdt = np.gradient(data_length_collapsed, data_time_collapsed)
7 #####
```

Listing 4.3: These lines of code are extracted from the custom Python script used for generating figures. These few lines accomplish the task of smoothing raw data. The process involves calculating the growth rate from the time derivative of the needle length, but it's done for every ' n ' values. By adjusting this ' n ' value, we can control the level of smoothness of the process, what we call a moving average. The 'TIME' and 'LENGTH' parameters indicate the column numbers where the relevant data is located.

4.5.2 Fitting

In order to classify the simulated growth behaviors and extract oscillation characteristics, apart from plotting and smoothing, individual needle velocities, $V(t)$, should be fitted to either of these two functions

$$v_1(t) = V_0 - A \cos [2\pi(t - t_0)f] \exp(-t/\tau), \quad (4.1)$$

$$v_2(t) = V_0 - A \{(1 - S) \cos [2\pi(t - t_0)f] + 2S |\cos [\pi(t - t_0)f]| - S\}, \quad (4.2)$$

via the following fitting parameters: mid-range velocity V_0 , time origin t_0 , oscillation amplitude A , oscillation frequency f , and either a characteristic damping time τ (Eq. (4.1)) or a “spikiness” factor S (Eq. (4.2)). The latter, bounded to $0 \leq S \leq 1$, allows fitting signals showing burst-like “spiky” maxima, yet with stable-frequency oscillations. As illustrated in Figure 4.2, $S = 0$ leads to a regular cosine function and $S = 1$ to a spiky cosine-like function of similar amplitude and frequency. (Note that, when $S > 0$, the mid-range velocity V_0 differs from the average velocity V_p)

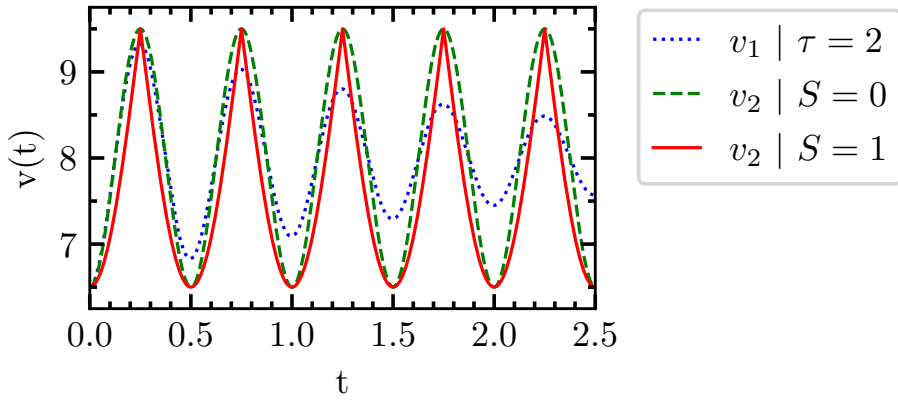


Figure 4.2: Illustration of functions $v_1(t)$ and $v_2(t)$ for $V_0 = 8.0$, $A = 1.5$, $f = 2.0$, $t_0 = 0.0$ and different values of τ (Eq. (4.1)) or S (Eq. (4.2)).

We chose to fit to both functions and select the best fit out of the two for convenience, after noticing that damped oscillations typically had smooth (non-spiky) behaviors while sustained oscillations had a range of behaviors from smooth to spiky. For each needle, the fitting was performed using a custom Python script that dynamically scans different fitting ranges and selects the one leading to the best fit, i.e., the highest coefficient of determination r^2 , while ensuring that the range included a minimum of 5 oscillation periods (when relevant) or at least 20 seconds.

Growth velocities $V(t)$ leading to a poor fit to both functions, namely if $r^2 < 0.8$, were classified as *noisy* (rather than rigorously *non-oscillatory* since their behavior was usually closer to noisy oscillations than to erratic bursts as reported in Ref. [56]). When $r^2 \geq 0.8$, behaviors were classified as *damped* if the fit was better with Eq. (4.1) than Eq. (4.2), or *sustained* otherwise. (Damped oscillations were all quite straightforward to identify from visual inspection of $V(t)$.)

To provide a comprehensive demonstration of the fitting process, refer to Fig. 4.3 (next page). This figure illustrates velocity data for needle number 1, derived from a simulation characterized by specific parameters: $N = 7$, $k = 0.14$, $D = 3 \times 10^{-9} \text{ m}^2/\text{s}$, and $V_p = 90, \mu\text{m/s}$, on a grid with dimensions $H_x = 398$ and $W_y = 630$. (Henceforth, we will employ a condensed notation for simulations, e.g., V9_N7_D3_k0.14_AlCu_630x398). The figure incorporates a legend box that presents the fitted values. This observed behavior signifies a *oscillatory pattern*, discernible

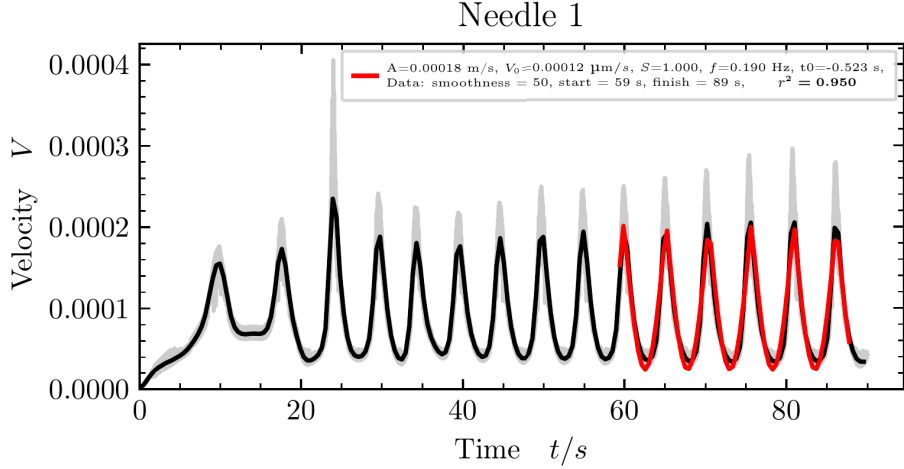


Figure 4.3: Sustained oscillation behavior for simulation V9_N7_D3_k0.14_AlCu_630x398. Plot of dendrite growth rate versus simulation time along with the fitting. In gray, the raw data is represented, in black, the smoothed data, and in red, the fitting curve. This velocity corresponds to needle number 1. The label inside displays the fitted values: $V_0 = 0.00012 \mu\text{m}/\text{s}$, $A = 0.00018 \text{ m/s}$, $f = 0.190 \text{ Hz}$, $t_0 = -0.523 \text{ s}$, and $S = 1.0$, with a coefficient of determination of $r^2 = 0.950$.

through visual inspection and confirmed by its alignment with the fitting equation (Eq.(4.2)), demonstrating significant accuracy ($r^2 \geq 0.8$).

In Fig.4.4, we present another fitting example, but now showcasing a *damping pattern* described by Eq.(4.1). The velocity data, labeled as $V(t)$, corresponds to needle number 3 and originates from the simulation V9_N10_D3_k0.14_AlCu_630x398. The plot includes the fitted values for the red function, demonstrating a robust coefficient of determination of $r^2 = 0.986$.

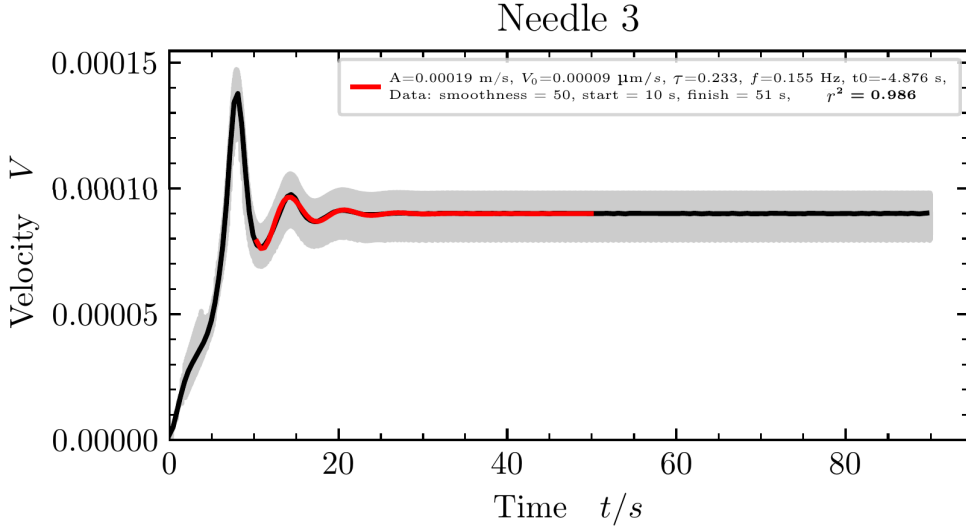


Figure 4.4: Damped oscillatory behavior for simulation V9_N10_D3_k0.14_AlCu_630x398. Plot of dendrite growth rate versus simulation time along with the fitting. This velocity corresponds to needle number 3. The label inside displays the following fitted values: $V_0 = 0.00009 \mu\text{m}/\text{s}$, $A = 0.00019 \text{ m/s}$, $f = 0.155 \text{ Hz}$, $t_0 = -4.876 \text{ s}$, and $\tau = 0.223$, with a coefficient of determination of $r^2 = 0.986$.

The initial guess for the frequency f , prior to its fitting, was based on a preliminary estimate via fast Fourier transform of the $V(t)$ signal. The *SciPy* Python library played a vital role in this fitting process, you can find the code responsible for this post-processing task in Listing 4.4 and in the GitHub repository previously mentioned. This code efficiently computes the FFT of the velocity signal, determines the number of data points, initializes a frequency array, calculates the

4. SIMULATIONS

Power Spectral Density (PSD) to reveal the signal's frequency content, and identifies significant peaks above a threshold.

```

1 def the_FFT(dt, total_time, velocity, time):
2
3     # Get the number of data points
4     n = len(time)
5     # Create a time array and initialize a frequency array
6     t = np.arange(0, total_time, dt)
7     freq = (1 / (dt * n)) * np.arange(n)
8     # Define an array for frequency indices (excluding 0 and Nyquist frequency)
9     L = np.arange(1, np.floor(n / 2), dtype='int')
10    # Compute the FFT and calculate the Power Spectral Density (PSD)
11    X = fft(velocity)
12    PSD = X * np.conj(X) / n
13    # Set a threshold for identifying peaks in the PSD
14    PSD_threshold = np.max(np.real(PSD[L])) * (1 / 5)
15    # Find peaks in the PSD above the threshold
16    peaks, _ = find_peaks(np.real(PSD[L]), height=PSD_threshold)
17    # Find the position of the maximum value in the PSD
18    PSD_max = np.max(PSD[L])
19    PSD_max_pos = np.where(PSD == PSD_max)[0][0]
20    # Select the frequency corresponding to the maximum PSD value
21    freq_max = freq[PSD_max_pos]
22    # Check a condition and possibly select the second peak as the frequency
23    → maximum
24    if True and (peaks[1] < 100):
25        PSD_max_pos = peaks[1] + 1
26        freq_max = freq[PSD_max_pos]
27    else:
28        PSD_max_pos = peaks[0] + 1
29        freq_max = freq[PSD_max_pos]
30
31    return freq, PSD, L, freq_max, PSD_max_pos

```

Listing 4.4: Implemented Fast Fourier Transform (FFT) function used for analyzing the velocity signal, denoted as $V(t)$, to identify its initial frequency component. This frequency estimation serves as the initial guess for the subsequent fitting process.

Additionally, Figure 4.5 presents a visual representation of the Fourier spectrum, providing a comprehensive view of the signal's frequency distribution. This graphical representation aids in the understanding of the dominant frequency component. These FFT results are central to our data analysis, playing a fundamental role in the subsequent fitting and analysis processes.

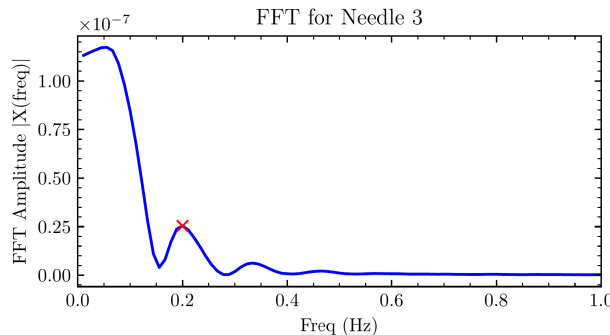


Figure 4.5: Fourier spectrum and the identified frequency component for $V(t)$ from Fig. 4.4 obtained through the fast Fourier transform (FFT), as discussed in Listing 4.4. This analysis aids in estimating the initial frequency (f) for further processing (fitting).

5 RESULTS

This chapter compiles the results obtained from the conducted research and constitutes the primary content of this bachelor's thesis.

To begin, Section 5.1 outlines the scope of this research, emphasizing the most relevant outcomes for this work. Subsequently, Section 5.2 elaborates on these significant findings. Finally, in Section 5.3, a comprehensive discussion and analysis of the recent advancements take place.

It's worth noting that, except for the initial section (5.1), all subsequent sections are directly derived from the ongoing research documented in our publication [4].

5.1 Scope of Research

The comprehensive findings of this research are encapsulated in the following four maps (Fig.5.1).

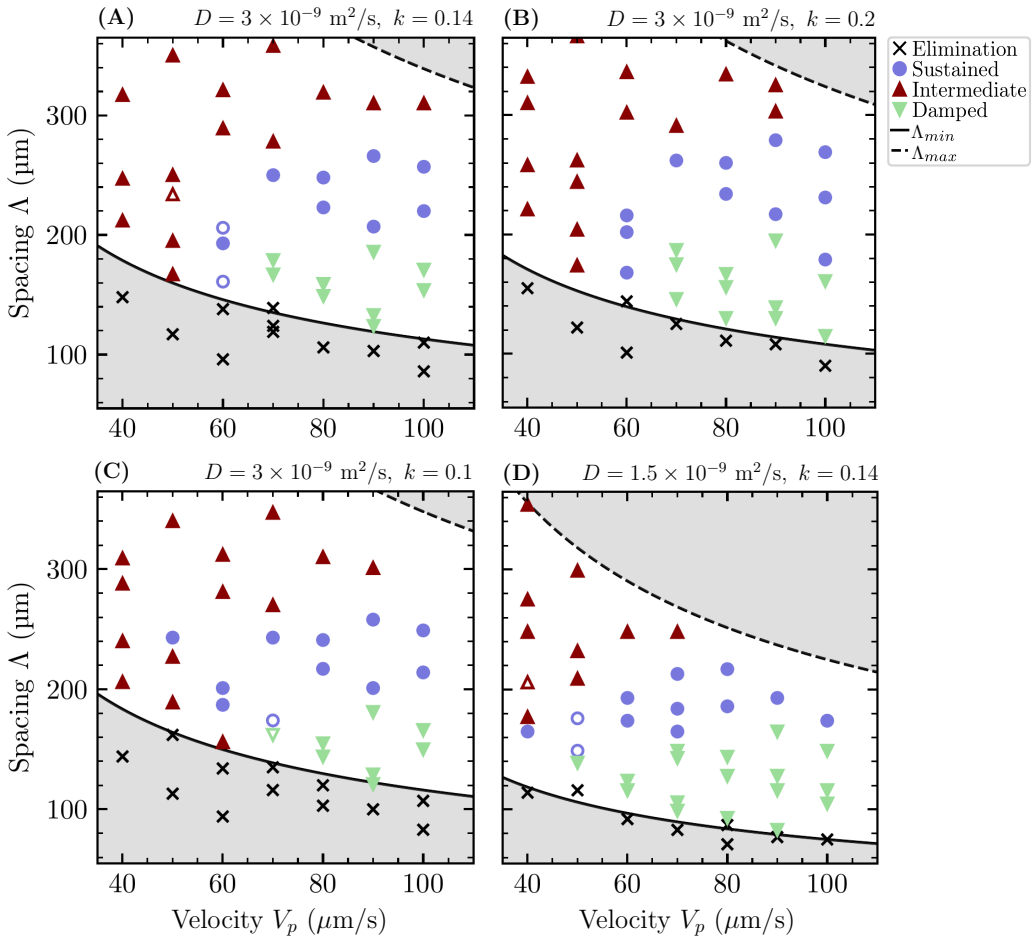


Figure 5.1: Oscillation characterization maps for the Al-4at.%Cu alloy, exploring variations in parameters, including diffusion coefficient (D) and partition coefficient (k). Open symbols represent unclassified behaviors.

These maps constitute the study of oscillatory behavior in the Al-4at.%Cu binary alloy. The map labeled as (A) serves as the initial point of investigation, employing well-established parameters as referenced in [56, 99]. Progressing from (A), we introduced slight modifications to two key parameters, namely the diffusion coefficient (D) and the partition coefficient (k), to

5. RESULTS

observe their influence on oscillatory phenomena. The subsequent simulations, labeled as (B) and (C), retained the original diffusivity while varying the partition coefficient, spanning from 0.14 to 0.2 and then down to 0.1. Lastly, simulation (D) entailed adjustments to the diffusivity while maintaining a constant partition coefficient, specifically reducing D from 3 to 1.5. Further details on the research planning have already been discussed in subsection 4.3.3.

While this study covers a broad scope, it's important to note that only map (A) has been comprehensively characterized and will be presented and discussed extensively in the followings sections.

5.2 Oscillatory Behavior Map

Figure 5.2 shows the resulting map of growth behaviors as a function of pulling velocity V_p and primary spacing Λ . As a first conclusion, it was indeed possible to obtain sustained oscillatory growth for several simulations over a range of (V_p, Λ) . Oscillations were only found above a minimum velocity, here for $V_p \geq 60 \text{ } \mu\text{m/s}$. Most cases (all but one) leading to sustained oscillations (\bullet symbols) fall within a spacing range $190 \leq \Lambda/\mu\text{m} \leq 270$, while damped oscillations (\blacktriangledown symbols) emerge within $120 \leq \Lambda/\mu\text{m} \leq 190$. While different symbol types denote the classification criteria mentioned in Section 4.5.2, their color follows a discrete distribution as a function of the ratio of average fluid velocity \bar{V} over pulling velocity V_p , namely: light green ($\bar{V}/V_p \leq 0.05$), medium blue ($0.05 \leq \bar{V}/V_p \leq 2.5$), or dark red ($\bar{V}/V_p \geq 2.5$). Except for a few data points around the sustained/noisy transition, the reasonable match between symbol types and colors shows that we can correlate the occurrence of damped, sustained, or noisy oscillations to the ratio \bar{V}/V_p . However, the current threshold values for \bar{V}/V_p , here denoted $\xi_1 \approx 0.05$ (damped/sustained) and $\xi_2 \approx 2.5$ (sustained/noisy), differ from those identified in Isensee and Tourret previous study focused on CMSX-4 ($\xi_1 \approx 1.0$, $\xi_2 \approx 2.0$), such that they may depend upon alloy parameters and/or processing conditions (e.g., temperature gradient). Below, we describe and discuss in further details the different growth behaviors observed in our simulations.

5.3 Discussion

5.3.1 Elimination ($\Lambda < \Lambda_{\min}$)

As expected, for each V_p , the lowest spacings lead to the elimination of at least one primary dendrite, marking the lower limit of the stable spacing range, Λ_{\min} . This minimal stable spacing appears to reasonably match the expected power law $\Lambda_{\min} \sim V^{-1/2}$ (solid black line). The ratio between the lower and upper limits of the stable spacing range $\Lambda_{\max}/\Lambda_{\min}$ typically varies between 2 and 5 [31, 105, 7]. Since the current simulations do not include sidebranching, they cannot predict the upper limit (as done, e.g., in Refs [105, 7]). Hence, once we had an estimate of Λ_{\min} for a given V_p , we approximated $\Lambda_{\max} \approx 3 \Lambda_{\min}$ (black dashed line) and did not perform any simulation above this Λ_{\max} , because such a situation would in reality likely lead to spacing reduction by tertiary sidebranching [105, 7].

5.3.2 Damped oscillations ($\Lambda \gtrsim \Lambda_{\min}$)

Above a certain velocity, here $\approx 75 \text{ } \mu\text{m/s}$, the lowest stable spacings just above Λ_{\min} lead to damped oscillations. These are illustrated in Figure 5.3 for two representative case, namely

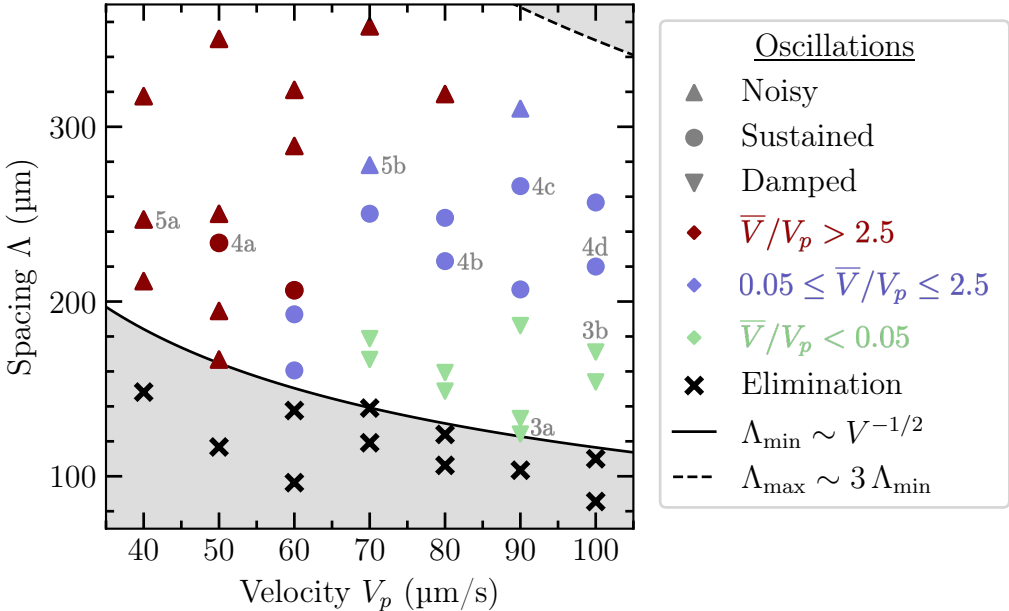


Figure 5.2: Oscillatory behavior map. Symbols types denote different growth behaviors: (\times) elimination events for $\Lambda < \Lambda_{\min}$ (black line) or (\blacktriangledown) damped, (\bullet) sustained, or (\blacktriangle) noisy oscillations. Symbols are colored according to the ratio \bar{V}/V_p . Gray text labels next to symbols mark cases highlighted in the following figures and discussion.

for (a) $V = 90$ μm/s and $\Lambda = 124$ μm/s and for (b) $V = 100$ μm/s and $\Lambda = 171$ μm. They respectively correspond to the lowest ($\tau = 16.7$ s) and highest ($\tau = 3.13$ s) damping rates obtained among the 44 simulations. While we did not collect sufficient data to extract meaningful scaling laws, we observed that the damping rate typically increases (i.e., τ decreases) when either V_p or Λ increases. In this regime, the behavior of all needles in the array is homogeneous and synchronized (typically oscillating in phase with one another).

From Figure 5.3 on, velocity fields are shown via the flow streamlines, of which the opacity decreases progressively when the fluid velocity is lower than $0.2V_{\max}$, with V_{\max} the maximum fluid velocity over the entire domain. This allows illustrating that, within the damped oscillation regime (Fig. 5.3), while some convective currents appear around and between the dendrites, the fluid velocity vanishes within a narrow boundary layer ahead of the solidification front. Transport of solute beyond this boundary layer occurs then primarily through diffusion.

5.3.3 Sustained oscillations (intermediate Λ)

Within the inspected range, for a sufficient pulling velocity, at intermediate primary spacings Λ , sustained oscillations occur. Typical cases are illustrated in Figure 5.4 for (a) $V = 50$ μm/s and $\Lambda = 234$ μm, (b) $V = 80$ μm/s and $\Lambda = 223$ μm, (c) $V = 90$ μm/s and $\Lambda = 266$ μm, and (d) $V = 100$ μm/s and $\Lambda = 220$ μm. Among these, Fig. 5.4c is a good illustration of a typical sustained oscillatory regime. Therein, all needles exhibit an oscillatory growth, with a small variability of oscillation amplitudes and frequencies throughout the array. As seen on the leftmost panel, prominent convection vortices appear in the liquid, and needle oscillations are desynchronized (not in phase) with one another.

In some cases, illustrated by Fig. 5.4b and d, the oscillatory growth regime emerges after a usually short (b) but potentially long (d) transient period, momentarily more akin to a damped oscillation regime before a subsequent amplification of the oscillation amplitude toward a steady

5. RESULTS

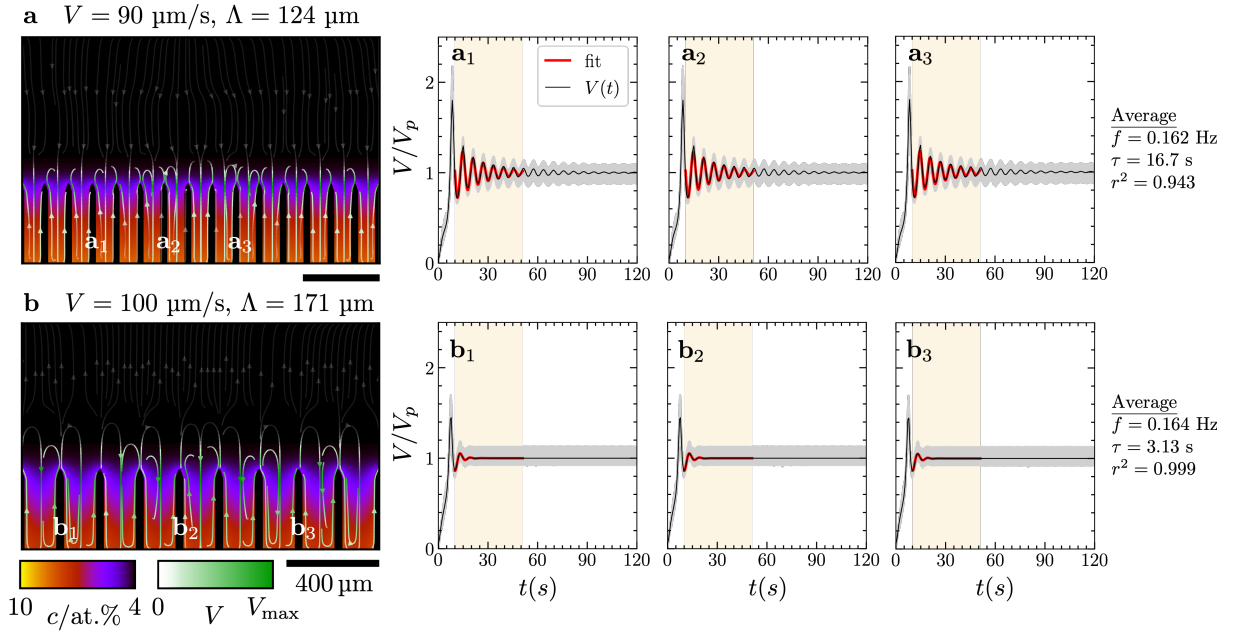


Figure 5.3: Damped oscillations (a) for $V = 90 \mu\text{m}/\text{s}$ and $\Lambda = 124 \mu\text{m}$ and (b) for $V = 100 \mu\text{m}/\text{s}$ and $\Lambda = 171 \mu\text{m}$. (left) Concentration field (color map) and fluid flow (streamlines) at $t = 120 \text{ s}$. Streamlines are progressively transparent toward lowest velocities (from opaque at $V/V_{\max} \geq 0.2$ to 90% transparent at $V = 0$). (right) Tip velocities of selected needles, showing raw (gray) and smoothed (black) $V(t)$ as well as fitted function (thick red) and range (shaded background).

value. (For this reason, several runs classified as damped were performed for longer durations in order to ascertain that they were indeed not in a transient state.) Such simulations exhibiting a transient regime were observed for the lowest Λ data point classified as sustained at $V = 80, 90$, and $100 \mu\text{m}/\text{s}$, i.e., close to the edge of the transition between damped and sustained oscillations (Fig. 5.2). The corresponding convective patterns are also intermediate, with vanishing velocities toward the top of the domain (like for damped oscillations at lower Λ) and the emergence of small nascent convection rolls (like for sustained oscillations at higher Λ).

Finally, Fig. 5.4a shows the other end of the sustained oscillation spectrum, at the edge of the transition toward noisy oscillations. This specific case corresponds to the lone outlier data point classified as “sustained” for $V = 50 \mu\text{m}/\text{s}$ in Fig. 5.2, due to its $r^2 = 0.847$ higher than the chosen threshold of 0.8. However, in spite of a relatively good fit to $v_2(t)$, Fig. 5.4a shows that resulting $V(t)$ look relatively noisy (see, e.g., Fig. 5.4a₃). In such cases, strong convection vortices are present within the liquid.

Among the sustained oscillations, measured frequencies range from 0.155 to 0.230 Hz (i.e., periods from 4.35 to 6.45 s), without any conclusive dependence upon Λ or V_p emerging within the investigated range of conditions. Naturally, the oscillation amplitude scales approximately like V_p and tends to increase toward high Λ when the $V(t)$ signals become more spiky.

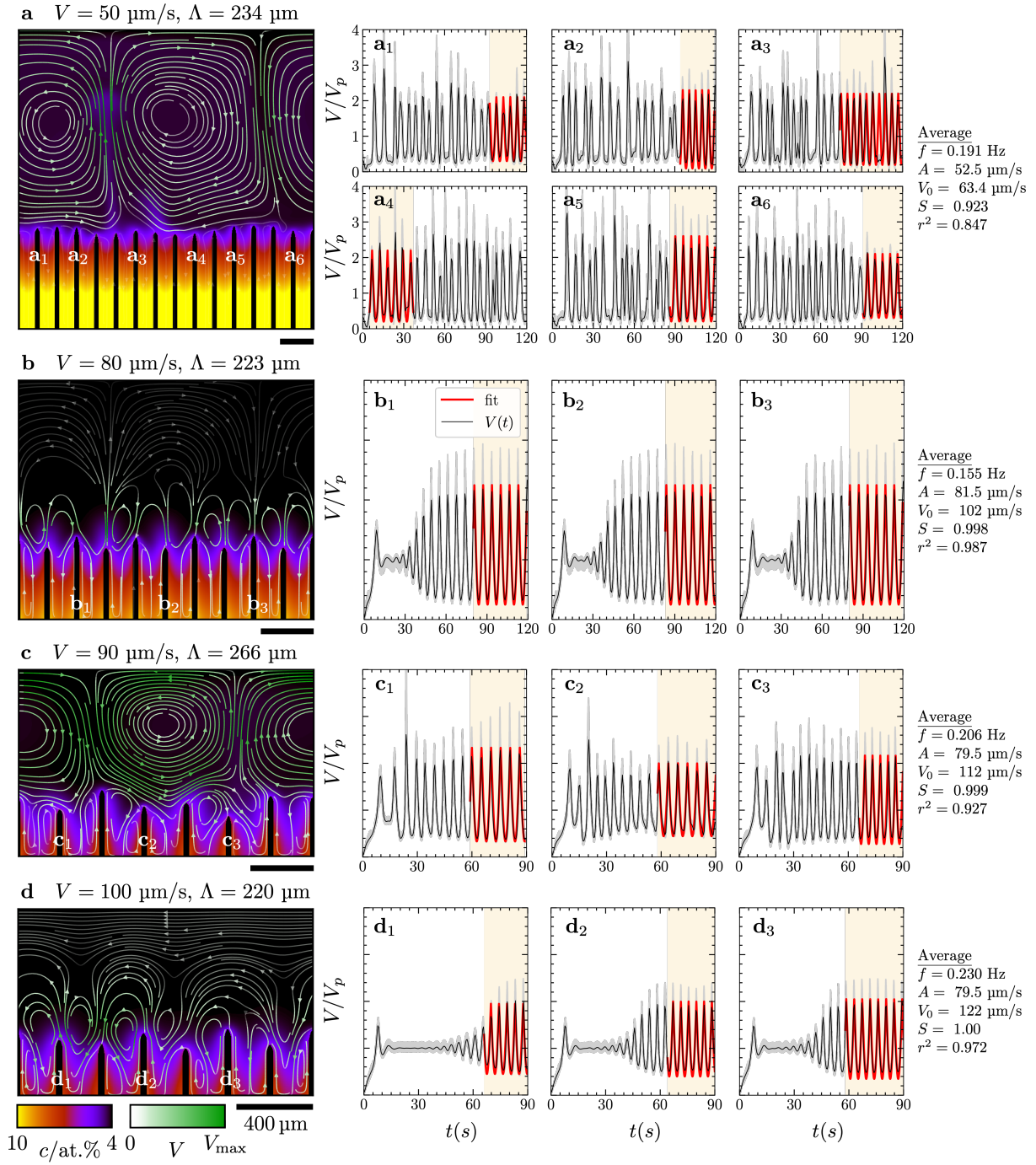


Figure 5.4: *Sustained oscillations for (a) $V = 50 \mu\text{m/s}$ and $\Lambda = 234 \mu\text{m}$, (b) $V = 80 \mu\text{m/s}$ and $\Lambda = 223 \mu\text{m}$, (c) $V = 90 \mu\text{m/s}$ and $\Lambda = 266 \mu\text{m}$, (d) $V = 100 \mu\text{m/s}$ and $\Lambda = 220 \mu\text{m}$. (left) Concentration field (color map) and fluid flow (streamlines, from opaque at $V/V_{\max} \geq 0.2$ to 90% transparent at $V = 0$) at $t = (a,b)$ 120 s and (c,d) 90 s. (right) Tip velocities of selected needles, showing raw (gray) and smoothed (black) $V(t)$ as well as fitted function (thick red) and range (shaded background).*

5.3.4 Noisy oscillations (high Λ)

As shown in Figure 5.5, at high primary spacings, or across all stable spacings for low V_p , the velocities deviate more prominently from the prototypical behaviors illustrated in Fig. 4.2.

Figure 5.5a shows the worst encountered fit with $r^2 = 0.590$ and Fig. 5.5b a case closer to

5. RESULTS

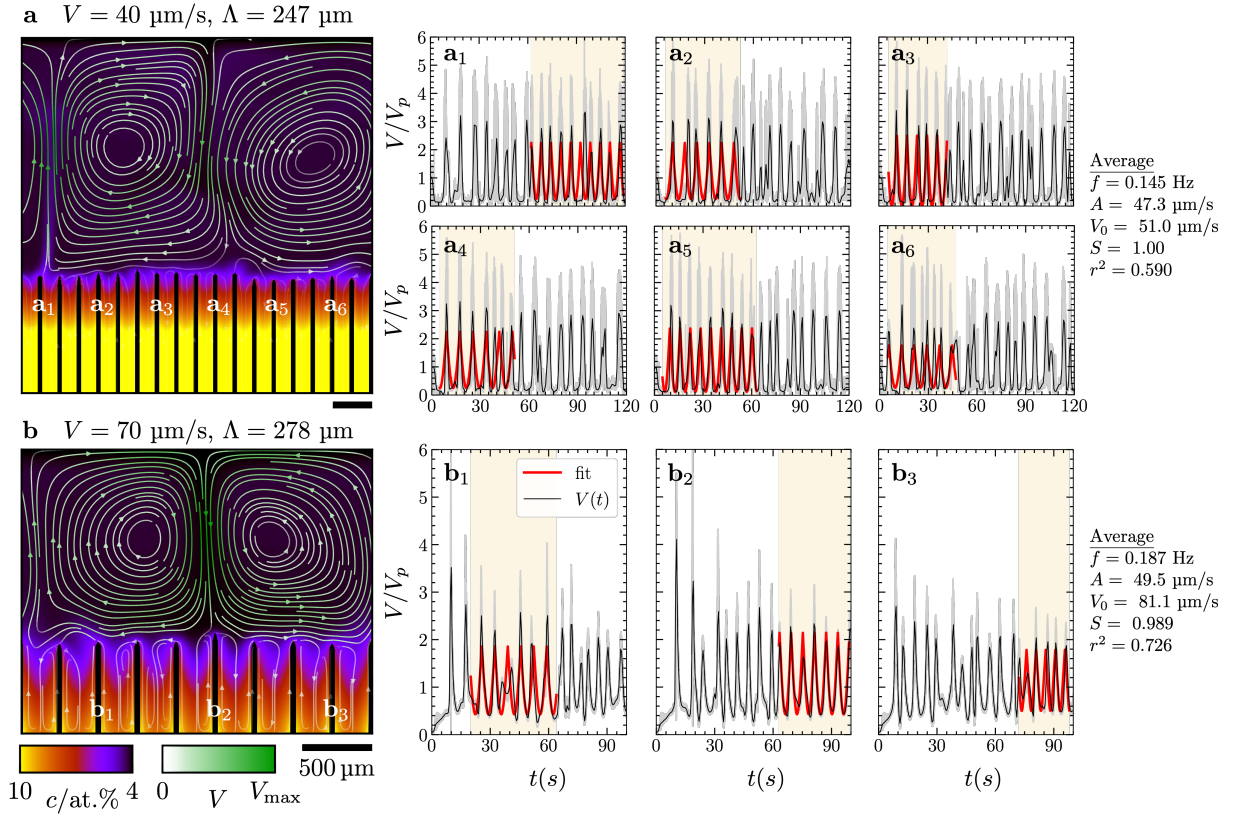


Figure 5.5: *Noisy oscillations for (a) $V = 40 \mu\text{m}/\text{s}$ and $\Lambda = 247 \mu\text{m}$, and (b) $V = 70 \mu\text{m}/\text{s}$ and $\Lambda = 278 \mu\text{m}$. (left) Concentration field (color map) and fluid flow (streamlines, from opaque at $V/V_{\max} \geq 0.2$ to 90% transparent at $V = 0$) at $t =$ (a) 120 s and (b) 100 s. (right) Tip velocities of selected needles, showing raw (gray) and smoothed (black) $V(t)$ as well as fitted function (thick red) and range (shaded background).*

the edge of the transition between the “sustained” and “noisy” regions of Fig. 5.2. While the $V(t)$ signals are clearly noisy and cannot be assimilated to any clear periodic function, both of them still exhibit an emerging frequency close to that of the sustained oscillations, namely with $0.134 < f/\text{Hz} < 0.255$ (i.e., periods between 3.92 and 7.46 s) across the investigated range of noisy oscillations. This behavior remains quite different from the burst-like growth encountered for CMSX-4 simulations at low V_p [56]. All cases of noisy oscillations exhibit prominent convection rolls in the liquid phase.

6 CONCLUSIONS AND FUTURE WORK

The concluding remarks have been structured into three distinct sections. Firstly, we will discuss the thesis itself, which represents a significant milestone in our undergraduate journey. This section, will provide an opportunity for reflection. Subsequently, we will present the research findings and conclusions, offering a comprehensive overview of the contributions of our work. To conclude this discussion, in alignment with the initial quote of this document, we will delve into the ethical and professional dimensions, while also considering their relationship with the Sustainable Development Goals.

6.1 Conclusions

On one hand, as an academic achievement, the completion of this thesis has afforded me a profound understanding of solidification theory, particularly in its application to metals. In addition, I have been introduced in the field of research, approaching the reading of papers and the study of state-of-the-art theories and models. Moreover, regarding the computational side, I had the opportunity to learn a new widely used programming language (Python) and to develop advanced algorithms for data extraction and post-processing. Likewise, I have deepened in the handling of Linux-based environments and the use of the terminal. Finally, in the context of the research carried out, which involves supercomputing, I have been able to get started in the launching of simulations using a queue manager (Slurm) on a cluster of GPUs.

From the other hand and regarding the performed research, we have investigated the conditions of occurrence and characteristics of buoyancy-driven oscillations of primary dendrite growth velocities in directional solidification using multiscale dendritic needle network (DNN) simulations. While it was previously studied experimentally [90] and computationally [56] for a Ni-based alloy, here we reproduce comparable behaviors using a binary Al-4at.%Cu alloy. These results suggest that this phenomenon may be general to any binary alloy, provided the appropriate (G , V_p , Λ) conditions. We confirmed that the ratio between average fluid velocity \bar{V} and pulling velocity V_p provides a reasonable indicator of the oscillatory regime (namely: damped, sustained, or noisy). However, the threshold values separating regimes differ from those identified for CMSX-4 under different processing conditions [56]. Here, the transition from damped to sustained oscillations occurs together with the onset of appearance of convection vortices in the fluid. This is also in contrast with previous results for CMSX-4 [90, 56], exhibiting well-established convection rolls in both regimes. Our results also did not capture the further expected transition from sustained to damped oscillations when increasing V_p (i.e., cooling rate [90, 56]), perhaps because it occurs at higher V_p than those explored here. Moreover, the effect of the null velocity imposed at the solid-liquid interface – in contrast, e.g., to imposing the growth velocity, accounting for the solid-liquid density change, or tracking the solid fraction into a mushy region – remains to be investigated.

Eventually, the research conducted aligns with Sustainable Development Goals 9 and 12, primarily due to its innovative nature. The focus on modeling and computational analysis addresses a critical aspect of technological advancement, particularly within the aeronautical sector. Processes reliant on directional solidification, such as the production of steam turbine blades and aircraft engines, are inherently intricate and presently cost-intensive. Given the pivotal role these components play in ensuring efficient energy production or optimal passenger safety, it becomes imperative to delve deeper into the factors influencing stable and uniform directional solidification conditions. This in-depth understanding holds the potential to revolutionize industrial component manufacturing, curbing the substantial waste typically incurred due to defects

arising from suboptimal process conditions.

6.2 Future Work

Some open questions remain on buoyancy-driven oscillations in directional solidification. Among other things, it remains unclear whether the phenomenon is relevant to bulk samples or is promoted by the 2D configuration (or quasi-2D thin-sample confinement in experiments). Ongoing work, directly following up from the present study, will clarify the dependence of oscillatory behavior upon different alloy parameters (such as diffusion coefficient D and partition coefficient k), i.e., fully characterizing the other three remaining behavior maps (B, C and D). Scanning a broader range of alloy parameters and processing conditions will allow us to extract more meaningful scaling laws for the oscillation characteristics, and to establish general rules governing the stability of dendritic fronts in directional solidification processes.

REFERENCES

- [1] S. Akamatsu, G. Faivre, and T. Ihle. “Symmetry-broken double fingers and seaweed patterns in thin-film directional solidification of a nonfaceted cubic crystal”. In: *Physical Review E* 51.5 (1995), p. 4751.
- [2] D. R. Askeland, P. P. Phulé, W. J. Wright, and D. Bhattacharya. *The science and engineering of materials*. 6th ed. Springer, 2003, pp. 305–331.
- [3] P. Aubertin, T. Wang, S. Cockcroft, and A. Mitchell. “Freckle formation and freckle criterion in superalloy castings”. In: *Metallurgical and materials transactions B* 31.4 (2000), pp. 801–811. URL: [http://refhub.elsevier.com/S1359-6454\(22\)00416-5/sbref0020](http://refhub.elsevier.com/S1359-6454(22)00416-5/sbref0020).
- [4] J. M. Barberá, T. Isensee, and D. Tourret. “On the occurrence of buoyancy-induced oscillatory growth instability in directional solidification of alloys”. In: *IOP Conference Series: Materials Science and Engineering* 1281.1 (May 2023), p. 012050. doi: [10.1088/1757-899X/1281/1/012050](https://doi.org/10.1088/1757-899X/1281/1/012050). URL: <https://dx.doi.org/10.1088/1757-899X/1281/1/012050>.
- [5] C. C. Battaile, R. N. Grugel, A. B. Hmelo, and T. G. Wang. “The effect of enhanced gravity levels on microstructural development in Pb-50 wt pct Sn alloys during controlled directional solidification”. In: *Metallurgical and Materials Transactions A* 25 (1994), pp. 865–870. doi: [10.1007/BF02665463](https://doi.org/10.1007/BF02665463). URL: <https://link.springer.com/article/10.1007/BF02665463>.
- [6] M. Becker, L. Sturz, D. Bräuer, and F. Kargl. “A comparative in situ X-radiography and DNN model study of solidification characteristics of an equiaxed dendritic Al-Ge alloy sample”. In: *Acta Materialia* 201 (2020), pp. 286–302. ISSN: 1359-6454. doi: [10.1016/j.actamat.2020.09.078](https://doi.org/10.1016/j.actamat.2020.09.078). URL: <https://www.sciencedirect.com/science/article/pii/S1359645420307801>.
- [7] B. Bellon et al. “Multiscale prediction of microstructure length scales in metallic alloy casting”. In: *Acta Materialia* 207 (2021), p. 116686. ISSN: 1359-6454. doi: [10.1016/j.actamat.2021.116686](https://doi.org/10.1016/j.actamat.2021.116686). URL: <https://www.sciencedirect.com/science/article/pii/S1359645421000665>.
- [8] N. Bergeon et al. “Spatiotemporal dynamics of oscillatory cellular patterns in three-dimensional directional solidification”. In: *Physical review letters* 110.22 (2013), p. 226102.
- [9] W. J. Boettinger et al. “Solidification microstructures: recent developments, future directions”. In: *Acta materialia* 48.1 (2000), pp. 43–70.
- [10] A. Bogni et al. “Application of synchrotron X-ray radiography to the study of dendritic equiaxed microstructure formation in Al-Cu alloys”. In: *Nuclear Instruments and Methods in Physics Research Section B: Beam Interactions with Materials and Atoms* 268.3 (2010). X-ray Techniques for Advanced Materials, Nanostructures and Thin Films: from Laboratory Sources to Synchrotron Radiation, pp. 394–398. ISSN: 0168-583X. doi: [10.1016/j.nimb.2009.09.011](https://doi.org/10.1016/j.nimb.2009.09.011). URL: <https://www.sciencedirect.com/science/article/pii/S0168583X09009781>.

- [11] A. Bogno et al. “Analysis by synchrotron X-ray radiography of convection effects on the dynamic evolution of the solid–liquid interface and on solute distribution during the initial transient of solidification”. In: *Acta Materialia* 59.11 (2011), pp. 4356–4365. ISSN: 1359-6454. DOI: <https://doi.org/10.1016/j.actamat.2011.03.059>. URL: <https://www.sciencedirect.com/science/article/pii/S135964541100214X>.
- [12] P. Bouissou and P. Pelce. “Effect of a forced flow on dendritic growth”. In: *Physical Review A* 40 (1989), pp. 6673–6680. DOI: [10.1103/PhysRevA.40.6673](https://doi.org/10.1103/PhysRevA.40.6673). URL: <https://journals.aps.org/prb/abstract/10.1103/PhysRevA.40.6673>.
- [13] W. Brentnall et al. “Extensive Industrial Gas Turbine Experience With Second Generation Single Crystal Alloy Turbine Blades”. In: *Turbo Expo: Power for Land, Sea, and Air*. Vol. 78712. American Society of Mechanical Engineers. 1997.
- [14] R. Broomfield et al. “Development and Turbine Engine Performance of Three Advanced Rhenium Containing Superalloys for Single Crystal and Directionally Solidified Blades and Vanes”. In: *Journal of Engineering for Gas Turbines and Power-transactions of The Asme - J ENG GAS TURB POWER-T ASME* 120 (July 1998), pp. 595–600. DOI: [10.1115/1.2818188](https://doi.org/10.1115/1.2818188).
- [15] P. Burkholder et al. “Allison engine testing CMSX-4 single crystal turbine blades and vanes”. In: *3 rd International Charles Parsons Turbine Conference: Materials Engineering in Turbines and Compressors*. 1995, pp. 305–320.
- [16] U. of Cambridge. *Solute Partitioning*. 2009. URL: https://www.doitpoms.ac.uk/tlplib/solidification_alloys/solute_partitioning.php.
- [17] Cannon Muskegon2. 2000. URL: <https://cannonmuskegon.com/>.
- [18] S.-K. Chan, H.-H. Reimer, and M. Kahlweit. “On the stationary growth shapes of NH₄Cl dendrites”. In: *Journal of Crystal Growth* 32.3 (1976), pp. 303–315.
- [19] C.-H. Chen, A. M. Tabrizi, P.-A. Geslin, and A. Karma. “Dendritic needle network modeling of the Columnar-to-Equiaxed Transition. Part II: three dimensional formulation, implementation and comparison with experiments”. In: *Acta Materialia* 202 (2021), pp. 463–477. ISSN: 1359-6454. DOI: [10.1016/j.actamat.2020.10.012](https://doi.org/10.1016/j.actamat.2020.10.012). URL: <https://www.sciencedirect.com/science/article/pii/S1359645420308016>.
- [20] L.-Q. Chen. “Phase-field models for microstructure evolution”. In: *Annual review of materials research* 32.1 (2002), pp. 113–140.
- [21] S. Chen, G. Guillemot, and C.-A. Gandin. “Three-dimensional cellular automaton-finite element modeling of solidification grain structures for arc-welding processes”. In: *Acta Materialia* 115 (2016), pp. 448–467. ISSN: 1359-6454. DOI: [10.1016/j.actamat.2016.05.011](https://doi.org/10.1016/j.actamat.2016.05.011). URL: <https://www.sciencedirect.com/science/article/pii/S1359645416303391>.
- [22] A. J. Chorin. “Numerical solution of the Navier-Stokes equations”. In: *Mathematics of Computation* 2 (1968), pp. 745–762. DOI: [10.1090/S0025-5718-1968-0242392-2](https://doi.org/10.1090/S0025-5718-1968-0242392-2). URL: <https://www.ams.org/journals/mcom/1968-22-104/S0025-5718-1968-0242392-2/>.

- [23] A. Clarke et al. “Microstructure selection in thin-sample directional solidification of an Al-Cu alloy: In situ X-ray imaging and phase-field simulations”. In: *Acta Materialia* 129 (2017), pp. 203–216. ISSN: 1359-6454. DOI: [10.1016/j.actamat.2017.02.047](https://doi.org/10.1016/j.actamat.2017.02.047). URL: <https://www.sciencedirect.com/science/article/pii/S1359645417301489>.
- [24] H. Combeau, M. Založník, and S. Hans. “Prediction of Macrosegregation in Steel Ingots: Influence of the Motion and the Morphology of Equiaxed Grains”. In: *Metallurgical and Materials Transactions B* 40 (2009), pp. 289–304. DOI: [10.1007/s11663-008-9178-y](https://doi.org/10.1007/s11663-008-9178-y). URL: <https://link.springer.com/article/10.1007/s11663-008-9178-y>.
- [25] S. Copley, A. F. Giamei, S. Johnson, and M. Hornbecker. “The origin of freckles in unidirectionally solidified castings”. In: *Metallurgical transactions* 1 (1970), pp. 2193–2204.
- [26] Y. Couder, J. Maurer, R. González-Cinca, and A. Hernández-Machado. “Side-branch growth in two-dimensional dendrites. I. Experiments”. In: *Phys. Rev. E* 71 (3 Mar. 2005), p. 031602. DOI: [10.1103/PhysRevE.71.031602](https://doi.org/10.1103/PhysRevE.71.031602). URL: <https://link.aps.org/doi/10.1103/PhysRevE.71.031602>.
- [27] N. D’souza, M. Ardakani, M. McLean, and B. Shollock. “Directional and single-crystal solidification of Ni-base superalloys: Part I. The role of curved isotherms on grain selection”. In: *Metallurgical and Materials Transactions A* 31 (2000), pp. 2877–2886.
- [28] J. A. Dantzig and M. Rappaz. *Solidification*. Materials. Lausanne, Switzerland: EPFL Press, 2009. ISBN: 978-2-940222-17-9. URL: [http://refhub.elsevier.com/S1359-6454\(16\)30619-X/sref4](http://refhub.elsevier.com/S1359-6454(16)30619-X/sref4).
- [29] M. Dupouy, D. Camel, and J. Favier. “Natural convection in directional dendritic solidification of metallic alloys—I. Macroscopic effects”. In: *Acta Metallurgica* 37.4 (1989), pp. 1143–1157. ISSN: 0001-6160. DOI: [10.1016/0001-6160\(89\)90110-7](https://doi.org/10.1016/0001-6160(89)90110-7). URL: <https://www.sciencedirect.com/science/article/abs/pii/0001616089901107>.
- [30] M. Dupouy, D. Camel, and J. Favier. “Natural convective effects in directional dendritic solidification of binary metallic alloys: Dendritic array primary spacing”. In: *Acta Metallurgica et Materialia* 40.7 (1992), pp. 1791–1801. ISSN: 0956-7151. DOI: [https://doi.org/10.1016/0956-7151\(92\)90122-U](https://doi.org/10.1016/0956-7151(92)90122-U). URL: <https://www.sciencedirect.com/science/article/pii/095671519290122U>.
- [31] B. Echebarria, A. Karma, and S. Gurevich. “Onset of sidebranching in directional solidification”. In: *Physical Review E* 81 (2 2010), p. 021608. DOI: [10.1103/PhysRevE.81.021608](https://doi.org/10.1103/PhysRevE.81.021608). URL: <https://link.aps.org/doi/10.1103/PhysRevE.81.021608>.
- [32] J. L. Enríquez Berciano, E. Tremps Guerra, S. d. Elío de Bengy, and D. Fernández Segovia. “Colada de acero”. In: (2009). URL: https://oa.upm.es/1669/1/MONO_TREMPs_2009_01.pdf.
- [33] *España - Precios de la electricidad de los hogares*. es. <https://datosmacro.expansion.com/energia-y-medio-ambiente/electricidad-precio-hogares/espana>. Accessed: 2023-9-4. Apr. 2023.

- [34] D. Fisher and W. Kurz. “Fundamentals of Solidification”. In: *Fundamentals of Solidification* (1999), pp. 1–316.
- [35] M. Flemings. *Solidification Processing*. New York: McGraw Hill, 1974.
- [36] R. Fleurisson, O. Senniger, G. Guillemot, and C.-A. Gandin. “Hybrid Cellular Automaton - Parabolic Thick Needle model for equiaxed dendritic solidification”. In: *Journal of Materials Science & Technology* 124 (2022), pp. 26–40. ISSN: 1005-0302. DOI: [10.1016/j.jmst.2022.02.017](https://doi.org/10.1016/j.jmst.2022.02.017). URL: <https://www.sciencedirect.com/science/article/pii/S1005030222002572>.
- [37] S. P. Frankel. “Convergence Rates of Iterative Treatments of Partial Differential Equations”. In: *Mathematical Tables and Other Aids to Computation* 4.30 (1950), pp. 65–75. DOI: [10.2307/2002770](https://doi.org/10.2307/2002770). URL: <https://www.jstor.org/stable/2002770>.
- [38] D. Frasier, J. Whetstone, K. Harris, G. Erickson, and R. Schwer. “Process and alloy optimization for CMSX-4 superalloy single crystal airfoils”. In: *High temperature materials for power engineering* (1990), pp. 1281–1300.
- [39] K. Fullagar et al. “Aero engine test experience with CMSX-4 alloy single-crystal turbine blades”. In: *Journal of Engineering for Gas Turbines and Power* 118.2 (1996), pp. 380–388. DOI: [10.1115/1.2816600](https://doi.org/10.1115/1.2816600).
- [40] C.-A. Gandin and M. Rappaz. “A coupled finite element-cellular automaton model for the prediction of dendritic grain structures in solidification processes”. In: *Acta Metallurgica et Materialia* 42.7 (1994), pp. 2233–2246. ISSN: 0956-7151. DOI: [10.1016/0956-7151\(94\)90302-6](https://doi.org/10.1016/0956-7151(94)90302-6). URL: <https://www.sciencedirect.com/science/article/abs/pii/0956715194903026>.
- [41] M. Georgelin and A. Pocheau. “Oscillatory instability, limit cycle, and transition to doublets in directional solidification”. In: *Physical review letters* 79.14 (1997), p. 2698.
- [42] P.-A. Geslin, C.-H. Chen, A. M. Tabrizi, and A. Karma. “Dendritic needle network modeling of the Columnar-to-Equiaxed transition. Part I: two dimensional formulation and comparison with theory”. In: *Acta Materialia* 202 (2021), pp. 42–54. ISSN: 1359-6454. DOI: [10.1016/j.actamat.2020.10.009](https://doi.org/10.1016/j.actamat.2020.10.009). URL: <https://www.sciencedirect.com/science/article/pii/S1359645420307989>.
- [43] A. F. Giamei and B. Kear. “On the nature of freckles in nickel base superalloys”. In: *Metallurgical Transactions* 1.8 (1970), pp. 2185–2192. URL: [http://refhub.elsevier.com/S1359-6454\(22\)00416-5/sbref0018](http://refhub.elsevier.com/S1359-6454(22)00416-5/sbref0018).
- [44] J. W. Gibbs et al. “In Situ X-Ray Observations of Dendritic Fragmentation During Directional Solidification of a Sn-Bi Alloy”. In: *JOM* 68 (2016), pp. 170–177. DOI: [10.1007/s11837-015-1646-7](https://doi.org/10.1007/s11837-015-1646-7). URL: <https://link.springer.com/article/10.1007/s11837-015-1646-7>.
- [45] M. Glicksman and S. Marsh. *Handbook of Crystal Growth vol 1b ed DTJ Hurle*. 1993.
- [46] M. Glicksman, R. Schaefer, and J. Ayers. “Dendritic growth-a test of theory”. In: *Metallurgical Transactions A* 7 (1976), pp. 1747–1759.

- [47] M. Glicksmann, M. Koss, and E. Winsa. “Dendritic growth velocities in microgravity”. In: *Physical Review Letters* 73.4 (1994), pp. 573–576. DOI: [10.1103/PhysRevLett.73.573](https://doi.org/10.1103/PhysRevLett.73.573). URL: <https://journals.aps.org/prl/abstract/10.1103/PhysRevLett.73.573>.
- [48] M. Griebel, T. Dornseifer, and T. Neunhoeffer. *Numerical Simulation in Fluid Dynamics: A Practical Introduction*. Philadelphia, PA, USA: Society for Industrial and Applied Mathematics, 1998. ISBN: 978-0898713985. DOI: [10.1137/1.9780898719703](https://doi.org/10.1137/1.9780898719703). URL: <https://epubs.siam.org/doi/book/10.1137/1.9780898719703>.
- [49] R. Grugel. “Secondary and tertiary dendrite arm spacing relationships in directionally solidified Al-Si alloys”. In: *Journal of materials science* 28 (1993), pp. 677–683.
- [50] K. Harris et al. “Development of the rhenium containing superalloys CMSX-4 reg-sign and CM 186 LC reg-sign for single crystal blade and directionally solidified vane applications in advanced turbine engines”. In: *Superalloys 1992*. 1992. DOI: [10.1007/BF02661730](https://doi.org/10.1007/BF02661730). URL: <https://doi.org/10.1007/BF02661730>.
- [51] K. Harris and J. B. Wahl. “Improved single crystal superalloys, CMSX-4 (SLS)[La+ Y] and CMSX-486”. In: *Superalloys, Proceedings of the 10th International Symposium on Superalloys 2004* (2004), pp. 45–52. DOI: [10.7449/2004/Superalloys_2004_45_52](https://doi.org/10.7449/2004/Superalloys_2004_45_52).
- [52] A. Hellawell, J. Sarazin, and R. Steube. “Channel convection in partly solidified systems”. In: *Philosophical Transactions of the Royal Society of London. Series A: Physical and Engineering Sciences* 345.1677 (1993), pp. 507–544.
- [53] J. J. Hoyt, M. Asta, and A. Karma. “Method for Computing the Anisotropy of the Solid-Liquid Interfacial Free Energy”. In: *Physical Review Letters* 86 (2001), pp. 5530–3. DOI: [10.1103/PhysRevLett.86.5530](https://doi.org/10.1103/PhysRevLett.86.5530). URL: <https://journals.aps.org/prl/abstract/10.1103/PhysRevLett.86.5530>.
- [54] J. J. Hoyt, M. Asta, and A. Karma. “Atomistic and continuum modeling of dendritic solidification”. In: *Materials Science and Engineering: R: Reports* 41.6 (2003), pp. 121–163. ISSN: 0927-796X. DOI: [10.1016/S0927-796X\(03\)00036-6](https://doi.org/10.1016/S0927-796X(03)00036-6). URL: <https://www.sciencedirect.com/science/article/pii/S0927796X03000366>.
- [55] T. Isensee and D. Tourret. “Three-dimensional needle network model for dendritic growth with fluid flow”. In: *IOP Conference Series: Materials Science and Engineering* 861 (2020), p. 012049. DOI: [10.1088/1757-899X/861/1/012049](https://doi.org/10.1088/1757-899X/861/1/012049). URL: <https://iopscience.iop.org/article/10.1088/1757-899X/861/1/012049>.
- [56] T. Isensee and D. Tourret. “Convective effects on columnar dendritic solidification – A multiscale dendritic needle network study”. In: *Acta Materialia* 234 (2022), p. 118035. ISSN: 1359-6454. DOI: [10.1016/j.actamat.2022.118035](https://doi.org/10.1016/j.actamat.2022.118035). URL: <https://www.sciencedirect.com/science/article/pii/S1359645422004165>.
- [57] T. Isensee. “Multiscale modeling of dendritic growth kinetics with liquid convection”. PhD thesis. ETSI Caminos Canales y Puertos, Defended January 18, 2023.
- [58] H. Jamgotchian et al. “Localized microstructures induced by fluid flow in directional solidification”. In: *Physical Review Letters* 87.16 (2001), p. 166105. DOI: [10.1103/physrevlett.87.166105](https://doi.org/10.1103/physrevlett.87.166105).

- [59] B. Jelinek, M. Eshraghi, S. Felicelli, and J. F. Peters. “Large-scale parallel lattice Boltzmann–cellular automaton model of two-dimensional dendritic growth”. In: *Computer Physics Communications* 185.3 (2014), pp. 939–947. ISSN: 0010-4655. DOI: [10.1016/j.cpc.2013.09.013](https://doi.org/10.1016/j.cpc.2013.09.013). URL: <https://www.sciencedirect.com/science/article/pii/S0010465513003147>.
- [60] K. Ji, E. Dorari, A. J. Clarke, and A. Karma. “Microstructural pattern formation during far-from-equilibrium alloy solidification”. In: *Physical Review Letters* 130.2 (2023), p. 026203.
- [61] A. Karma. “Dendritic Growth”. In: *Branching in Nature - Dynamics and Morphogenesis of Branching Structures, from Cell to River Networks* 14 (2001), pp. 365–402.
- [62] A. Karma. “Phase field methods”. In: *Encyclopedia of Materials: Science and Technology*. 2nd. Oxford: Elsevier, 2001, pp. 6873–6886.
- [63] A. Karma. “Phase-field formulation for quantitative modeling of alloy solidification”. In: *Physical review letters* 87.11 (2001), p. 5701.
- [64] A. Karma and P. Pelcé. “Oscillatory instability of deep cells in directional solidification”. In: *Physical Review A* 39.8 (1989), p. 4162.
- [65] K. Kubarych and J. Aurrecochea. “Post Field Test Evaluation of an Advanced Industrial Gas Turbine First Stage Turbine Blade”. In: Pennsylvania, Oct. 1993.
- [66] W. Kurz and R. Trivedi. “Banded solidification microstructures”. In: *Metallurgical and Materials Transactions A* 27 (1996), pp. 625–634.
- [67] W. Kurz, D. J. Fisher, and R. Trivedi. “Progress in modelling solidification microstructures in metals and alloys: dendrites and cells from 1700 to 2000”. In: *International Materials Reviews* 64.6 (2019), pp. 311–354. DOI: [10.1080/09506608.2018.1537090](https://doi.org/10.1080/09506608.2018.1537090).
- [68] W. Kurz, M. Rappaz, and R. Trivedi. “Progress in modelling solidification microstructures in metals and alloys. Part II: dendrites from 2001 to 2018”. In: *International Materials Reviews* 66.1 (2021), pp. 30–76. DOI: [10.1080/09506608.2020.1757894](https://doi.org/10.1080/09506608.2020.1757894).
- [69] J. S. Langer. “Instabilities and pattern formation in crystal growth”. In: *Reviews of modern physics* 52.1 (1980), p. 1.
- [70] J. Langer. “Models of pattern formation in first-order phase transitions”. In: *Directions in condensed matter physics: Memorial volume in honor of shang-keng ma*. World Scientific, 1986, pp. 165–186.
- [71] J. Langer. “Lectures in the theory of pattern formation”. In: *Chance and matter* 629 (1987).
- [72] L. Langston. “Single-crystal turbine blades earn ASME milestone status”. In: *Mach. Des* 90 (2018), pp. 46–52. URL: <https://www.machinedesign.com/mechanical-motion-systems/article/21836518/singlecrystal-turbine-blades-earn-asme-milestone-status> (visited on 03/22/2023).

- [73] W. Losert, B. Shi, and H. Cummins. “Evolution of dendritic patterns during alloy solidification: Onset of the initial instability”. In: *Proceedings of the National Academy of Sciences* 95.2 (1998), pp. 431–438.
- [74] R. Mehrabian, M. Keane, and M. Flemings. “Interdendritic fluid flow and macrosegregation; influence of gravity”. In: *Metallurgical Transactions* 1 (1970), pp. 1209–1220. ISSN: 1543-1916. DOI: [10.1007/BF02900233](https://doi.org/10.1007/BF02900233). URL: <https://link.springer.com/article/10.1007/BF02900233>.
- [75] H. Nguyen-Thi, B. Billia, and H. Jamgotchian. “Influence of thermosolutal convection on the solidification front during upwards solidification”. In: *Journal of Fluid Mechanics* 204 (1989), pp. 581–597. DOI: [10.1017/S0022112089001904](https://doi.org/10.1017/S0022112089001904). URL: <https://doi.org/10.1017/S0022112089001904>.
- [76] H. Nguyen-Thi, G. Reinhart, and B. Billia. “On the interest of microgravity experimentation for studying convective effects during the directional solidification of metal alloys”. In: *Comptes Rendus Mécanique* 345.1 (2017). Basic and applied researches in microgravity – A tribute to Bernard Zappoli’s contribution, pp. 66–77. ISSN: 1631-0721. DOI: [10.1016/j.crme.2016.10.007](https://doi.org/10.1016/j.crme.2016.10.007). URL: <https://www.sciencedirect.com/science/article/pii/S1631072116301048>.
- [77] H. Nguyen-Thi et al. “Directional solidification of Al–1.5wt% Ni alloys under diffusion transport in space and fluid-flow localisation on earth”. In: *Journal of Crystal Growth* 281.2 (2005), pp. 654–668. ISSN: 0022-0248. DOI: [10.1016/j.jcrysGro.2005.04.061](https://doi.org/10.1016/j.jcrysGro.2005.04.061). URL: <https://www.sciencedirect.com/science/article/pii/S0022024805005245>.
- [78] J. Ni and C. Beckermann. “A volume-averaged two-phase model for transport phenomena during solidification”. In: *Metallurgical Transactions B* 22.3 (1991), p. 349. ISSN: 1543-1916. DOI: [10.1007/BF02651234](https://doi.org/10.1007/BF02651234). URL: <https://link.springer.com/article/10.1007/BF02651234>.
- [79] J. Nickolls, I. Buck, M. Garland, and K. Skadron. “Scalable Parallel Programming with CUDA”. In: *Queue* 6.2 (2008), pp. 40–53. ISSN: 1542-7730. DOI: [10.1145/1365490.1365500](https://doi.org/10.1145/1365490.1365500). URL: <https://dl.acm.org/doi/10.1145/1365490.1365500>.
- [80] M. Ode, S. G. Kim, and T. Suzuki. “Recent advances in the phase-field model for solidification”. In: *ISIJ international* 41.10 (2001), pp. 1076–1082.
- [81] A. Ohno. “The Solidification of Metals, Chijin Shokan Co”. In: *Ltd., Tokyo* 24 (1976).
- [82] J. H. Perepezko. “Nucleation in undercooled liquids”. In: *Materials Science and Engineering* 65.1 (1984), pp. 125–135.
- [83] J. H. Perepezko. “Metals Handbook”. In: *Handbook of Thermal Analysis and Calorimetry*. 9th ed. Vol. 15. ASM International, 2018, pp. 101–108.
- [84] T. S. Piwonka. “Aggregate molding materials”. In: *ASM Handbook*. 15 (1988), pp. 319–323.
- [85] T. M. Pollock and W. H. Murphy. “The breakdown of single-crystal solidification in high refractory nickel-base alloys”. In: *Metallurgical and Materials Transactions A* 27.4

- (1996), pp. 1081–1094. DOI: [10.1007/BF02649777](https://doi.org/10.1007/BF02649777). URL: <https://link.springer.com/article/10.1007/BF02649777>.
- [86] T. M. Pollock and S. Tin. “Nickel-Based Superalloys for Advanced Turbine Engines: Chemistry, Microstructure and Properties”. In: *Journal of Propulsion and Power* 22.2 (2006), pp. 361–374. DOI: [10.2514/1.18239](https://doi.org/10.2514/1.18239). URL: <https://arc.aiaa.org/doi/10.2514/1.18239>.
- [87] M. Rappaz and C.-A. Gandin. “Probabilistic modelling of microstructure formation in solidification processes”. In: *Acta Metallurgica et Materialia* 41.2 (1993), pp. 345–360. ISSN: 0956-7151. DOI: [10.1016/0956-7151\(93\)90065-Z](https://doi.org/10.1016/0956-7151(93)90065-Z). URL: <https://www.sciencedirect.com/science/article/abs/pii/095671519390065Z>.
- [88] M. Rappaz and P. H. Thévoz. “Solute diffusion model for equiaxed dendritic growth: Analytical solution”. In: *Acta Metallurgica* 35.12 (1987), pp. 2929–2933. ISSN: 0001-6160. DOI: [10.1016/0001-6160\(87\)90292-6](https://doi.org/10.1016/0001-6160(87)90292-6). URL: [http://www.sciencedirect.com/science/article/pii/0001616087902926](https://www.sciencedirect.com/science/article/pii/0001616087902926).
- [89] B. Ravi. *Metal casting: computer-aided design and analysis*. PHI Learning Pvt. Ltd., 2005.
- [90] G. Reinhart et al. “Impact of solute flow during directional solidification of a Ni-based alloy: In-situ and real-time X-radiography”. In: *Acta Materialia* 194 (2020), pp. 68–79. ISSN: 1359-6454. DOI: <https://doi.org/10.1016/j.actamat.2020.04.003>. URL: <https://www.sciencedirect.com/science/article/pii/S1359645420302603>.
- [91] S. Sakane, T. Takaki, M. Ohno, Y. Shibuta, and T. Aoki. “Two-dimensional large-scale phase-field lattice Boltzmann simulation of polycrystalline equiaxed solidification with motion of a massive number of dendrites”. In: *Computational Materials Science* 178 (2020), p. 109639. ISSN: 0927-0256. DOI: [10.1016/j.commatsci.2020.109639](https://doi.org/10.1016/j.commatsci.2020.109639). URL: <https://www.sciencedirect.com/science/article/pii/S0927025620301300>.
- [92] S. Sakane et al. “Multi-GPUs parallel computation of dendrite growth in forced convection using the phase-field-lattice Boltzmann model”. In: *Journal of Crystal Growth* 474 (2017). The 8th International Workshop on Modeling in Crystal Growth, pp. 154–159. ISSN: 0022-0248. DOI: [10.1016/j.jcrysgro.2016.11.103](https://doi.org/10.1016/j.jcrysgro.2016.11.103). URL: [http://www.sciencedirect.com/science/article/pii/S0022024816308132](https://www.sciencedirect.com/science/article/pii/S0022024816308132).
- [93] A. Sample and A. Hellawell. “The mechanisms of formation and prevention of channel segregation during alloy solidification”. In: *Metallurgical Transactions A* 15 (1984), pp. 2163–2173.
- [94] N. Shevchenko, S. Boden, G. Gerbeth, and S. Eckert. “Chimney formation in solidifying Ga-25wt pct In alloys under the influence of thermosolutal melt convection”. In: *Metallurgical and Materials Transactions A* 44 (2013), pp. 3797–3808. ISSN: 8. DOI: [10.1007/s11661-013-1711-1](https://doi.org/10.1007/s11661-013-1711-1). URL: <https://link.springer.com/article/10.1007/s11661-013-1711-1>.
- [95] A. K. Sinha. *Physical metallurgy handbook*. McGraw-Hill, 2003, pp. 110–111.

- [96] Y. Souhar, V. De Felice, C. Beckermann, H. Combeau, and M. Založník. “Three-dimensional mesoscopic modeling of equiaxed dendritic solidification of a binary alloy”. In: *Computational Materials Science* 112 (2016), pp. 304–317. ISSN: 0927-0256. DOI: [10.1016/j.commatsci.2015.10.028](https://doi.org/10.1016/j.commatsci.2015.10.028). URL: <https://www.sciencedirect.com/science/article/abs/pii/S0927025615006850>.
- [97] B. J. Spencer and H. E. Huppert. “Steady-state solutions for an array of strongly-interacting needle crystals in the limit of small undercooling”. In: *Journal of crystal growth* 148.3 (1995), pp. 305–323.
- [98] D. M. Stefanescu. “Numerical Microscale Modeling of Solidification”. In: *Science and Engineering of Casting Solidification*. Springer International Publishing, 2015, pp. 379–434. ISBN: 978-3-319-15693-4. DOI: [10.1007/978-3-319-15693-4_18](https://doi.org/10.1007/978-3-319-15693-4_18). URL: https://doi.org/10.1007/978-3-319-15693-4_18.
- [99] I. Steinbach. “Pattern formation in constrained dendritic growth with solutal buoyancy”. In: *Acta Materialia* 57.9 (2009), pp. 2640–2645. ISSN: 1359-6454. DOI: [10.1016/j.actamat.2009.02.004](https://doi.org/10.1016/j.actamat.2009.02.004). URL: <https://www.sciencedirect.com/science/article/abs/pii/S1359645409000822>.
- [100] L. Sturz and A. Theofilatos. “Two-dimensional multi-scale dendrite needle network modeling and x-ray radiography of equiaxed alloy solidification in grain-refined Al-3.5 wt-%Ni”. In: *Acta Materialia* 117 (2016), pp. 356–370. ISSN: 1359-6454. DOI: [10.1016/j.actamat.2016.06.005](https://doi.org/10.1016/j.actamat.2016.06.005). URL: [http://www.sciencedirect.com/science/article/abs/pii/S1359645416304244](https://www.sciencedirect.com/science/article/abs/pii/S1359645416304244).
- [101] Tarjeta gráfica NVIDIA GeForce RTX 3090 y 3090 Ti. <https://www.nvidia.com/es-es/geforce/graphics-cards/30-series/rtx-3090-3090ti/>. Accessed: 2023-9-4.
- [102] “Teraflop”. In: July 2023. URL: <https://dictionary.cambridge.org/dictionary/english/teraflop>.
- [103] M. Thomas et al. “Allison manufacturing, property and turbine engine performance of CMSX-4 single crystal airfoils”. In: *Materials for Advanced Power Engineering* 1994 (1994), pp. 1075–1098.
- [104] D. Tourret, M. Francois, and A. Clarke. “Multiscale dendritic needle network model of alloy solidification with fluid flow”. In: *Computational Materials Science* 162 (2019), pp. 206–227. DOI: [10.1016/j.commatsci.2019.02.031](https://doi.org/10.1016/j.commatsci.2019.02.031). URL: <https://www.sciencedirect.com/science/article/abs/pii/S0927025619301065>.
- [105] D. Tourret and A. Karma. “Multiscale dendritic needle network model of alloy solidification”. In: *Acta Materialia* 61.17 (2013), pp. 6474–6491. ISSN: 1359-6454. DOI: [10.1016/j.actamat.2013.07.026](https://doi.org/10.1016/j.actamat.2013.07.026). URL: <https://www.sciencedirect.com/science/article/abs/pii/S1359645413005284>.
- [106] D. Tourret and A. Karma. “Corrigendum to: “Multi-scale dendritic needle network model of alloy solidification” [Acta Mater. 61 (2013) 6474–6491]”. In: *Acta Materialia* 87 (2015), p. 411. ISSN: 1359-6454. DOI: [10.1016/j.actamat.2015.01.026](https://doi.org/10.1016/j.actamat.2015.01.026). URL: <https://www.sciencedirect.com/science/article/abs/pii/S1359645415000397>.

- [107] D. Tourret and A. Karma. “Three-dimensional dendritic needle network model for alloy solidification”. In: *Acta Materialia* 120 (2016), pp. 240–254. ISSN: 1359-6454. DOI: <https://doi.org/10.1016/j.actamat.2016.08.041>. URL: <https://www.sciencedirect.com/science/article/pii/S135964541630619X>.
- [108] D. Tourret, A. Karma, A. J. Clarke, P. J. Gibbs, and S. D. Imhoff. “Three-dimensional Dendritic Needle Network model with application to Al-Cu directional solidification experiments”. In: *IOP Conference Series: Materials Science and Engineering* 84 (2015), p. 012082. DOI: <10.1088/1757-899x/84/1/012082>. URL: <https://doi.org/10.1088/1757-899x/84/1/012082>.
- [109] D. Tourret, Y. Song, A. Clarke, and A. Karma. “Grain growth competition during thin-sample directional solidification of dendritic microstructures: A phase-field study”. In: *Acta Materialia* 122 (2017), pp. 220–235. ISSN: 1359-6454. DOI: <10.1016/j.actamat.2016.09.055>. URL: <https://www.sciencedirect.com/science/article/pii/S1359645416307546>.
- [110] D. Tourret et al. “Three-dimensional multiscale modeling of dendritic spacing selection during Al-Si directional solidification”. In: *JOM* 67.8 (2015), pp. 1776–1785. DOI: <10.1007/s11837-015-1444-2>. URL: <https://doi.org/10.1007/s11837-015-1444-2>.
- [111] R. Trivedi and W. Kurz. “Dendritic growth”. In: *International Materials Reviews* 39.2 (1994), pp. 49–74. DOI: <10.1179/imr.1994.39.2.49>. URL: <https://doi.org/10.1179/imr.1994.39.2.49>.
- [112] R. Trivedi, P. Mazumder, and S. N. Tewari. “The effect of convection on disorder in primary cellular and dendritic arrays”. In: *Metallurgical and Materials Transactions A* 33.12 (2002), pp. 3763–3775. DOI: <10.1007/s11661-002-0249-4>. URL: <https://link.springer.com/article/10.1007/s11661-002-0249-4>.
- [113] F. VerSnyder and A. Giamei. “Directional Solidification and Single-Crystal Casting Technology”. In: *Pergamon Press, Encyclopedia of Materials Science and Engineering*. 2 (1986), pp. 1202–1204.
- [114] C. Y. Wang and C. Beckermann. “A multiphase solute diffusion model for dendritic alloy solidification”. In: *Metallurgical and Materials Transactions A* 24.12 (1993), pp. 2787–2802. ISSN: 1543-1940. DOI: <10.1007/BF02659502>. URL: <https://link.springer.com/article/10.1007/BF02659502>.
- [115] C. Y. Wang and C. Beckermann. “Equiaxed dendritic solidification with convection: Part I. Multiscale/multiphase modeling”. In: *Metallurgical and Materials Transactions A* 27.9 (1996), pp. 2754–2764. ISSN: 1543-1940. DOI: <10.1007/BF02652369>. URL: <https://link.springer.com/article/10.1007/BF02652369>.
- [116] W. Wang, P. Lee, and M. McLean. “A model of solidification microstructures in nickel-based superalloys: predicting primary dendrite spacing selection”. In: *Acta Materialia* 51.10 (2003), pp. 2971–2987. ISSN: 1359-6454. DOI: [10.1016/S1359-6454\(03\)00110-1](10.1016/S1359-6454(03)00110-1). URL: <https://www.sciencedirect.com/science/article/pii/S1359645403001101>.
- [117] D. M. Young. “Iterative methods for solving partial difference equations of elliptic type”. In: *Transactions of the American Mathematical Society* 76 (1954), pp. 92–111. DOI: <10>.

2307/1990745. URL: <https://www.ams.org/journals/tran/1954-076-01/S0002-9947-1954-0059635-7/>.

ANNEXES

C Work Breakdown Structure

The current thesis is an outcome of research in computational materials science. To structure the process, the research project has been segmented into the following sections:

- Initial Training
- Simulations
- Data Pre-processing
- Data Analysis
- Documentation

Each of these sections has been further subdivided into lower levels, resulting in a structure consisting of 4 ranks. Starting from level 1, representing the entire project, and descending to levels 3 and 4, which make up the designated “Work Packages” (also known as activities). The successful completion of all these Work Packages signifies the overall completion of the project. The project’s breakdown structure can be visualized on the following page.

D Time Planning

A Gantt diagram, created in Latex, was used to plan the project (see next pages). The scheduling was divided into two main time-based phases:

- The first phase, spanning three and a half months during the RIF grant awarded by IMDEA Materials, focused on the technical aspects, including laboratory work, data collection, simulations, and initial Python implementation of processing algorithms.
- The second phase, which took place during the last academic year, was dedicated to research documentation and report writing. It included publishing a paper with the primary research results and completing the final report.

Task distribution for both phases was based on the previously mentioned Gantt chart.

E Budgeting

The budget has been divided into three types of resources:

- **Energy resources:** Estimating the electricity cost for the conducted simulations proves challenging in terms of precision. In this context, we calculate an average cost to represent the medium expenses associated with the most significant simulations. See table E.1.

Energy Resources - GPU Simulations

Name	Number of Simulations	Duration (h) ⁽¹⁾	Consumption (kW) ⁽²⁾	€/kWh ⁽³⁾	Cost
Map A	44	46.00	0.35	0.3071	217.55 €
Map B	45	46.00	0.35	0.3071	222.49 €
Map C	45	46.00	0.35	0.3071	222.49 €
Map D	47	46.00	0.35	0.3071	232.38 €
Total energy resources:					894.91 €

Table E.1: Estimated Electricity Costs for Simulations: ⁽¹⁾ Based on the average duration, with a maximum duration not exceeding 92 hours; ⁽²⁾ Calculated using the average consumption for the NVIDIA RTX 3090 [101]; ⁽³⁾ Computed using the average electricity price (including VAT) for the month of June 2022 [33], when the simulations were performed.

- **Human resources:** In this section, we have accounted for the hours invested by the student Josep María Barberá, valued at a rate of 10 €/hour, as well as the hours contributed by the three supervisors, priced at 50 €/hour each. See table E.2. The total hours attributed to Josep María have been calculated as follows: During the Summer 2022 IMDEA Internship, which spanned three and a half months from July 2022 to mid-October 2022, with work conducted five days a week for seven hours each day. This amounts to a total of 14 weeks, resulting in 490 hours. In the Summer of 2023, he worked for two months, from June to September 2023, with seven days of work per week for two hours each day. This adds up to 12 weeks, accounting for 168 hours. Additionally, the first week and a half of September involved intensive work, spanning ten days at eight hours per day, totaling 80 hours. In total, this amounts to 738 hours.

Human Resources

Name	Hours	€/hour	Cost
Josep María	738	10.00 €	7,380.00 €
Supervisors	240	50.00 €	12,000.00 €
Total human resources:			19,380.00 €

Table E.2: Allocation of Human Resources.

- **Computer resources:** This resource outlines the various software programs employed in project execution. The total cost is zero, as these programs have been utilized under different licensing arrangements, including academic licenses, OpenSource licenses, trial versions, or licenses provided by the Universidad Politécnica de Madrid (the Polytechnic University of Madrid). See table E.3.

The total budget for this project has been 20274.91 €.

Software		
Program	License	Price
Writing and Editing		
TexStudio	OpenSource	0 €
Ipe Drawing Editor	OpenSource	0 €
Microsoft Excel (from Microsoft 365)	UPM	
Microsoft Word (from Microsoft 365)	UPM	
Simulation and Programming		
GitHub	OpenSource	0 €
Visual Studio Code	OpenSource	0 €
Jupyter Notebooks	OpenSource	0 €
Slurm	OpenSource	0 €
ParaView	OpenSource	0 €
Communication and productivity		
Slack	IMDEA	0 €
Total computer resources:		0 €

Table E.3: *Overview of Computer Resources Utilized*

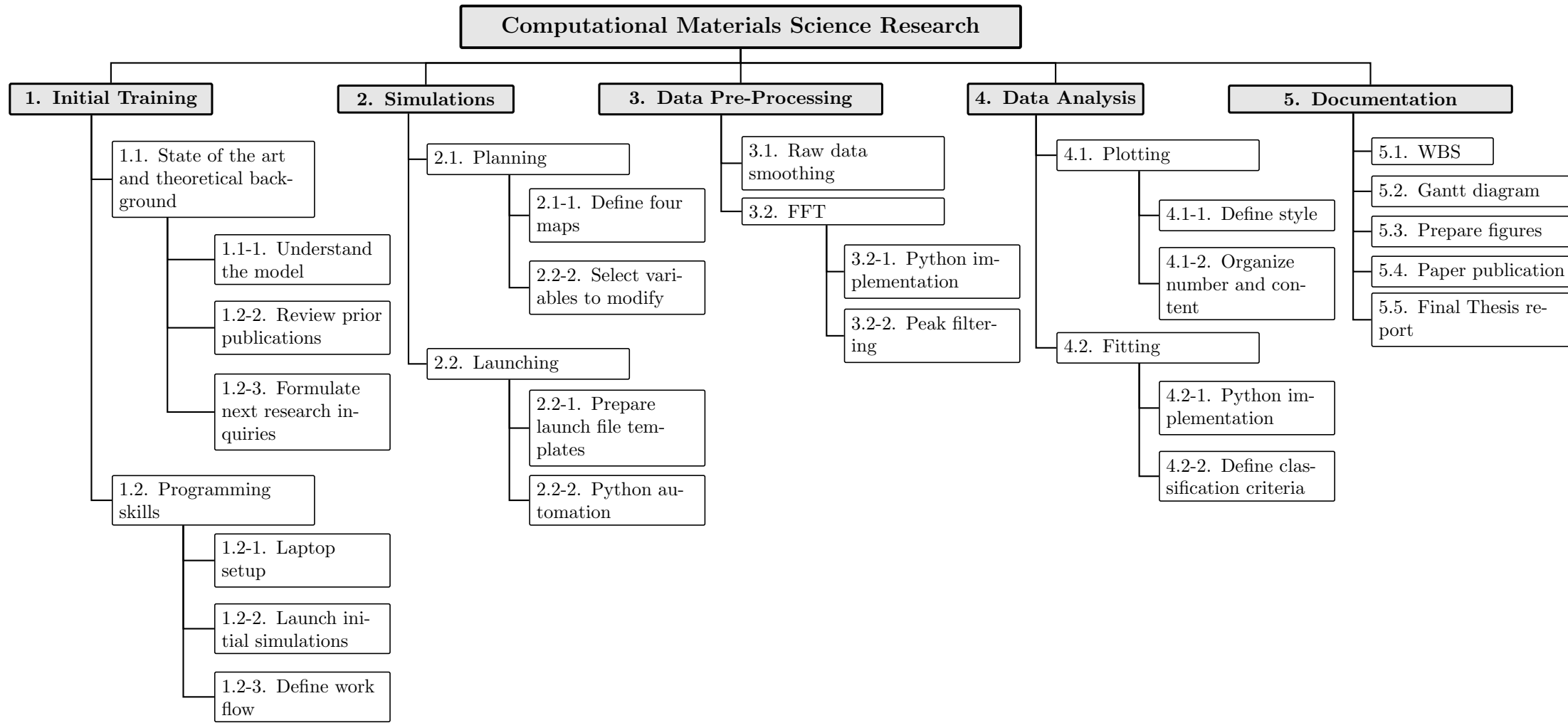


Figure E.1: Work Breakdown Structure (WBS). Hierarchical project breakdown, for the visualization of project components and deliverables, facilitating their orderly execution.

Simulations and Data Pre-Processing

Initial Training

- Understand the model
- Review prior publications
- Formulate next research inquiries
- Laptop setup
- Initial simulation and Workflow

Launch of Simulations

- Define four maps
- Variables to modify
- Prepare launch file

Python automation script

Data Pre-Processing

- Raw data smoothing
- FFT
- Frequency peak filtering
- Python script implementation

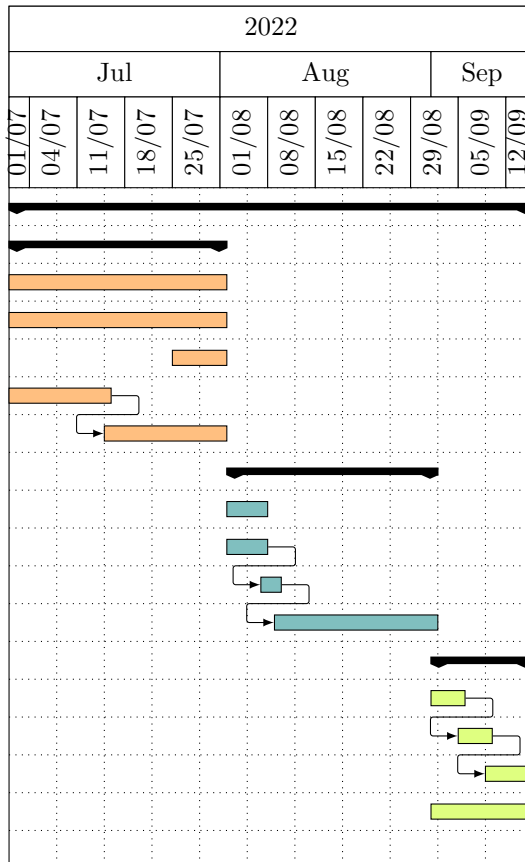


Figure E.2: Gantt Diagram (part 1): first part of the research corresponding to the duration of the RIF (Research Initiation Fellowship) at IMDEA Materials.

Data Analysis

- Plot script implement.
- Plots planning
- Fitting implementation
- Behavior classification

Documentation

- Figures preparation
- Paper publication
- Final thesis report
- Thesis review
- Final submission

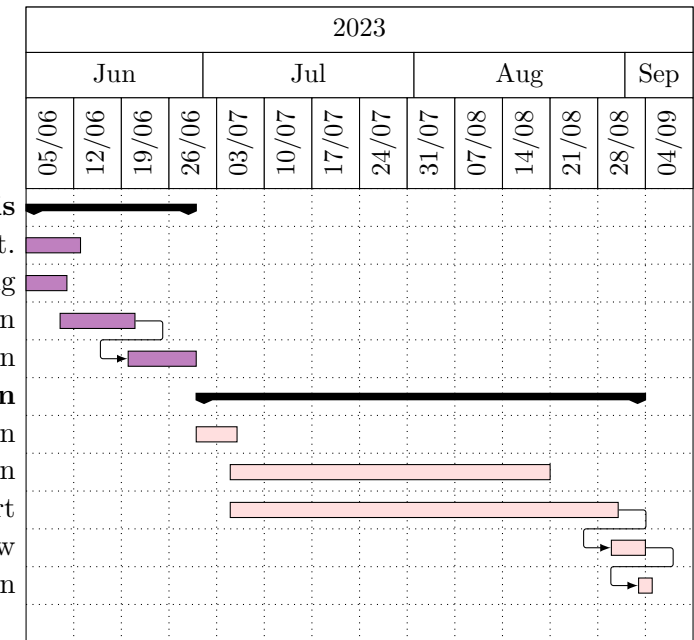


Figure E.3: Gantt Diagram (part 2): last part of the research corresponding to the analysis and the documentation for the Bachelor's Thesis.